1992

Three-dimensional flaw reconstruction using a real-time X-ray imaging system

Edward Raymond Doering
Iowa State University

INFORMATION TO USERS

This manuscript has been reproduced from the microfilm master. UMI films the text directly from the original or copy submitted. Thus, some thesis and dissertation copies are in typewriter face, while others may be from any type of computer printer.

The quality of this reproduction is dependent upon the quality of the copy submitted. Broken or indistinct print, colored or poor quality illustrations and photographs, print bleedthrough, substandard margins, and improper alignment can adversely affect reproduction.

In the unlikely event that the author did not send UMI a complete manuscript and there are missing pages, these will be noted. Also, if unauthorized copyright material had to be removed, a note will indicate the deletion.

Oversize materials (e.g., maps, drawings, charts) are reproduced by sectioning the original, beginning at the upper left-hand corner and continuing from left to right in equal sections with small overlaps. Each original is also photographed in one exposure and is included in reduced form at the back of the book.

Photographs included in the original manuscript have been reproduced xerographically in this copy. Higher quality 6" x 9" black and white photographic prints are available for any photographs or illustrations appearing in this copy for an additional charge. Contact UMI directly to order.

U·M·I

University Microfilms International
A Bell & Howell Information Company
300 North Zeeb Road, Ann Arbor, MI 48106-1346 USA
313/761-4700 800/521-0600

Order Number 9234804

Three-dimensional flaw reconstruction using a real-time X-ray imaging system

Doering, Edward Raymond, Ph.D.

Iowa State University, 1992

U·M·I
300 N. Zeeb Rd.
Ann Arbor, MI 48106

Three-dimensional flaw reconstruction using a real-time X-ray imaging system

by

Edward Raymond Doering

A Dissertation Submitted to the

Graduate Faculty in Partial Fulfillment of the

Requirements for the Degree of

DOCTOR OF PHILOSOPHY

Department: Electrical Engineering and Computer Engineering
Major: Electrical Engineering (Communications and Signal Processing)

Approved:

Signature was redacted for privacy.

In Charge of Major Work

Signature was redacted for privacy.

For the Major Department

Signature was redacted for privacy.

For the Graduate College

Iowa State University
Ames, Iowa
1992

TABLE OF CONTENTS

LIST OF TABLES

LIST OF FIGURES

ACKNOWLEDGMENTS

This work was sponsored by the NSF Industry/University Center for NDE at Iowa State University.

CHAPTER 1. INTRODUCTION

Nondestructive evaluation (NDE) is a broad interdisciplinary field of study devoted to detecting and characterizing flaws or defects within structures and devices. These devices need to be analyzed during manufacture and while in service. Destructive testing is only useful in a manufacturing environment, and then only when the part cost is low and part volume is high. Here it is feasible to draw random samples from a lot, make destructive tests, and statistically infer the performance of the remaining parts in the lot. Pull-testing the wire bonds of integrated circuits demonstrates a useful destructive test. However, high performance (expensive) parts cannot be discarded for testing purposes. Furthermore, the critical nature of these parts while in service mandates that they be evaluated periodically for integrity. Thus, NDE techniques provide a valuable service to manufacturers and service personnel alike.

Determining the three-dimensional position, orientation, and size of a defect is an important type of NDE measurement. Fracture mechanics uses this 3-D information to predict how a defect will grow or change as a result of renewed stress on the material. In a manufacturing environment, knowledge of the 3-D location permits accurate decisions to be made about whether the part can be fixed or whether it should be discarded. In a repair situation, the 3-D flaw location can be programmed

into computer-controlled machining equipment to properly remove a minimal amount of material to gain access to the flaw area. In addition, this 3-D flaw information can be used as data for process control.

Three-dimensional measurements are also used for quality control to determine if a device has been manufactured correctly. For example, turbine blades from jet engines operate in a high temperature environment. Coolant tubes are embedded within the blade and follow the complex geometry of the turbine blade shape. The blades must be inspected to determine if the tube diameters meet specification, and the positions of the tubes relative to the sidewalls of the blade must be within tolerance as well. Two-dimensional projection measurements using X-ray inspection can determine the tube diameters. Three-dimensional measurements are required to ensure that the coolant tubes are properly located within the blade material.

NDE is performed on a wide variety of materials including metals, ceramics, epoxies, wood, fiberglass, and composites. Many types of NDE inspections have been developed; they are differentiated primarily on how they introduce energy into the material and measure the result. The types of energy involved include acoustic (ultrasonic and acoustic emission), electromagnetic radiation (microwaves, eddy currents, optics, X-rays, and gamma rays), neutrons, and thermal waves.

A general model for the NDE problem is indicated in Figure 1.1. The device-under-test, or sample, is a physical object possibly containing one or more defects. Energy is introduced to the sample by the source. This energy interacts with the structure of the material and is observed by the detector. The goal of the nondestructive measurement is to analyze the detected energy to derive quantitative information about the structure of any flaws or defects present in the sample. *A priori* knowledge

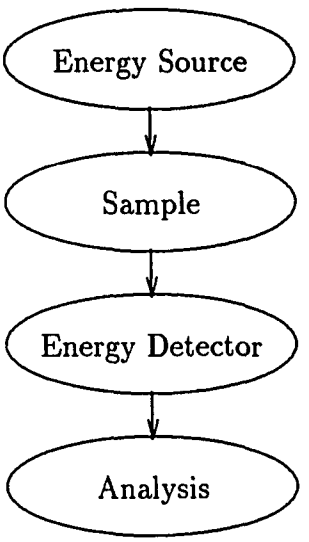

Figure 1.1: General model for NDE inspection

about the energy source, material structure, and detector response is the key to this analysis.

Radiography is the technique of illuminating an object with X-ray radiation and recording the latent image formed by variations within the object. Traditionally these variations have been recorded on X-ray sensitive film. Real-time radiography (RTR) replaces the film with and X-ray-to-light conversion device. A typical RTR system consists of an X-ray source, an object positioner, a combination X-ray-to-light converter and intensifier (herein referred to as the image intensifier), video camera, frame digitizer, computer, and display device. For industrial applications using NDE, RTR has the advantages of high throughput, reduced costs associated with film processing, and interactive inspection. RTR provides the additional capabilities of image enhancement, automatic inspection, and digital archival when coupled with a dig-

itizer and digital computer. The primary disadvantages of RTR are significantly reduced spatial resolution and reduced contrast sensitivity compared to film. Both film-based radiography and RTR are used to record and display 2-D projections of the sample under test.

This document describes the development of a system using a real-time radiography laboratory to make 3-D measurements of crack endpoints and other features of interest within a material. Points of interest include endpoints of simple cracks, vertices of a polyline describing a crack with complicated geometry, and centroids of void-like or inclusion-like flaws. Non-flaw features such as the axis of an embedded hole relative to the external surface of a sample can be determined as well. The laboratory environment of the real-time X-ray system affords a high degree of positional accuracy of all elements of the system including X-ray source, sample, and detector. Consequently, the 3-D coordinates of a feature are determined reliably and accurately. The image intensifier plays the key role in determining the overall RTR image quality, so image processing routines were developed to correct the key spatial degradations of the detector (reduced resolution and geometric distortion). The system performance was determined by making measurements on fabricated samples and industrial samples.

It should be noted that laboratory and real-time detector calibrations developed for this work are applicable to any type of quantitative measurement made with the RTR system, including 2-D projection radiography and computed tomography. Moreover, the integration of the computer, frame digitizer, and and high-speed processor into all aspects of data collection, processing, and analysis provides a framework that easily incorporates these other techniques.

Background on X-Ray NDE

X-ray NDE uses an X-ray field as the energy source. The X-ray source generates a cone-shaped beam of X-ray photons. This beam passes through the sample and is selectively attenuated by local material variations in thickness, density, and atomic number. The field exiting the sample carries a projection or latent image of the sample interior which is sensed by an area detector. The detector converts the X-ray field to an optical field which is viewed by the human eye, or more usefully, digitized, processed and displayed on an image monitor. Quantitative information about the image (and hence the material's structure) is determined using numerical processing of the digitized image.

X-ray sensitive film is the traditional area detector. Continuous X-ray-to-light conversion devices using a phosphor screen have been available as well; poor sensitivity is the primary drawback of these screens. Image intensification was developed to boost the sensitivity of the screen, and the image quality of a modern image intensifier now rivals X-ray film for some applications (Halmshaw, 1990).

NDE practitioners using X-ray apparatus either use film or the real-time detector. Film has the advantages of high resolution, high dynamic range (100:1), long integration time which reduces quantum mottle noise, and archival capability. Resolution is measured in terms of spatial frequency, with units of line pairs (lp) per unit distance (e.g., lp/mm). Film attains resolution of 10 to 20 lp/mm (Halmshaw, 1987). The disadvantage of film is the need for chemical processing to develop and fix the image. This process takes at least three minutes, and results in a static image. The real-time detector allows the X-ray field to be viewed continuously, so the sample can be inspected rapidly under a wide variety or orientations. This advan-

tage is offset by the real-time detector's lower resolution of 3–6 lp/mm (Halmshaw, 1987) and lower dynamic range of 20:1 (Gupta and Krohn, 1987). Furthermore, the real-time converter does not have any inherent integration capability, although this can be overcome using digital integration (i.e., frame averaging). For these reasons, most NDE practitioners prefer film.

Usually the 2-D X-ray projection is analyzed to determine the presence and severity of a flaw. This single projection does not communicate any information about the position of the flaw in the material along the line of sight from the X-ray source to the detector. Furthermore, a single projection will usually miss an arbitrarily-oriented thin crack. The real-time technique allows the sample to be rapidly viewed in a wide range of orientations.

Several techniques have been developed to identify the depth of a defect in the material, or its 3-D coordinates with the sample. Film-based stereography works by obtaining a stereo pair of images. Either the source or sample is translated relative to the film detector. Triangulation methods are used to identify the flaw depth. This method requires high accuracy in determining the 3-D coordinates of the source, sample, and detector. Swapping film trays between the two exposures requires a reference object to be included in order to determine the proper orientation of the film with respect to the global coordinate system. The main advantage is the long integration time of film.

Computed tomography (CT) (Herman, 1979; Martz *et al.*, 1990) is the most widely used technique for 3-D flaw position determination. A CT scan uses a fan beam source to illuminate a thin cross section of the sample. This 1-D projection is recorded using either a stepped point detector or a 1-D array detector. The sample is rotated a

slight amount and a new projection is acquired. This process repeats until the object has been rotated 180°. These 1-D projections are input to an image reconstruction routine which generates a 2-D image of the cross-sectional slice of the object. The resolution of the image is governed by the number of points recorded for each 1-D projection and the angular difference between each orientation. CT systems achieve resolutions in the range 0.01–0.1 cm/pixel (Martz *et al.*, 1990); microtomography systems make use of projective magnification with an X-ray source spot size of 10μm and achieve resolution of 10–50 μm/pixel (Feldkamp, Jesion, and Kubinski, 1989). The intensity of the CT image pixel is proportional to X-ray attenuation, so variations in material density are visualized in the image. Multiple slices are used to create a 3-D volume image. Tomosynthesis uses a cone-beam source and an area detector to yield the 3-D volume image more quickly.

The main disadvantage of CT is the high equipment expense and large computation requirements for image reconstruction. Commercial CT systems use multiple X-ray sources and line detectors to collect the 1-D projection data in parallel. Consequently, they are complex and very expensive. The total time for data acquisition and image reconstruction is on the order of 5 minutes. At the opposite extreme, a cheap system using a single X-ray source, one point detector, and a rotation device requires many hours to collect projection data of sufficient signal-to-noise ratio to achieve a usable reconstruction. CT also requires 360 degree access to the part. Some samples are plate-like and essentially yield no information along the long axis, and other sample geometries permit rotation over only a limited angle of rotation. Modified CT routines have been developed to use *a priori* information in the form of a CAD model of the sample (Eberhard and Hedengren, 1988) and minimal support

constraints (Roberts, 1991); however, the results must be carefully understood to ensure they are free of artifacts.

To date, most applications of CT have only made qualitative use of the gray scale image (Cortes, Lin, and Miller, 1991). Reconstruction noise due to the CT data acquisition hardware and reconstruction software algorithms has been the main impediment to quantitative information. For example, a CT image of a dense particle embedded in matrix of lower density will have streak artifacts and blurring of the imaged particle's edges. Advanced reconstruction algorithms are being developed to overcome these problems (Cortes, Lin, and Miller, 1991).

Coplanar rotational laminagraphy is an interesting method which uses film to create a cross-sectional image like CT. The sample is placed between the source and the detector as in conventional radiography, but the film is placed in parallel with the X-ray field. The sample and film are attached to rotating stages which rotate in phase. The source and film define a plane; an image of the intersection of this plane with the sample is created on the film. The film is rotated several hundred times during the exposure. The resulting image is highly blurred and requires a significant amount of image restoration processing to yield a usable image (Segal and Cohen, 1990).

Real-Time Radiography in NDE

Real-time radiography (RTR) systems are able to continuously transform the X-ray field into an optical image. In contrast, film-based radiography requires at least 3 minutes for developing from image acquisition to image display (Halmshaw, 1987). Real-time systems replace the film with a scintillation screen to continuously convert

the X-ray field to an optical field. The crystals in this screen are phosphorescent, and the incident X-ray photon excites the crystal structure which subsequently emits a burst of lower energy optical photons. This optical image could in principle be viewed by the human eye when properly dark adapted. However, this optical image is weak and is required to be digitized. This weak optical image is intensified to make it compatible with a video camera. Photons are electrically neutral and cannot be amplified directly. Image intensifiers operate by converting the weak optical field to an electron field using a photocathode utilizing the photoelectric effect. The electrons are accelerated and focused onto a smaller phosphor screen which emits optical photons. The intensified image has gain due to electron acceleration and image minification.

Real-time X-ray inspection is used to provide immediate information concerning the presence and severity of flaws in a sample, and to rapidly determine dimensions, mechanical configuration, and the presence and positioning of components in a mechanism (ASTM E 1000-88, 1988). Use of the real-time image also permits all of the parameters involved to create the final image to be manipulated interactively to optimize the image, as opposed to exposing and developing a series of radiographs (ASTM E 1255-88, 1988). These parameters include X-ray source voltage and current, display contrast, and digital image processing function.

The advantages of RTR over a film-based system are high inspection throughput (seconds instead of minutes), reduced costs incurred by film processing, and interactive inspection. Image digitization and computer processing add the additional advantages of image enhancement, automated inspection, and digital image archival. The disadvantages of RTR are significantly reduced spatial resolution, reduced con-

trast sensitivity, and higher cost. RTR systems using the electron acceleration-based image intensifier have geometrical distortion due to the design of the conversion tube. RTR conversion devices also lack the integration capability of film (which results in higher noise and quantum mottle), but this is alleviated by frame averaging on the digitizer.

The term "real-time" takes on different meanings according to the operation. For example, cine-radiography systems are used to image high speed events such as a bullet impacting an object. This requires frame rates of 10,000 to 100,000 frames per second (fps). Computer animation requires between 1 and 30 fps; 8 fps is considered the lower limit for interactivity. Near-real-time systems operate in the range 0.1 to 1 fps. For this work, "real-time" is defined as 8 fps or greater and near-real-time is defined as 0.1 to 8 fps. Figure 1.2 shows the different regimes encountered in real-time work.

Real-time processing techniques that are most generally used include: (1) field-flattening, (2) frame averaging, (3) image "crispening" (sharpening), and (4) contrast enhancement; frame averaging and contrast enhancement are sufficient for some applications (Halmshaw, 1987).

Real-time systems are presently used for a variety of inspection applications. Electronic circuit board assemblies need to be inspected for continuity of the circuit traces as well as for integrity of the bond wires enclosed in the integrated circuit package. The dual advantages of continuous imaging and wide magnification range offered by a microfocus-based real-time system permit all aspects of an assembly to be inspected at once (Buechler, 1987). Microfocus X-ray sources have an emission spot size of 0.01–0.1 mm; sources with a 10μm spot size permit geometric magnification of

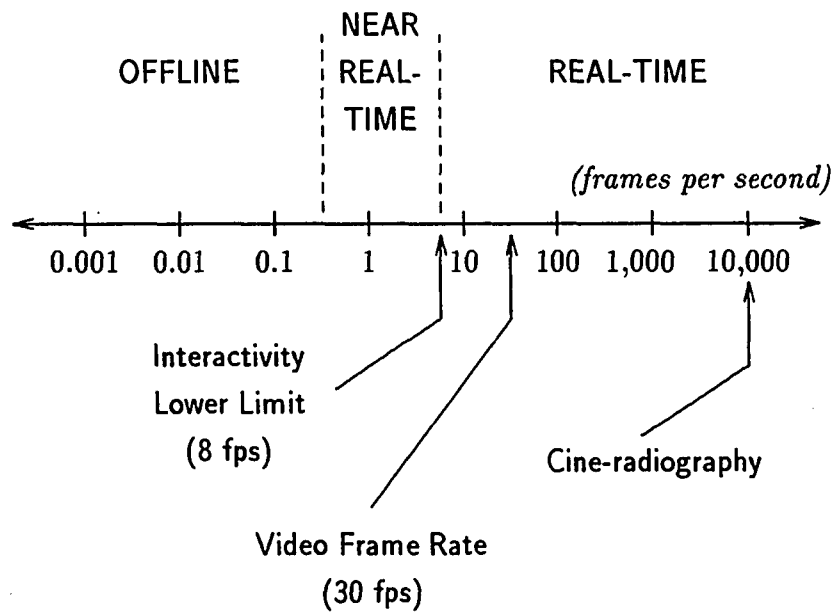

Figure 1.2: Spectrum of real-time applications

greater than 100 times (ASTM E 1255-88, 1988). Low X-ray energies (~20KeV) were found to be optimum for examining these components since the materials involved (polyethylene, aluminum, and silicon) all have low atomic number; lower X-ray energy yields a higher contrast image since the difference in energy-dependent mass attenuation coefficients for each material is more pronounced in this regime (Stupin, 1987).

Until recently, barriers to the widespread use of RTR inspection systems in the electronics industry included lower resolution of the image compared to film, difficulty of use, and high initial cost (Olsen, 1988). However, the steady improvement in microfocus source design mitigates the resolution problem of the real-time detector via projective magnification, and the continuing decrease in image processing hardware/software cost has further increased the utility of the real-time image in terms of information quantitation and automated analysis. These techniques include calculation of adhesion void areas, registration shifts, and linear/radial distances (Olsen, 1988). Furthermore, the film costs for larger operations range from $5,000–$10,000 per month (Olsen, 1988), so these savings would pay for the real-time system (costing $100,000) in one to two years.

Real-time inspection has been successfully applied to the inspection of welds. Weld inspection requires imaging of a large range of materials from less than 1 mm to more than 40 mm of steel (Munro *et al.*, 1987), with applications ranging from laser and electron beam weldments of dissimilar materials to steel pipes with longitudinal and/or circumferential joints. Pipe mills produce product at high speeds which requires automated or semi-automated inspections. Presently, the film-less

inspection capability represents a cost savings, but automated inspection holds the promise of still greater savings due to increased accuracy (Munro *et al.*, 1987).

Weld inspection techniques include the use of area detector and linear semiconductor arrays (Link *et al.*, 1989; Jacquemond, Odet, and Goutte, 1990). Linear arrays can continuously image a continuous welding process without waiting for a 2-D image to be acquired as in a conventional area detector/frame grabber combination. Linear array detectors also offer increased dynamic range, higher signal-to-noise ratio, and excellent spatial resolution compared to film and fluoroscopic screen techniques (Gupta and Krohn, 1987).

An automated real-time turbine blade inspection system has been developed (Betz and Barray, 1988). This system uses a robotic arm as a part handler, and image analysis algorithms were developed to automate the inspection process. The nickel-alloy material of the blade had thickness variations ranging from 0.5 mm to 13 mm. A combination of analog shading correction in the video camera electronics and digital contrast enhancement was used to view this wide variation in thickness in a single view. Image subtraction of two integrated images (128 averaged video frames) with a slight offset in the X and Y position of the part between views was used to enhance visibility of low contrast image details.

Research Objective

The purpose of this research is to develop a system utilizing a real-time radiography laboratory to locate and size crack-like defects and other points of interest within a material using a limited number of views. This system will augment an existing real-time inspection setup by adding the ability to make quantitative 3-D

measurements. While this system will not provide the extreme detail of a CT reconstruction, it will, however, provide sufficient information for NDE practitioners who need to know where a flaw is located and its approximate size. This information is easily obtained without the time and expense required of a full CT reconstruction.

Approach

The real-time system consists of many components, with the X-ray detector playing the key role in determining overall image quality. The image intensifier is characterized for geometric and radiometric distortions as well as blurring. The 3-D system requires high spatial resolution and linearity, so these aspects are emphasized. Image restoration is used to improve the resolution of the detector, and a non-linear image warp is used to correct geometric distortion.

Calibration of the laboratory setup is essential to minimize errors. Detector calibration techniques were developed to determine the system point spread function (PSF) for image restoration, and to measure the geometric distortion. Image-based methods were also developed to determine the 3-D coordinates of the X-ray source and sample relative to the detector. Calibration steps requiring a great deal of data collection were automated.

The lab setup for this research uses a fixed source and fixed detector arrangement. A high resolution sample positioner is used to translate and rotate the sample. Traditional stereography techniques use a shifted source. The stereography equations were modified to use a fixed source and to take advantage of the more general sample motions made available by the positioner.

Real-time processing is necessary to restore and enhance the image. Certain

orientations of the sample place the feature of interest in a non-optimal contrast range for the operator. Contrast enhancement routines can overcome this problem. A high speed DSP (digital signal processing) board is used for the image-oriented calculations. Software was developed to make the real-time processing conveniently accessible to the operator whenever image enhancement is needed. The particular DSP board used for this research was selected since it can run any processing routine that can be implemented using the C language.

3-D reconstruction equations were developed for a cone-beam source, an arbitrary sequence of sample movement, and arbitrary detector geometry. Error estimates were determined by estimating all measurement errors pertaining to the positions of the lab equipment and detector. Monte Carlo simulations of the reconstruction process were used to determine how each type of error contributed to the overall measurement error. A technique was also developed to analyze the particular reconstruction experiment and characterize the numerical stability of the inversion. As much as possible, calibration and modelling are used to minimize the errors.

Overview of Chapters

Chapter 2 describes the laboratory equipment used. It discusses the separate components as well as how they work together to make a complete 3-D measurement system. Chapter 3 describes the mathematical techniques used for 3-D reconstruction and error estimation. A practical implementation of these techniques in the RTR laboratory is discussed, and simulation results are presented to provide an understanding of the major contributors to overall accuracy of the system. Chapter 4 investigates the X-ray detector in more detail. The non-ideal behavior of the detector is charac-

terized and modeled to determine methods for overcoming its degradations. These include techniques for image restoration and image warping. Chapter 5 describes calibration techniques for determining the laboratory geometry. The performance of the complete system is analyzed by making measurements on a variety of samples ranging from simple to complex. Chapter 6 summarizes the work, presents conclusions, and describes future directions for this research.

CHAPTER 2. LABORATORY EQUIPMENT

This chapter describes the real-time X-ray laboratory equipment used for this research. An overview of the laboratory is presented first, followed by a detailed description of the separate components in the laboratory. The chapter concludes with a discussion of how the components interconnect in terms of data flow and system control.

System Overview

Figure 2.1 shows a diagram of the physical components of the real-time X-ray laboratory. All the parts associated with generating and sensing the X-ray field are enclosed within a lead-lined containment vault to protect people from radiation. The X-ray source generates an X-ray field which passes through the sample mounted to a remotely controlled sample positioner. This positioner permits the operator to translate and rotate the sample while viewing the X-ray projection image. This greatly assists interaction with the sample compared to working with X-ray film. The latent image imparted to the X-ray field by the sample is converted to an optical image by the image intensifier. The video camera converts this optical image to a video signal which is digitized and stored as a raster-scanned image in the frame digitizer/frame store. Finally this image is displayed on the image monitor. Optionally, the image

is processed to improve contrast, resolution, or to correct any aberrations previously introduced into the imaging chain.

Equipment

X-ray source

A microfocus X-ray generator is used in this RTR laboratory. The generator works by passing an electron current through a filament. This heats the filament which releases a stream of electrons which are accelerated and focused onto a tungsten target. The filament and target are contained within an evacuated tube to minimize electron collisions with gas molecules. Upon impact, the electrons experience extreme deceleration. An accelerating (or decelerating) free electron always emits electromagnetic radiation; here, the radiation is in the X-ray regime. The parameters of the system are accelerating voltage for the electrons ($\leq$ 200 KV), electron current ($\leq$ 1 mA), and target spot size (5 to 1000 μm). The term "microfocus" refers to any generator that has a target spot size less than 0.1 mm (ASTM E 1255-88, 1988). A 10 μm spot size was used for this work.

Ideally the X-ray source would be a point source, since geometric unsharpness blur results from a finitely-sized source. Unsharpness is caused whenever the sample is placed somewhere between the source and detector instead of in contact with the detector. Figure 2.2 shows a diagram of this situation for the image of a step edge. The microfocus source is a good approximation to a point source, and permits the detected image to be magnified up to 100 times. Magnification is a simple way to offset limited resolution in the detector at the cost of a reduced field of view.

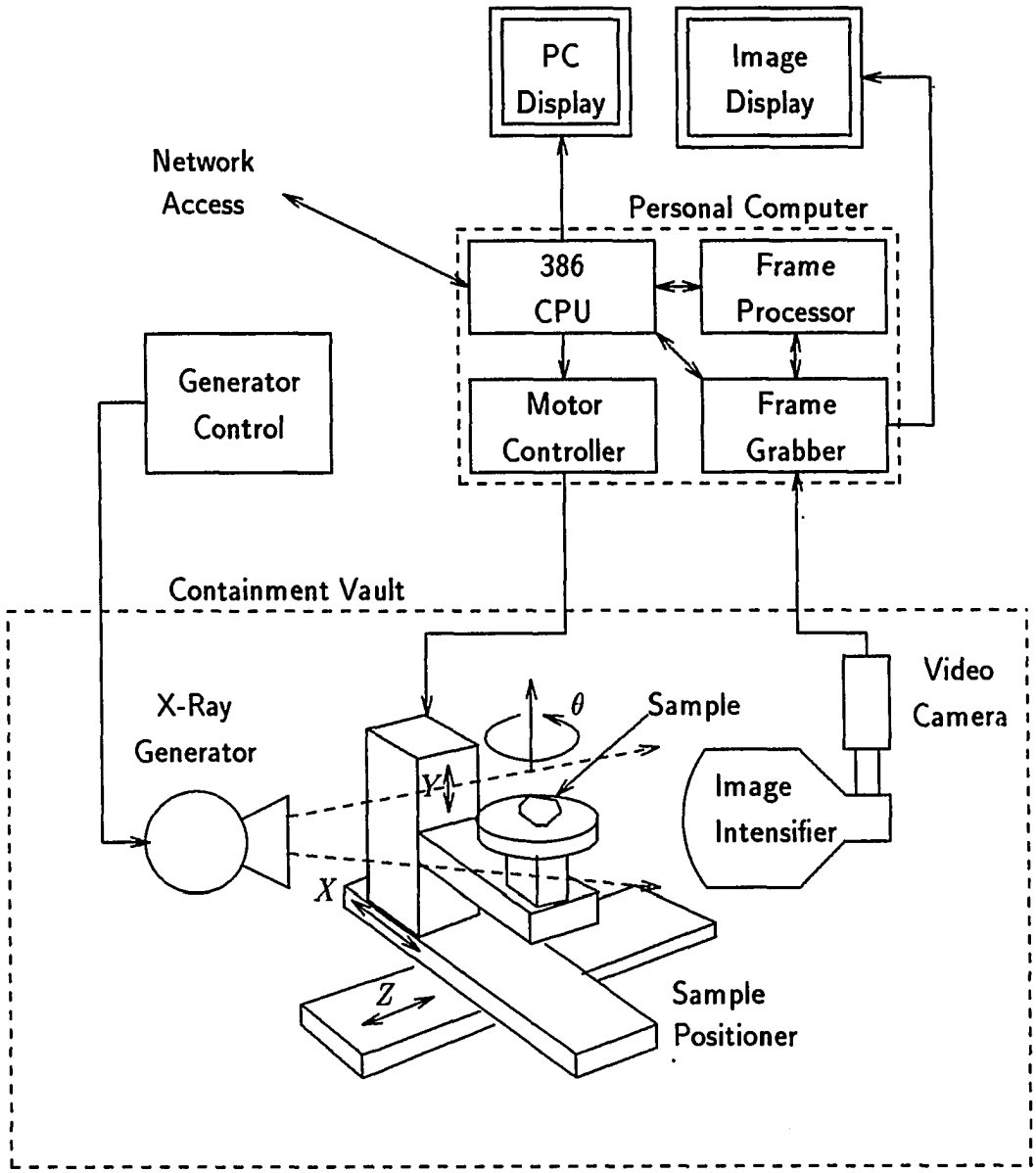

Figure 2.1: Real-time radiography laboratory equipment

Figure 2.2 also shows the magnification equation and how it is related to geometric unsharpness.

The small spot size of the microfocus source limits the amount of power per unit area that can be absorbed by the target without severe pitting or melting. Tungsten has high thermal conductivity, and water is pumped through the target to carry away the excess heat. This technique permits the X-ray tube to be operated at up to 200 KV at 1 mA of current. This is a relatively low power output compared to conventional broad focus sources (spot size 1–2 mm) which operate at energy levels up to 500 KeV. Thus microfocus-based inspection restricts the types of samples that can be imaged to thin, low density, or low atomic number materials.

Sample positioner

The sample positioner has three translational axes and two rotational axes. Each axis is moved by a wormscrew controlled by a high resolution stepper motor. The translation axis motors have a resolution of 100,000 steps/inch and the rotation axis motors have 10,000 steps/degree resolution. The positional accuracy is a non-cumulative error of 3-5% over one revolution of the motor.

The stepper motors are actuated by a series of pulses generated by PC-compatible indexer cards. These cards accept command strings (sequences of ASCII characters) from a program running on the host computer. These commands set up acceleration and velocity profiles to be used to move the sample from one position to another. The commands are easily incorporated into any program that needs to control a sample's position, e.g., a CT data collection routine. A program was also developed for interactive joystick control of the sample position. This program is used by the

Magnification, M **Geometric Unsharpness, U_g**

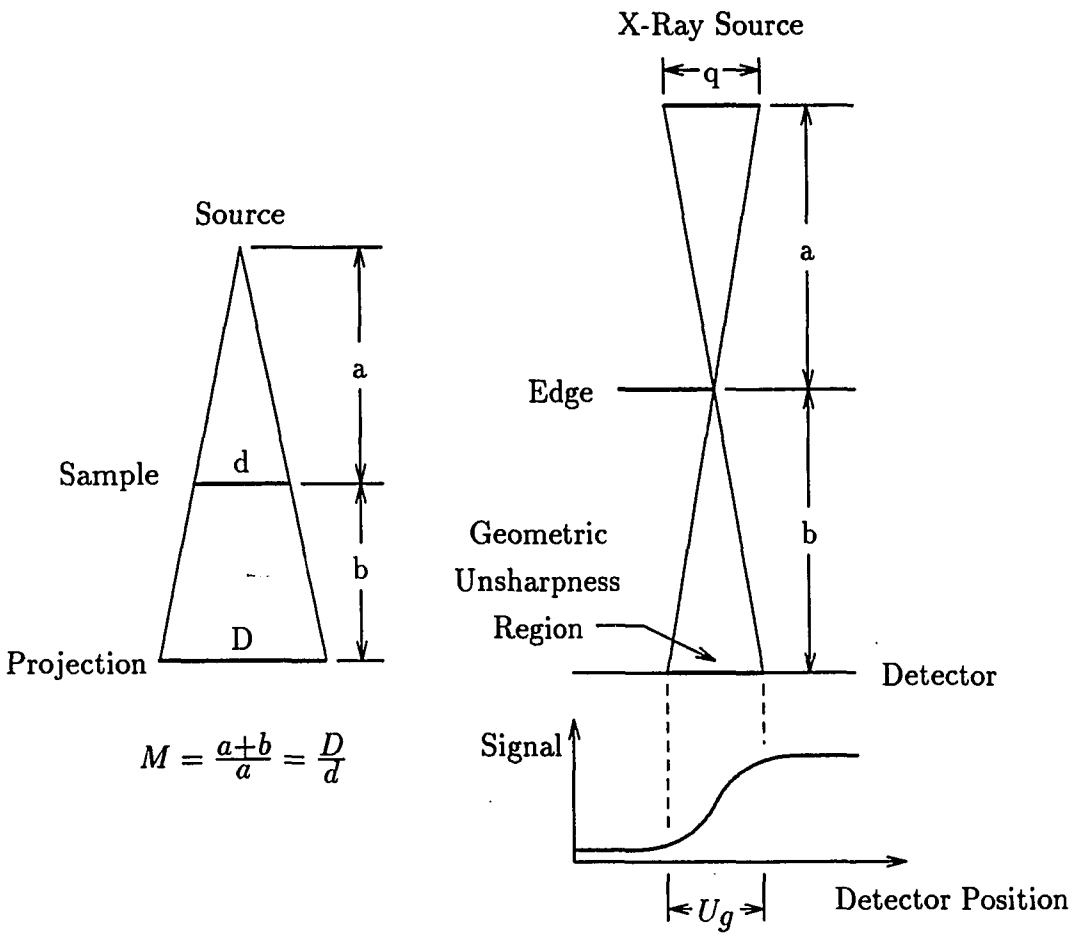

$$M = \frac{a+b}{a} = \frac{D}{d}$$

$$U_g = \frac{b}{a}q = q(M-1)$$

Figure 2.2: Magnification and geometric unsharpness

operator to manipulate the sample while viewing the real-time X-ray image. This routine optionally updates the sample's coordinates in a shared data file, so other programs can access this information while the operator moves the sample.

Image intensifier

The electrostatic inverting image intensifier is the X-ray-to-light conversion device used for this project, and determines the overall image quality of the real-time X-ray imaging system. The operation of this device and the image processing routines used to overcome its design limitations are discussed thoroughly in Chapter 4. This section highlights the specifications of the particular tube used for making X-ray measurements.

The image intensifier has a 15 cm diameter input screen and a 1.5 cm diameter output screen. The primary specifications for this unit are conversion efficiency, contrast ratio, and resolution. Conversion efficiency is the ratio of the output image brightness to the incident X-ray flux. Image brightness is measured in candelas per square meter (cd/m^2) and X-ray flux is measured in milliRoentgens per second (mR/s). For this tube the conversion efficiency is 180 $cd \cdot s/mR \cdot m^2$. Contrast ratio is determined by affixing a lead disk to the center of the input screen. The diameter of the lead disk is 10% of the input screen diameter, or 1.5 cm. The contrast ratio is the ratio between the maximum output brightness measured away from the disk and the minimum brightness observed under the disk; for this tube it is 22:1. Resolution is determined by attaching a standard X-ray chart (Type 6 Funk's X-ray chart) to the input screen and observing the output image with a microscope. The resolution is specified as 44 line pairs per centimeter (lp/cm) for this unit. This image intensifier

is an "E"-series tube manufactured in 1987. Manufacturers of image intensifiers are now producing "H"-series tubes which have higher contrast ratio (at least 30:1) and higher resolution (58 lp/cm) (Precise Optics, 1991). The performance of image intensifier tubes degrades approximately 10% per year (Corso, 1992), so the specified resolution is only valid when the tube is new.

Video camera

A CCD (charge-coupled device) camera converts the optical output of the image intensifier to an RS-170 video signal. CCD (charge coupled device) video cameras inherently have negligible spatial distortion. The detector array is fabricated as an integrated circuit, so uniformity of the array is controlled to within fractions of a micrometer. CCD arrays are now available in 1K×1K sizes, thus making them competitive resolution-wise with vidicon tubes. Until recently, vidicon tubes were preferred for higher resolution. However, tube-based cameras have significant amounts of spatial distortion. This distortion is irregular (and thus difficult to model) and time-varying (Frobin and Hierholzer, 1991). For example, a commercially available Newvicon tube-based video camera was characterized for its power-up spatial and gray level response; a nine pixel shift occurred in the first 10 minutes, and 120 minutes were required to stabilize the gray level from a 7% deviation from its final value (Doering and Basart, 1991a).

Frame digitizer

The Data Translation DT2867 frame grabber converts the video camera signal to a digitized image. This board is well-suited to the needs of real-time radiogra-

phy. The main features of the board are a 16-bit image buffer for video-rate true frame averaging (add N video frames together and divide by N) and a high speed image transfer bus which operates at 10 MBytes/second. Frame averaging makes the greatest contribution to image quality; successive processing only improves the presentation of the image for the operator (Munro, *et al.*, 1987). Frame averaging increases the signal-to-noise ratio (SNR) proportional to $\sqrt{N}$ (Mengers, 1980), and is an alternative to increasing the image intensifier screen efficiency (Link *et al.*, 1989). The high speed bus connects directly to the frame processing device rather than passing the image data through the PC's bus.

The image is digitized to a 640×480 8-bit image. These dimensions match the 4:3 aspect ratio of the RS-170 video signal yielding equal sampling frequencies in the horizontal and vertical directions. This creates an image with square pixels to simplify quantitative sizing applications. In addition to the 16-bit buffer, two 8-bit buffers are available for secondary image storage and display. The display section is configurable to use one buffer for image display and another buffer for nondestructive overlay graphics. Data Translation provides no graphics routines, so functions were created for drawing text and graphical objects such as cursors, marks, lines, and boxes. These functions were used to develop mouse-oriented routines for choosing points and regions of interest directly on the image display.

Three ALU/multipliers operating at 25 MHz perform real-time image preprocessing operations such as convolution filters and morphological processing. The ALUs and other parameters of the board are controlled by a program running on the host computer. The frame grabber does not have any high-level on-board control capability. This is a primary drawback of the board for real-time processing since

the computer must remain in intimate control over all aspects of the board at all times. The frame grabber is capable of digitizing at the video frame rate, but the additional tasks needed during the real-time loop limit the overall performance to 10 fps. However, a minimum of 4 to 8 frames need to be averaged to achieve a good signal, so this limitation is usually not a problem. The computer controls the frame grabber through the PC bus, which is the bottleneck for this system. In contrast, the frame processor (described in the next section) operates independently of the host computer.

Frame processor

The Ariel MM-96 DSP (digital signal processing) plug-in board for the PC computer processes the acquired image. This board is based on the Motorola 96002 32-bit floating point DSP processing chip. It is a member of a new generation of processors specifically designed for the computational needs of DSP, i.e., fast memory access and fast multiplication. It operates at 16.5 MIPS (millions of instructions cycles per second) and has a theoretical peak of 50 MFLOPS (millions of floating point operations per second). The MFLOPS rating is greater than the MIPS rating since pipelining of the single-cycle multiplier and arithmetic logic unit (ALU) allows up to 3 floating point operations to be carried out in one instruction cycle; in practice this cannot be sustained continuously, hence the use of the phrase "theoretical peak." Two 96002 processors are available for a total of 100 MFLOPS. Each processor has 64 Kwords of private zero-wait-state SRAM (static random access memory). The SRAM is used for program memory and data cache memory. Both processors share 4 Mwords of

1-wait-state DRAM (dynamic RAM) for large data and image arrays. Image data is passed to the Data Translation board via the high speed image transfer bus.

An Intermetrics optimizing C compiler and Spectron Microsystems SPOX DSP operating system are supplied with the board. Traditionally, DSP boards are programmed in assembly language specifically tailored to the architecture of the processor to achieve efficiency. The optimizing C compiler allows the software developer to code in a portable high level language, thus simplifying the design and maintenance of the software. The SPOX operating system is an emerging standard for DSP plug-in boards. It provides an interface to the PC resources (e.g., files, keyboard, and screen), memory management tools, and object-oriented functions that operate on matrices and vectors directly. At this time, the SPOX operating system only runs on a single processor, so half of the board's capacity is not being utilized.

Achieving speed performance is highly dependent on how the DSP chip is programmed. It is commonly held that assembly level programming is required to get close to the theoretical performance. However, this is costly in terms of initial program development and subsequent maintenance. A compromise is to program in C for I/O, memory management, and flow control, and in assembly language for the time-critical portions of the code (Terry, 1990).

To test this approach, an image division routine was implemented as a benchmark program. The function is

$$y(i,j) = \frac{x(i,j)}{d(i,j)}s + o, \tag{2.1}$$

where $x(i,j)$ is the input image, $d(i,j)$ is the divisor image, s is a scalar, o is an offset, and $y(i,j)$ is the output image. This was implemented first using a standard C program. The second implementation used 96002 assembly language for the math

computation. The program execution was timed, and the average of five runs was used as the amount of time needed to process the image. Figure 2.3 shows the performance of these two implementations relative to a DECstation 5000 workstation; a variety of other workstations are also shown for comparison. A 256×256 image was used, and the performance measure was computed using pixel operations per second (POPS). The DECstation 5000 operated at 408 KPOPS. Note that the MM-96 assembly version ran 4 times faster than the C version.

While the 96002 is not as well-suited to the requirements of C compilers compared to RISC (reduced instruction set computer) chips such as the Intel i860, the 96002 is better suited for numerical computation due to its single-cycle multiplier (Wilson, 1992). Assembly-level programming is necessary to realize the computing performance available in the 96002. Fortunately, the C language can be used to develop the overall control structure of the program (including I/O and memory management); assembly-level programming is only required for computationally intensive and time-critical portions of the code.

Host computer

The Innovation 386 computer is used as the control center for the position control, frame digitizer, and frame processor cards. This computer was specially designed to be IBM PC-compatible, yet have 20 expansion slots rather than the standard 6 slots. The extra slots are used to provide enough space for the cards mentioned above as well as a variety of other X-ray detectors and peripheral devices not specifically used for the real-time environment. An 660 MByte hard disk is provided for im-

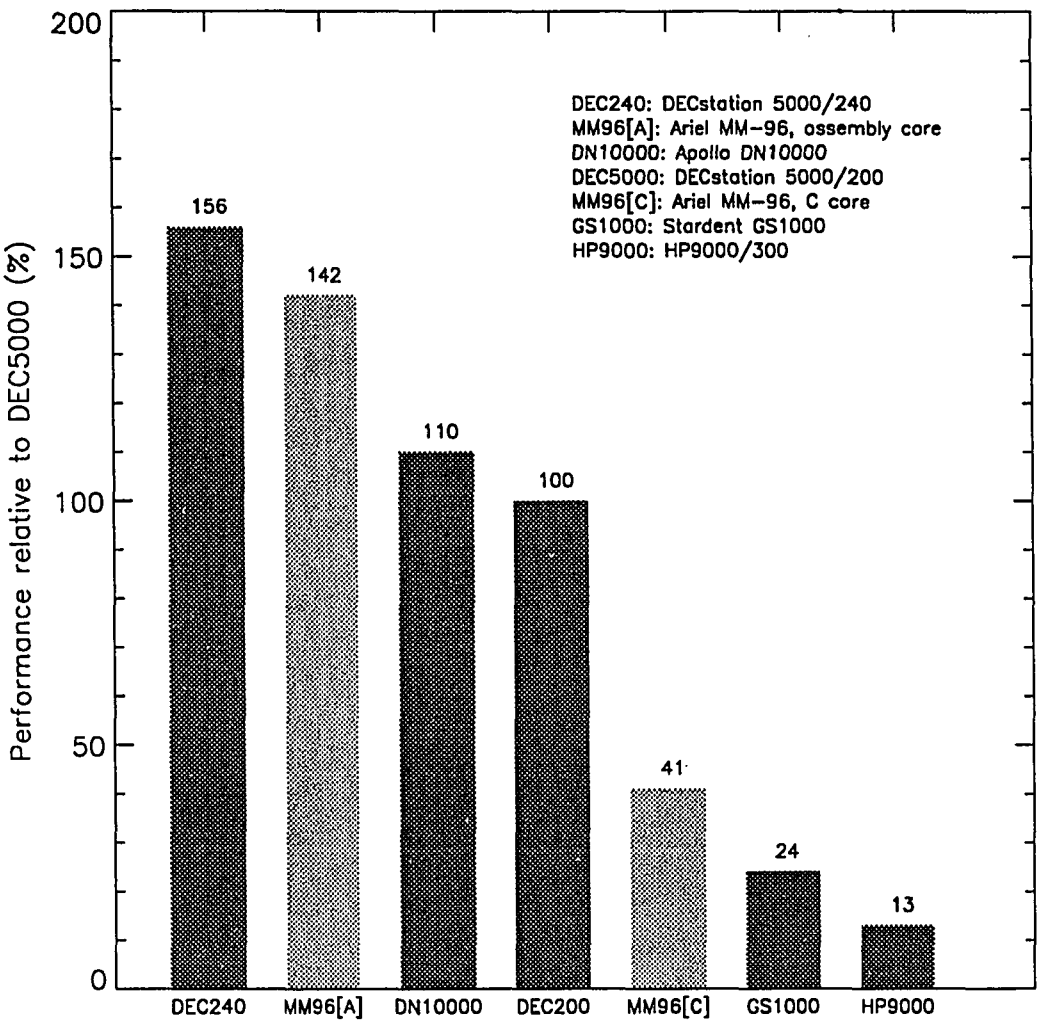

Figure 2.3: Performance of Ariel MM-96 compared to workstations

age and data storage. A high speed data link is used to transfer images to other computers for off-line analysis.

Data Flow and System Control

This section describes how all the separate pieces of equipment work together to provide a unified system for making X-ray NDE measurements. Figure 2.4 shows a flow diagram of this process. The data flow begins with the X-ray source. The X-ray beam passes through and interacts with the sample to generate an image of the sample's interior. This image is observed by the detector consisting of the image intensifier, video camera, and frame digitizer. The frame store is operated as an accumulator during frame averaging to emulate film integration. Averaging 4 to 8 frames significantly improves the signal-to-noise ratio. The frame processor is brought in to the flow when the image data needs to processed. The resulting image is displayed on the image monitor and finally viewed by the operator.

The operator must run three control programs on the host computer. DOS (disk operating system) is a single-user, single-task operating system, so normally this would not be possible without bundling all three (large) programs into a single program. Desqview, a commercially available package, multiplexes the PC's CPU between multiple windows to create a multi-tasking environment which simultaneously runs the sample positioner, frame digitizer, and frame processor interface programs. Each program runs concurrently in a separate window on the PC monitor, although only one window is active for user input at a time.

The sample positioner routine displays the coordinates of the sample and provides an interface to the motor control cards. The arrow keys are used to select

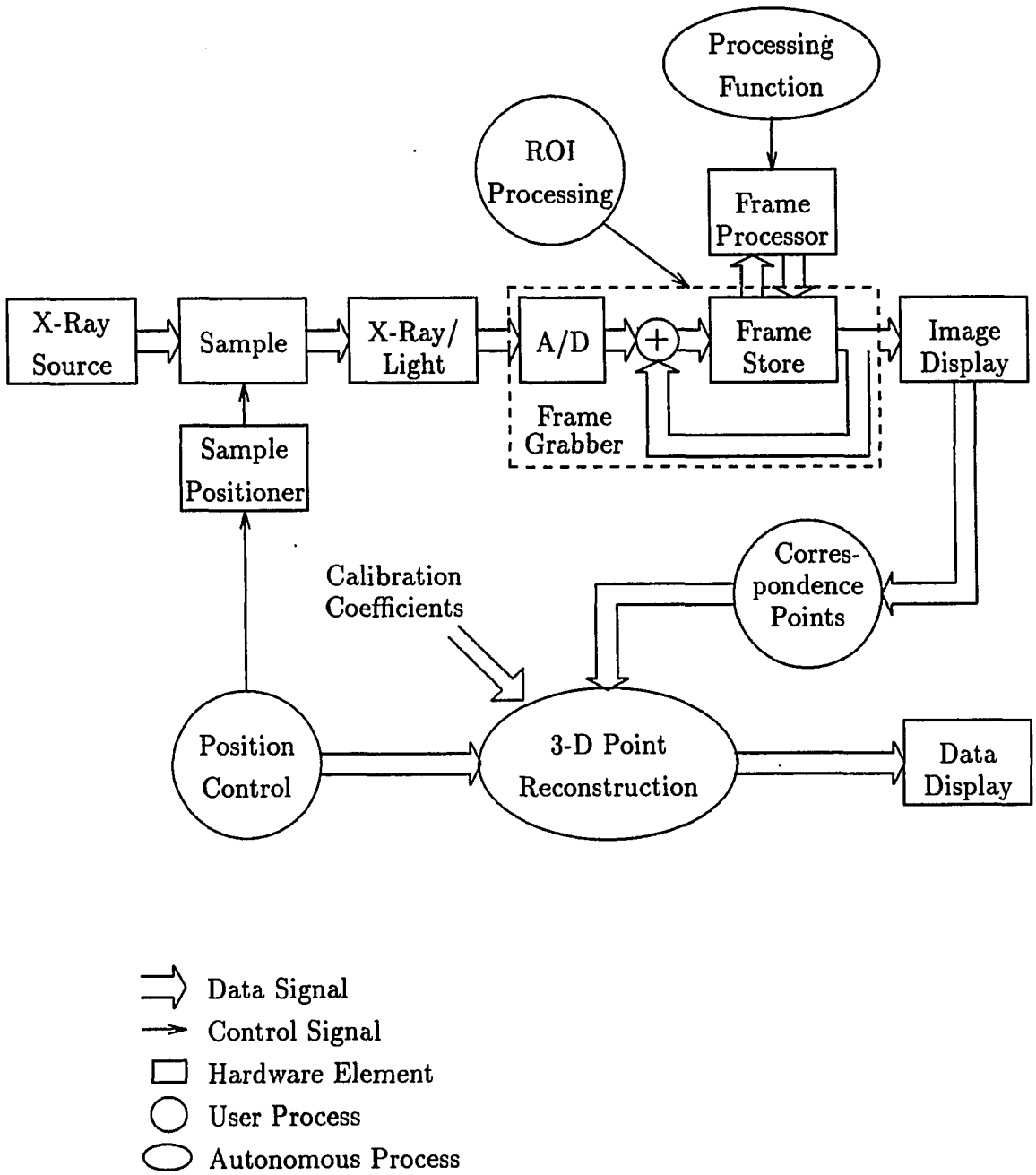

Figure 2.4: Data flow and system control for real-time radiography laboratory

among the axes and to start and stop sample motion on a particular axis. The position display is continuously updated to the PC screen and is optionally written to a shared data file read by other programs that require the sample position.

The frame grabber routine communicates with the frame grabber board through a non-sharable DOS device driver, so only one process can control the frame grabber at a time. Data Translation provides a C function library to interface with the device driver. This makes it easy for any program running on the PC to have access to the frame grabber. A variety of stand-alone programs were developed to handle routine tasks for for image acquisition, display, storage, and analysis. These do not require the multi-tasking environment. The 3-D reconstruction routine, however, requires the multi-tasking environment to read the sample position and to coordinate activity between the frame grabber and the frame processor.

The frame processor interface routine provides the link between DOS and the MM-96. The program begins by downloading and starting the SPOX operating system and 96002 executable onto the MM-96. Afterwards, the program waits for any requests from SPOX for DOS resources. For example, the C program running on the MM-96 can open a data file, read from the file, and close it. SPOX relays these requests to the interface program running on the PC. The interface routine is the program that actually operates on the DOS file. Aside from DOS requests, the MM-96 program runs independent of the PC. To improve operating efficiency of the sample positioner and frame grabber programs, the frame processor interface program is operated in the background without receiving CPU cycles once the MM-96 program is running.

Real-time processing loop

The frame digitizer and frame processor are set up to perform a real-time processing loop. The image transfer functions of this loop are indicated in Figure 2.5. The frame grabber is controlled by the host computer to perform the four steps indicated by the circled numbers in the diagram. The purpose of this program is to act as an image server for the processing board. Once initialized, the client program running on the frame processor operates independently of the host computer since DOS resources are not accessed inside the real-time processing loop. Its operation sequence is indicated by the boxed numbers.

The image server begins by acquiring a frame-averaged image into the 16-bit averaging buffer of the frame digitizer in Step 1. The buffer is first initialized to zero, then N frames ($1 \leq N \leq 255$) are digitized by the analog-to-digital convertor (A/D) and summed together. The image is subsequently divided by N. In Step 2, a sub-image or region-of-interest (ROI) is sent via the high-speed image bus to the frame processor. The most recently processed image is immediately received from the processor and inserted into the ROI (Step 3) rather than waiting for the frame processor to finish with the current ROI. This allows the frame averaging and frame processing functions to operate in parallel. The only disadvantage of this technique is that the processed image lags the unprocessed image by one display frame. In Step 4, the composite image is sent to the display buffer.

The image client program running on the frame processor is designed to access any files or data as part of an initialization step since any access to DOS resources is slow. It subsequently enters an infinite processing loop. In Step 1 of this loop, the frame processor loads the ROI from the frame digitizer into the input image buffer.

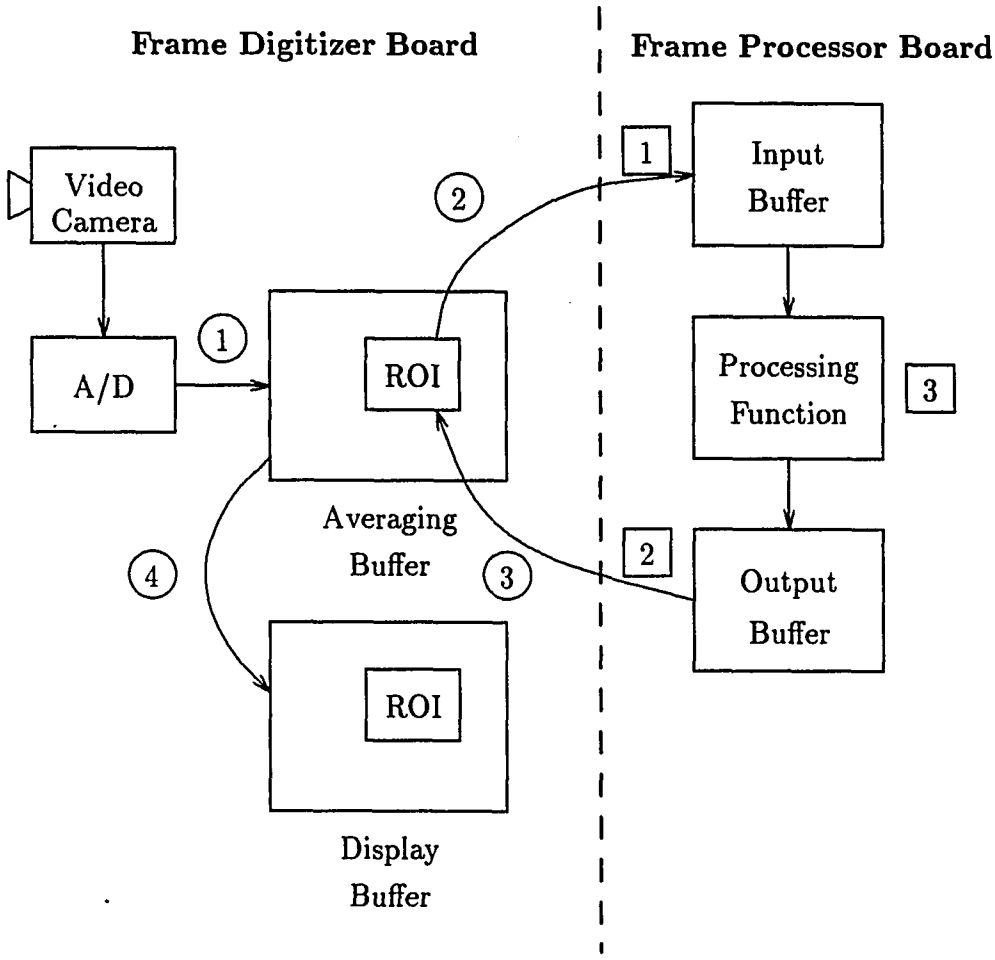

Figure 2.5: Real-time image processing loop functions

Step 2 is executed immediately and the output image buffer is sent back to the frame digitizer. Step 3 follows and the input image buffer is mapped onto the output image buffer using whatever processing function the user has programmed. To use a new processing function, the user must terminate the frame processor interface program externally (from the operating system) and execute a new program.

The user interface to the image server accepts control information from the keyboard and the mouse. Moving the mouse continuously adjusts the position of the region of interest, thus permitting a high degree of interaction with the image. The ROI size is selectable as any sub-image of the 640×480 image. Keyboard input is used to control the number of frames averaged, to toggle the enhancement ROI on and off, and to send processing parameters to the frame processor client program. Prior to sending the unprocessed ROI, the image server sends a parameter array to the client program. The array is physically located in frame grabber memory which is accessible by the high speed image transfer bus, thus eliminating the need to send data through the slower PC bus.

The first four integer values of the array indicate the size and location of the ROI. The location is required for some algorithms that register the ROI with a previously stored image, such as background division of a flat-field calibration image. Additional integer or floating point parameters are user-specified. For example, suppose the image client is performing background subtraction by polynomial fitting and follows this with a contrast stretch. It requires the maximum polynomial order for the fit and a number to scale the residual image. The image client is set up to take the polynomial order as an integer from the fifth value of the parameter array and the scalar as a floating point value from the sixth value of the array. The user sets

a parameter value by initiating the appropriate image server command (pressing "P" on the keyboard). The image server prompts for the type (integer or floating point) and value. This updates the parameter array sent to the image client and the processing results using the updated parameters are viewed immediately.

The image server was programmed as a stand-alone program and also as a function. The function is used by the 3-D reconstruction program to do real-time processing before each feature point is selected from the screen. The image server has user commands to display the update rate, to set the device-driver time-out value (this is important when it takes a long time to process an image), to pause while a new frame processor routine is loaded, and to temporarily release the frame grabber device driver. This last capability makes it possible to use the other stand-alone programs to modify the frame grabber parameters such as zoom, video A/D gain and offset, and look-up tables.

3-D point reconstruction

After moving the sample to its initial position and enhancing the features of interest, a mouse-guided cursor is used to choose the 2-D projected coordinates from the display screen. An arbitrary number of points can be selected; each is reconstructed independently of the others. When all points are entered, the reconstruction program reads the current sample position from a shared data file written by the positioner control program. The user is prompted to move to a new orientation and select the corresponding points. Labeled marks are placed over the selected points as a visual aid to indicate the order of points to select. The new sample coordinates are read after all the corresponding points are entered. This process continues until the user

signifies that data collection is complete. The point reconstruction program calculates the 3-D coordinates of each point and displays this information numerically on the data display. A simple data visualization was also implemented to show the 3 coordinate planes XZ, XY, and YZ.

The laboratory geometry is stored in a file to initialize the 3-D reconstruction routine. This information includes the X-ray source position, sample positioner center of rotation, detector calibration coefficients, and transformations to convert device units into physical units. These transformations also convert the local coordinate systems of the positioner and display to the laboratory global coordinate system. The detector calibration is required to linearize the spatial response of the image intensifier. Chapter 5 describes an image-based technique to obtain the laboratory geometry, and Chapter 3 describes the calibration and image processing techniques used to improve the detector performance.

CHAPTER 3. 3-D FLAW RECONSTRUCTION

This chapter describes the mathematical foundation used to reconstruct the three dimensional coordinates of flaws and other features of interest within a host material. This method is restricted to determining *point* locations as opposed to computed tomography methods which reconstruct a map of the entire X-ray attenuation of a sample cross-section. Determining the coordinates of only the points of interest is much more computationally efficient, and often provides sufficient information for an NDE practitioner to make a decision.

The point reconstruction method developed for this work is called the *generalized stereography* (GS) method. It closely resembles the work of Wallingford (1990); the main differences are the generalized approach for sample manipulation and the elimination of nuisance parameters in the system inversion. Wallingford's work as well as other well known methods for determining flaw depth are briefly described prior to deriving the GS equations.

The chapter concludes by describing how to incorporate the GS equations into a real-time radiography system. A simulation of the measurement process (forward model) and the solution process (inverse model) is used to gain insight into the error sensitivity of the system under a variety of operational configurations.

Existing Methods

Stereoradiography (Quinn and Sigl, 1980) is a qualitative technique based on the same principle as a stereoscopic photograph viewer. Two radiographs of the sample are required. Between exposures, the X-ray source is shifted a distance equal to the spacing of the human eyes. These radiographs are placed in a stereoscopic viewer, and the operator perceives the depth of flaws within the sample. Perceiving the orientation of the feature within the part is aided by placing a uniform grid of lead wires around the sample or by painting lead stripes on the sample (Veress, 1989).

Stereo X-ray photogrammetry (Veress, 1989) is a quantitative version of stereoradiography. X-ray photogrammetry is based on a central projection model which assumes a point X-ray source and straight line propagation of the X-rays. The latter condition holds due to the nature of electromagnetic wave propagation. The former condition of a point source is not realized in an actual X-ray source, and the ensuing geometric unsharpness makes feature identification more ambiguous. The microfocus source, however, is an extremely good approximation to an ideal point source, so unsharpness problems are minimized. The straight line propagation of the X-ray path implies a collinear relationship between the X-ray source, feature point, and detector points. McNeil (1966) identifies four types of X-ray photogrammetric lab setups: (1) two stationary sources with a stationary object, (2) translation of a single source with stationary object, (3) stationary source with object translation, and (4) stationary source with object rotation. In all cases the object is kept in contact with the X-ray film detector. Case (4) is preferred since equipment complexity is minimized. Case (3) requires a significant amount of translation, so the X-ray source must be rotated between views. X-ray photogrammetric techniques emphasize system calibration as a

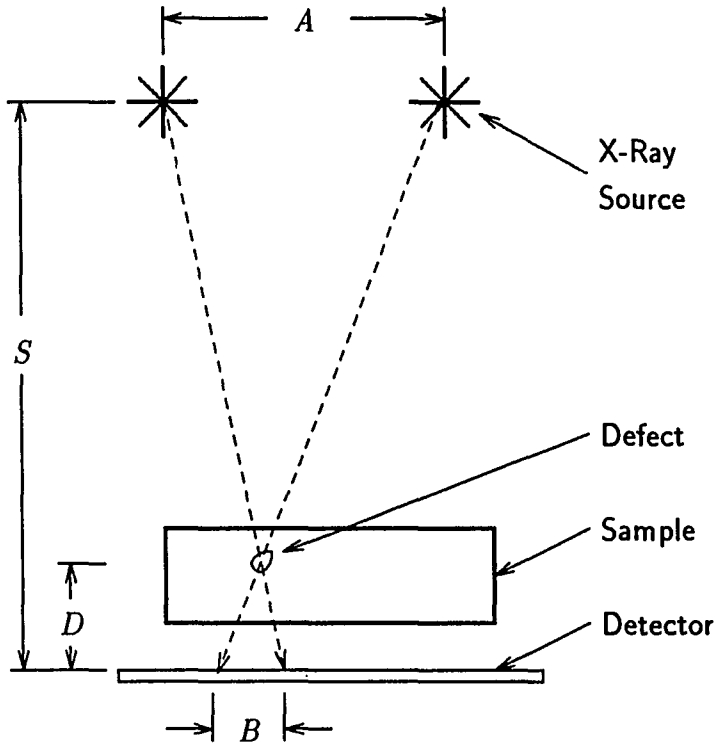

Figure 3.1: Parallax method for measuring depth of a flaw in a material

means to achieve low measurement errors, e.g., ±0.004 cm in depth (Veress, Lippert, and Takamoto, 1977).

The *parallax method* (Bryant and McIntire, 1985) uses source shifting and similar triangle relationships to quantitatively determine flaw depth within a sample. Figure 3.1 shows a diagram of the parallax radiography setup. The X-ray source is translated a known distance A in a line parallel to the X-ray detector. This produces a corresponding shift B in the image of the flaw on the film. The objective is to determine the flaw distance D above the detector plane. Knowing the source-to-detector

distance S, the rule of similar triangles implies

$$\frac{B}{D} = \frac{A}{S-D}. \tag{3.1}$$

Solving for D yields

$$D = \frac{SB}{A+B}. \tag{3.2}$$

This technique requires the source shift and source/detector distances to be known accurately. Furthermore, since the result of the method is the flaw height above the detector, the sample thickness and position relative to the detector must be accurately known as well to properly locate the flaw relative to the boundaries of the sample. This problem is alleviated by applying lead markers on the source side and detector side of the sample. The formula of Equation (3.2) is applied for both markers. This determines the boundaries of the sample relative to the detector, so knowledge of the sample thickness is not required.

Stereography (Wallingford, 1990) is a method for reconstructing the three dimensional coordinates of feature points within a sample. This approach uses a sample shift rather than a source shift. The method was implemented using both X-ray film and the real-time detector. A pair of images is collected and input to an off-line program to compute the feature depth.

The X-ray source position is indicated by the vector $\vec{S} = S_x\hat{\imath} + S_y\hat{\jmath} + S_z\hat{k}$. The ray connecting the source, the point of interest $\vec{P}$, and the measurement point $\vec{M}$ in the detector plane is described by the parametric equation $\vec{R}(t) = \vec{S}(1-t) + \vec{M}(t)$. As t varies from 0 to 1, $\vec{R}(t)$ traces out the ray from the source to the measurement point. The vector $\vec{R}(t)$ coincides with $\vec{P}$ at some value of $t = t_1$. The sample is shifted an amount T in a line parallel to the X-ray detector plane. This translates

the point of interest to a new position $\vec{P}'$ which projects a new measurement point at $\vec{M}'$. The new ray selected by $\vec{S}$, $\vec{P}'$, and $\vec{M}'$ is described by a second equation $\vec{R}'(t)$. It coincides with $\vec{P}'$ at $t = t_2$. These two measurements yield a system of equations which is inverted to solve for the unknown values P_x, P_y, P_z, and the "nuisance parameters" t_1 and t_2.

Wallingford demonstrated that this technique could easily accommodate additional measurements to produce a least-squares estimate of the point position $\vec{P}$. Furthermore, he derived an extension of the method which could accommodate sample rotation as well as translation. In the subsequent derivation, the sample manipulation is generalized using a linear transformation of the form $\mathbf{y} = \mathbf{Ax} + \mathbf{b}$. This transformation permits the sample to be manipulated in a more complex manner than simple translation.

The main drawback of the parametric approach is that a new parameter t_i is introduced for each new measurement. The point of interest $\vec{P}$ and its translates $\vec{P}_i$ are functions of these parameters, so there is redundancy in this system formulation. In the following derivation, the fact that $\vec{S}$, $\vec{P}$, and $\vec{M}$ are collinear is expressed using a cross product approach rather than a parametric equation approach. This non-parametric method is free of nuisance parameters.

Mathematical Formulation

The following derivation is designed for a fixed-position X-ray source, a fixed-position X-ray detector, and a movable sample. This is a limitation of the particular RTR laboratory used for this work (i.e., the X-ray source and detector positions are

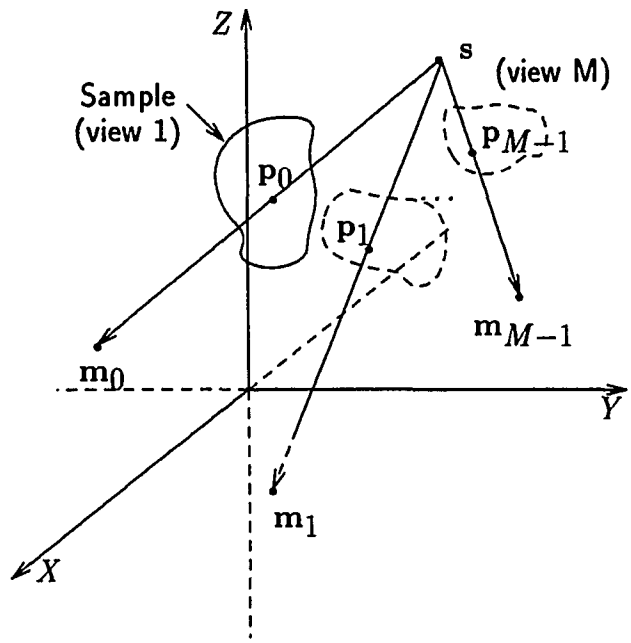

Figure 3.2: Experiment geometry for generalized stereography

not computer controlled). However, this method can easily be reformulated in terms of a movable source and a fixed sample.

Figure 3.2 shows a diagram of the experiment geometry. The X-ray source location is denoted by the 3×1 vector $\mathbf{s} = [s_1\ s_2\ s_3]^T$ (the vector indices 1, 2, and 3 correspond to the X, Y, and Z axes, respectively, of the global coordinate system; this convention is used throughout the derivation). The X-ray source produces a cone beam which is modelled by a series of rays emanating from s. One of these rays passes through the point of interest $\mathbf{p}_0$ (also called the range point) and casts a shadow (projection) on the X-ray detector at the measurement point $\mathbf{m}_0$. Note that no particular detector geometry is assumed here, so the choice of $\mathbf{m}_0$ in three dimensions is perfectly general. For example, the spherical surface of the image

intensifier could be used directly rather than assuming a planar detector. The point $\mathbf{p}_0$ is embedded within a host material, so only s and $\mathbf{m}_0$ are known.

The goal of the reconstruction is to uniquely identify the 3-D coordinates of $\mathbf{p}_0$. It is known that $\mathbf{p}_0$ is collinear with the source point and measurement point since all three points lie on the same ray. Yet this is insufficient information to uniquely determine $\mathbf{p}_0$ since any position along the ray satisfies the collinearity constraint. Additional information is obtained by translating $\mathbf{p}_0$ to a new location $\mathbf{p}_1$, which selects a new ray and creates the measurement point $\mathbf{m}_1$. $\mathbf{p}_0$ is transformed to $\mathbf{p}_1$ using the linear transformation $\mathbf{p}_1 = \mathbf{A}\mathbf{p}_0 + \mathbf{b}_1$. Simple translation is accomplished by taking $\mathbf{A}_1$ as the identity matrix and $\mathbf{b}_1$ as a non-zero vector. Rotation about a center of rotation $\mathbf{c}$ is accomplished by subtracting $\mathbf{c}$ (this takes $\mathbf{p}_0$ to the origin), applying the rotation matrix $\mathbf{R}$, and adding back $\mathbf{c}$ to restore the original position:

$$\begin{aligned} \mathbf{p}_1 &= \mathbf{R}(\mathbf{p}_0 - \mathbf{c}) + \mathbf{c} \\ &= (\mathbf{R}\mathbf{p}_0 - \mathbf{R}\mathbf{c}) + \mathbf{c} \\ \mathbf{p}_1 &= \mathbf{R}\mathbf{p}_0 + (\mathbf{I} - \mathbf{R})\mathbf{c}. \end{aligned} \tag{3.3}$$

For this transformation, $\mathbf{A}_1 = \mathbf{R}$ and $\mathbf{b}_1 = (\mathbf{I} - \mathbf{R})\mathbf{c}$.

The additional measurement point $\mathbf{m}_1$ and knowledge of how $\mathbf{p}_1$ is related to $\mathbf{p}_0$ provides sufficient information to find $\mathbf{p}_0$. This information is summarized as follows:

Condition 1: s, $\mathbf{p}_0$, and $\mathbf{m}_0$ are collinear,

Condition 2: s, $\mathbf{p}_1$, and $\mathbf{m}_1$ are collinear, and

Condition 3: $\mathbf{p}_1 = \mathbf{A}_1\mathbf{p}_0 + \mathbf{b}_1$.

Conditions 1 and 2 are constraints on the locations of the unknown point and its translate. Condition 3 indicates how the constraints are coupled together.

Any three points A, B, and C are collinear when the cross product product $\vec{AB} \times \vec{AC}$ equals zero. It will be convenient to define the cross product operation in matrix notation. In vector notation, the cross product of two vectors $\vec{A}$ and $\vec{B}$ is given by the determinant

$$\vec{A} \times \vec{B} = \begin{vmatrix} \hat{\imath} & \hat{\jmath} & \hat{k} \\ A_x & A_y & A_z \\ B_x & B_y & B_z \end{vmatrix},$$

where $\hat{\imath}$, $\hat{\jmath}$, and $\hat{k}$ are unit vectors in the X, Y, and Z directions, respectively. Expanding this determinant yields

$$\vec{A} \times \vec{B} = (A_y B_z - A_z B_y)\hat{\imath} - (A_x B_z - A_z B_x)\hat{\jmath} + (A_x B_y - A_y B_x)\hat{k}. \tag{3.4}$$

Using the correspondence $\mathbf{a} = [a_1 \ a_2 \ a_3]^T \leftrightarrow \vec{A} = A_x\hat{\imath} + A_y\hat{\jmath} + A_z\hat{k}$, the above expansion is written in matrix notation as

$$\begin{bmatrix} a_2b_3 - a_3b_2 \\ -a_1b_3 + a_3b_1 \\ a_1b_2 - a_2b_1 \end{bmatrix} = \begin{bmatrix} 0 & -a_3 & a_2 \\ a_3 & 0 & -a_1 \\ -a_2 & a_1 & 0 \end{bmatrix} \begin{bmatrix} b_1 \\ b_2 \\ b_3 \end{bmatrix}. \tag{3.5}$$

The operator which takes the 3×1 vector $\mathbf{a}$ onto the 3×3 matrix premultiplying $\mathbf{b}$ in the above equation is defined as $\mathbf{C_x}$, where

$$\mathbf{C_x} \equiv \begin{bmatrix} 0 & -x_3 & x_2 \\ x_3 & 0 & -x_1 \\ -x_2 & x_1 & 0 \end{bmatrix}. \tag{3.6}$$

Hence, $\vec{A} \times \vec{B}$ corresponds to $\mathbf{C_a b}$.

Now, the collinearity constraint of Condition 1 is expressed by equating the cross product of the the vector pointing from the measurement point to the source point

$(\mathbf{s} - \mathbf{m}_0)$ and the vector pointing from the measurement point to the range point $(\mathbf{p}_0 - \mathbf{m}_0)$ to zero:

$$\begin{aligned} \mathbf{C}_{\mathbf{s}-\mathbf{m}_0}(\mathbf{p}_0 - \mathbf{m}_0) &= \mathbf{0} \\ \mathbf{C}_{\mathbf{s}-\mathbf{m}_0}\mathbf{p}_0 &= \mathbf{C}_{\mathbf{s}-\mathbf{m}_0}\mathbf{m}_0. \end{aligned} \tag{3.7}$$

It is tempting to solve the above equation for $\mathbf{p}_0$; however, the rank of $\mathbf{C}_\mathbf{x}$ (denoted $\rho(\mathbf{C}_\mathbf{x})$) is ≤ 2, but $\mathbf{C}_\mathbf{x}$ is a 3×3 matrix. Thus, $\mathbf{C}_x$ is not invertable, so $\mathbf{p}_0$ cannot be determined uniquely. This further demonstrates the need for making more than one measurement to uniquely determine the range point.

Condition 2 is expressed in a like manner:

$$\mathbf{C}_{\mathbf{s}-\mathbf{m}_1}\mathbf{p}_1 = \mathbf{C}_{\mathbf{s}-\mathbf{m}_1}\mathbf{m}_1. \tag{3.8}$$

By Condition 3, $\mathbf{p}_1 = \mathbf{A}_1\mathbf{p}_0 + \mathbf{b}_1$, so by substitution into Equation (3.8),

$$\begin{aligned} \mathbf{C}_{\mathbf{s}-\mathbf{m}_1}(\mathbf{A}_1\mathbf{p}_0 + \mathbf{b}_1) &= \mathbf{C}_{\mathbf{s}-\mathbf{m}_1}\mathbf{m}_1 \\ \mathbf{C}_{\mathbf{s}-\mathbf{m}_1}\mathbf{A}_1\mathbf{p}_0 &= \mathbf{C}_{\mathbf{s}-\mathbf{m}_1}(\mathbf{m}_1 - \mathbf{b}_1). \end{aligned} \tag{3.9}$$

Combining Equations (3.7) and (3.9) forms the system

$$\begin{pmatrix} \mathbf{C}_{\mathbf{s}-\mathbf{m}_0}\mathbf{A}_0 \\ \mathbf{C}_{\mathbf{s}-\mathbf{m}_1}\mathbf{A}_1 \end{pmatrix}(\mathbf{p}_0) = \begin{pmatrix} \mathbf{C}_{\mathbf{s}-\mathbf{m}_0}(\mathbf{m}_0 - \mathbf{b}_0) \\ \mathbf{C}_{\mathbf{s}-\mathbf{m}_1}(\mathbf{m}_1 - \mathbf{b}_1) \end{pmatrix}, \tag{3.10}$$

where $\mathbf{A}_0 \equiv \mathbf{I}$ and $\mathbf{b}_0 \equiv \mathbf{0}$. This is an overdetermined system, so $\mathbf{p}_0$ is a least-squares solution. However, for the case of two measurements, the left-hand matrix has only six rows, so this particular system is only slightly overdetermined. The "overdeterminedness" of the system is improved by including additional measurements $\mathbf{m}_i$

obtained by applying a series of transformations to $\mathbf{p}_0$ to yield the set of range points $\mathbf{p}_i = \mathbf{A}_i\mathbf{p}_0 + \mathbf{b}_i$. A total of M measurements yields the general system

$$\begin{pmatrix} \mathbf{C}_{\mathbf{s}-\mathbf{m}_0}\mathbf{A}_0 \\ \mathbf{C}_{\mathbf{s}-\mathbf{m}_1}\mathbf{A}_1 \\ \mathbf{C}_{\mathbf{s}-\mathbf{m}_2}\mathbf{A}_2 \\ \vdots \\ \mathbf{C}_{\mathbf{s}-\mathbf{m}_{M-1}}\mathbf{A}_{M-1} \end{pmatrix} (\mathbf{p}_0) = \begin{pmatrix} \mathbf{C}_{\mathbf{s}-\mathbf{m}_0}(\mathbf{m}_0 - \mathbf{b}_0) \\ \mathbf{C}_{\mathbf{s}-\mathbf{m}_1}(\mathbf{m}_1 - \mathbf{b}_1) \\ \mathbf{C}_{\mathbf{s}-\mathbf{m}_2}(\mathbf{m}_2 - \mathbf{b}_2) \\ \vdots \\ \mathbf{C}_{\mathbf{s}-\mathbf{m}_{M-1}}(\mathbf{m}_{M-1} - \mathbf{b}_{M-1}) \end{pmatrix}. \quad (3.11)$$

The left matrix premultiplying $\mathbf{p}_0$ is a $3M \times 3$ ($M \geq 2$) rectangular matrix denoted $\mathbf{X}$. The right hand side is a $3M \times 1$ column vector denoted $\mathbf{y}$.

System Inversion

The system of Equation (3.11) is an overdetermined linear system of the form $\mathbf{Xp} = \mathbf{y}$, where the zero subscript has been dropped to simplify the following discussion. Solving for $\mathbf{p}$ requires computation of the matrix inverse of $\mathbf{X}$. $\mathbf{X}$ is rectangular, so only a generalized inverse $\mathbf{X}^-$ can be found. The solution vector is then $\mathbf{p} = \mathbf{X}^-\mathbf{y}$. When $\rho(\mathbf{X}^T\mathbf{X}) = 3$, $\mathbf{X}^T\mathbf{X}$ is a square matrix and is invertible. Thus, the most computationally straightforward solution is

$$\mathbf{p} = (\mathbf{X}^T\mathbf{X})^{-1}(\mathbf{X}^T\mathbf{y}). \quad (3.12)$$

Unfortunately, this method (known as solution of the normal equations) is prone to numerical instability, especially when $\mathbf{X}$ is ill-conditioned (Press *et al.*, 1988). The singular value decomposition (SVD) (Press *et al.*, 1988) approach is more numerically stable, and provides useful information concerning the quality of the solution vector $\mathbf{p}$.

The SVD decomposes $\mathbf{X}$ as follows:

$$\mathbf{X} = \mathbf{U}\mathbf{W}\mathbf{V}^T, \tag{3.13}$$

where $\mathbf{U}$ and $\mathbf{V}^T$ are orthogonal matrices, and $\mathbf{W}$ is a diagonal matrix containing the singular values w_i. The solution vector $\mathbf{p}$ is determined as

$$\begin{aligned} \mathbf{p} &= \mathbf{X}^{-}\mathbf{y} \\ &= (\mathbf{U}\mathbf{W}\mathbf{V}^T)^{-1}\mathbf{y} \\ &= (\mathbf{V}^T)^{-1}\mathbf{W}^{-1}\mathbf{U}^{-1}\mathbf{y} \\ \mathbf{p} &= \mathbf{V}\mathbf{W}^{-1}\mathbf{U}^T\mathbf{y} \end{aligned} \tag{3.14}$$

The last step follows since the transpose of an orthogonal matrix is its inverse; $\mathbf{W}$ is diagonal, so $\mathbf{W}^{-1}$ is found by taking the reciprocal of the diagonal elements.

The *condition number* of the matrix $\mathbf{X}$ indicates to what extent $\mathbf{X}$ is ill-conditioned for the least-squares problem. The condition number is the ratio of the maximum and minimum singular values:

$$CN = \frac{w_{max}}{w_{min}}. \tag{3.15}$$

$CN \simeq 1$ indicates a well-conditioned $\mathbf{X}$ matrix, while a large value indicates it is ill-conditioned (Press *et al.*, 1988). Furthermore, the sensitivity of the least-squares solution is proportional to the square of the condition number (Golub and Van Loan, 1989). In the laboratory software implementation, the condition number is included as an output to the user as a diagnostic to indicate how much confidence can be placed in the least-squares solution vector $\mathbf{p}$.

Application of Model in RTR Environment

This system computes the 3-D coordinates of a point $\mathbf{p}_0$ given a measurement point $\mathbf{m}_0$ derived from an initial view of the sample, a sequence of additional measurements $\mathbf{m}_1$, $\mathbf{m}_2$, ..., $\mathbf{m}_{M-1}$ derived from a series of new sample orientations defined by ($\mathbf{A}_i$,$\mathbf{b}_i$), and knowledge of the source location s. The sample positioner center of rotation is indicated by the 3×1 vector c. The angular position of the platter is denoted by θ.

Figure 3.3 shows a diagram of the coordinate systems used for the X-ray source, sample positioner, and detector. The global coordinate system (X_g, Y_g, Z_g) is centered on the face of the X-ray detector. The source is located somewhere in the positive Z_g half-space. A coordinate system local to the sample (X_s, Y_s, Z_s) is placed with its origin at c. Linear transformations are used to map device coordinates to the global coordinate system. For example, the sample positioner reports position in steps, and the display screen coordinates are reported in pixels. Both need to be converted into the global coordinate system in centimeter units.

The sample positioner lacks shaft encoders to provide an absolute position between invocations of the sample positioner program, so the positioner values are relative to the initial platter position c loaded from the laboratory geometry file. Once the sample is attached to the platter, the position is adjusted to obtain an initial view. A projection of a point of interest is defined from the image using a mouse-guided cursor to give the first measurement $\mathbf{m}_0 = [m_1\ m_2\ 0]^T$ (m_3 is always zero since the detector plane lies in the X_gY_g plane). The current position of the platter is recorded as $\mathbf{c}_0 = \mathbf{c} + \Delta\mathbf{c}_0$ and θ_0. The sample is translated and/or rotated to a new view. Once $\mathbf{m}_1$ is defined from the image, the sample position is

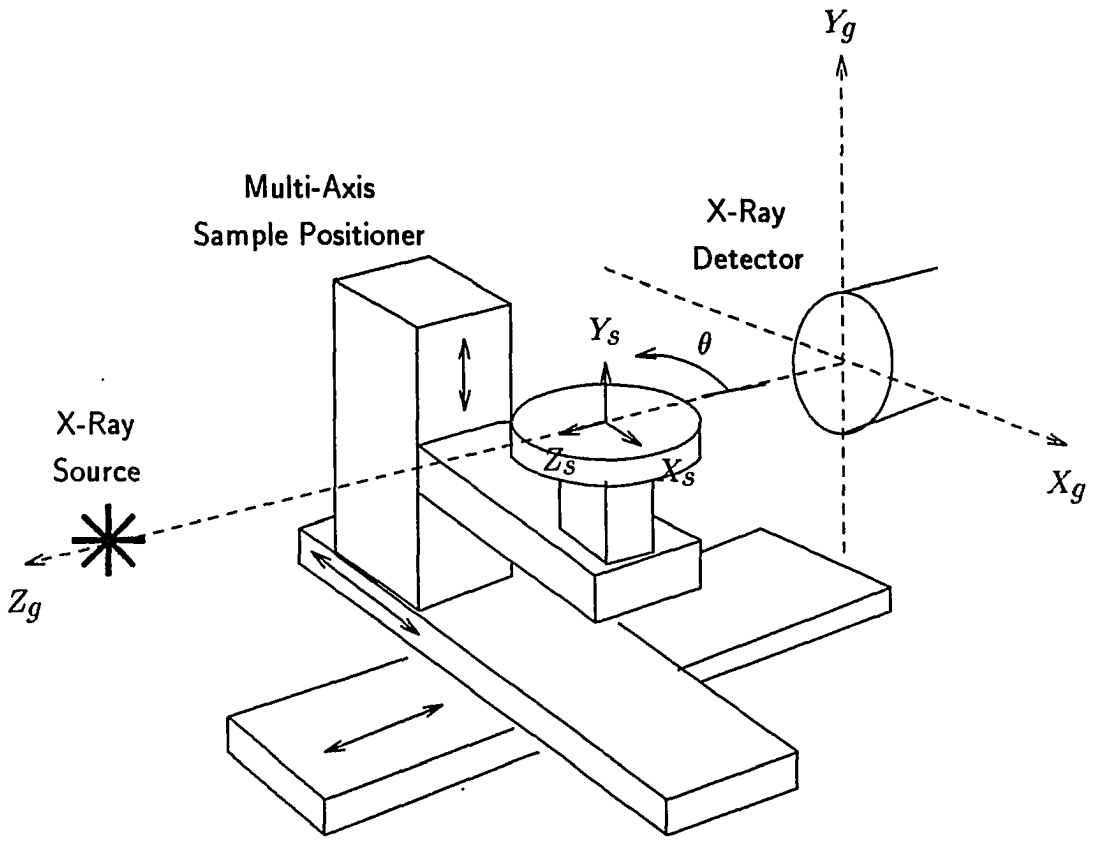

Figure 3.3: Global and sample coordinate systems for RTR laboratory

recorded as $\mathbf{c}_1 = \mathbf{c} + \Delta\mathbf{c}_1$ and θ_1. The linear transformation linking the range points is $\mathbf{p}_1 = \mathbf{R}(\mathbf{p}_0 - \mathbf{c}_0) + \mathbf{c}_1$. Conceptually, this transformation takes the range point $\mathbf{p}_0$ back to the initial center of rotation $\mathbf{c}_0$, applies the rotation matrix $\mathbf{R}$ (a function of the change in rotation $\theta_1 - \theta_0$), and translates it back to the new center of rotation $\mathbf{c}_1$. In terms of the general transformation defined by $(\mathbf{A}_1, \mathbf{b}_1)$:

$$\begin{aligned} \mathbf{A}_1 &= \mathbf{R}(\theta_1 - \theta_0) \\ &= \begin{bmatrix} \cos(\theta_1 - \theta_0) & 0 & \sin(\theta_1 - \theta_0) \\ 0 & 1 & 0 \\ -\sin(\theta_1 - \theta_0) & 0 & \cos(\theta_1 - \theta_0) \end{bmatrix}, \end{aligned} \tag{3.16}$$

and

$$\mathbf{b}_1 = (\mathbf{c} + \Delta\mathbf{c}_1) - \mathbf{A}_1(\mathbf{c} + \Delta\mathbf{c}_0). \tag{3.17}$$

The matrix $\mathbf{R}(\theta)$ applies a rotation about the Y_S axis. This process is repeated until $M \geq 2$ measurements are made. The quantities $\mathbf{s}$, $\mathbf{m}_i$, $\mathbf{A}_i$, and $\mathbf{b}_i$ are organized into the system of Equation (3.11), which is subsequently inverted to solve for the range point $\mathbf{p}_0$. The entire process is applied to an arbitrary number of range points within the sample.

Flaw measurements are made by selecting endpoints of crack features. Complex cracks are measured by selecting vertices within the crack image as range points. Once the 3-D coordinates are determined, the crack is reconstructed by connecting piecewise linear segments between the range points. The orientation of the crack is completely determined by the points $\mathbf{p}_{0i}$. The length of the crack is computed by summing the lengths as

$$L = \sum_{i=1}^{M-1} \left| \mathbf{p}_{0i} - \mathbf{p}_{0i-1} \right|. \tag{3.18}$$

This feature was implemented into the 3-D reconstruction program to allow the user to measure the length between an arbitrary sequence of points.

The centroid of void-like flaws and inclusions can be identified as well. The 3-D centroid projects closely to the 2-D centroid of the projection on the detector. For a sphere of uniform density, the distance between the centroid of the 2-D elliptical projection and the projection of the 3-D sphere centroid is (McNeil, 1966)

$$\Delta x = (d/2)[\tan(\theta - \phi) + \tan(\theta + \phi) - 2\tan\theta], \tag{3.19}$$

where d is the source-to-detector distance, θ is the angle between a source ray passing through the sphere centroid and a source ray normal to the detector, and 2ϕ is the angle subtended by the sphere boundary (see Figure 3.4). The distance Δx is zero when the sphere is on-axis with the source ($\theta = 0$). Δx increases slightly off-axis. McNeil used a 1/4" (0.64 cm) sphere with a source/detector distance $d = 36$" (91 cm) and $\theta = 14''02'$ ($\phi = 0°12'$ follows from the 1/4" sphere) to get Δx =0.00012" (0.00030 cm). Thus, the error is negligible, considering that the effective width of a pixel in the X-ray detector is 0.017 cm (at 60 pixels/cm sampling frequency). Limits on the void's boundaries are determined by making 2-D measurements from a series of sample rotations. More accurate modeling of the flaw shape is possible (Wallingford, 1990), although this requires the gray values of the projection to be used. The image intensifier has a wide variety of radiometric aberrations which would need to be taken into account to make this work successfully.

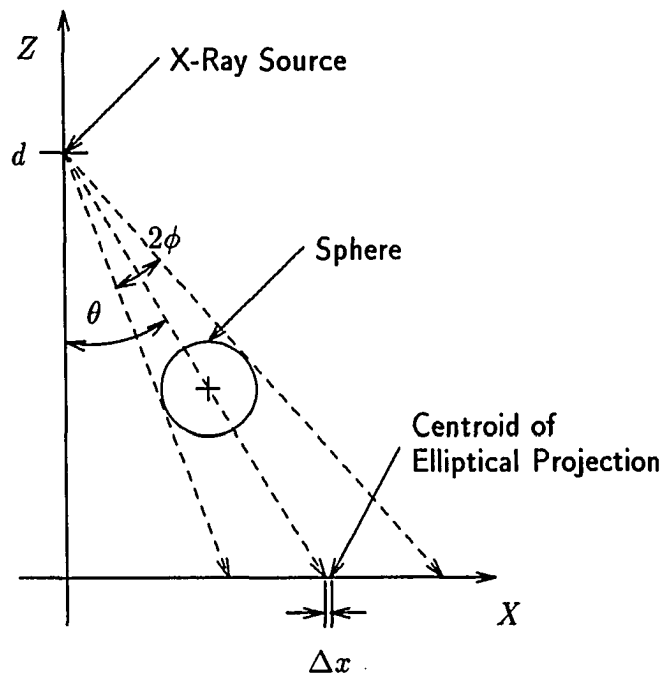

Figure 3.4: Error in determining 3-D centroid from 2-D projection

Simulation of 3-D Measurement System

A simulator was developed to make detailed analyses of the 3-D measurement system. The simulator is split into a forward model and an inverse model. The inverse model is the the same as that implemented in the real-time laboratory. It uses $\mathbf{s}$, $\mathbf{c}$, $\mathbf{m}_i$, and a list of sample manipulations to calculate $\mathbf{p}_0$. The forward model uses the same information, except $\mathbf{p}_0$ is input and the measurements $\mathbf{m}_i$ are output. These models are used as the basis of a Monte-Carlo simulation to study the effects of noise and bias on the inverse solution. Simulation was used since interaction of variables and lack of an analytic expression for the inversion process would otherwise make this analysis difficult.

Forward model equations

The same collinearity constraints are used for the forward model, except now the range point $\mathbf{p}_0$ is given and the measurement $\mathbf{m}_0$ needs to be determined. The collinearity of these points with the source is expressed as

$$\begin{aligned} \mathbf{C}_{\mathbf{s}-\mathbf{p}_0}(\mathbf{m}_0 - \mathbf{p}_0) &= \mathbf{0} \\ \mathbf{C}_{\mathbf{s}-\mathbf{p}_0}\mathbf{m}_0 &= \mathbf{C}_{\mathbf{s}-\mathbf{p}_0}\mathbf{p}_0 \\ \mathbf{C}_{\mathbf{s}-\mathbf{p}_0}\mathbf{m}_0 &= \mathbf{C}_{\mathbf{s}}\mathbf{p}_0. \end{aligned} \tag{3.20}$$

The transformations $(\mathbf{A}_i, \mathbf{b}_i)$ are computed using the same formulas as for the 3-D inversion (Equations (3.16) and (3.17)). These are applied to $\mathbf{p}_0$ to find the translates $\mathbf{p}_i$.

The Z component of $\mathbf{m}_i$ is constrained to the detector surface. A planar surface in the XY plane is selected, so $m_{i3} = 0$ for all measurements (a planar surface is

justified since the X-ray detector is calibrated to emulate a linear planar detector). This reduces the number of unknowns to 2, so Equation (3.20) can be solved uniquely. Expanding both sides of Equation (3.20) results in

$$\begin{bmatrix} -(s_3 - p_{03})m_{02} \\ (s_3 - p_{03})m_{01} \\ -(s_2 - p_{02})m_{01} + (s_1 - p_{01})m_{02} \end{bmatrix} = \begin{bmatrix} -s_3p_{02} + s_2p_{03} \\ s_3p_{01} - s_1p_{03} \\ -s_2p_{01} + s_1p_{02} \end{bmatrix}. \tag{3.21}$$

Adding the first two rows results in the following system:

$$\begin{bmatrix} (s_3 - p_{03}) & -(s_3 - p_{03}) \\ -(s_2 - p_{02}) & (s_1 - p_{01}) \end{bmatrix} \begin{bmatrix} m_{01} \\ m_{02} \end{bmatrix} = \begin{bmatrix} s_3(p_{01} - p_{02}) + (s_2 - s_1)p_{03} \\ s_1p_{02} - s_2p_{01} \end{bmatrix}. \tag{3.22}$$

This is a full rank system which can be solved for the measurement X and Y coordinates. This technique is applied to each $\mathbf{p}_i$ to calculate the remaining measurement points.

Simulation results

The simulator was implemented using the modules shown in Figure 3.5. The ellipses indicate user specified parameters to define the laboratory setup (X-ray source position and sample positioner location), the range point location, and the variances and biases to be used to perturb the positions of the X-ray source, sample center of rotation, and screen measurements. The rectangles indicate the major sections of the simulator itself. The screen measurements $\mathbf{m}_i$ are computed using the forward model described in the previous section. These measurements are considered to be "exact", since no noise or bias has been added yet. In the next step, more "realistic" measurements of the system are created. A normal random number generator is used

to create measurement noise; for each measurement quantity, the random number is scaled by a standard deviation and offset by a bias appropriate to that quantity. The X-ray source and sample position measurement noise is assumed to be continuous, while the screen measurements are quantized to emulate the behavior of the digitizer.

The perturbed values are applied to the same algorithm that is used to make the 3-D measurements in the laboratory. This routine generates an estimate of the range point, which is saved to an array. The simulator goes back and calculates a new set of noise values, which in turn are applied to the range point calculator to generate another estimate of the range point. This process is repeated many times (usually 100) to build up a distribution of estimates. The average and standard deviation of this distribution are computed, and bias is determined by comparing the average value of the estimate to the "true" value specified earlier by the user.

The error in estimating the Z component (depth) of the range point is of most interest, since the X and Y components are easily calculated from only a single 2-D projection image. Measurement errors stem from four sources:

1. Determining the 3-D position of the X-ray source,
2. Determining the 3-D center of rotation of the sample positioner platter,
3. Movement of the sample from one view to the next, and
4. Determining the measurement points from the display screen.

Error Source (3) is negligible in this system due to the high precision and accuracy of the sample positioner. The laboratory source/positioner/detector geometry remains fixed once the measurement is in progress, so Error Sources (1) and (2) contribute a

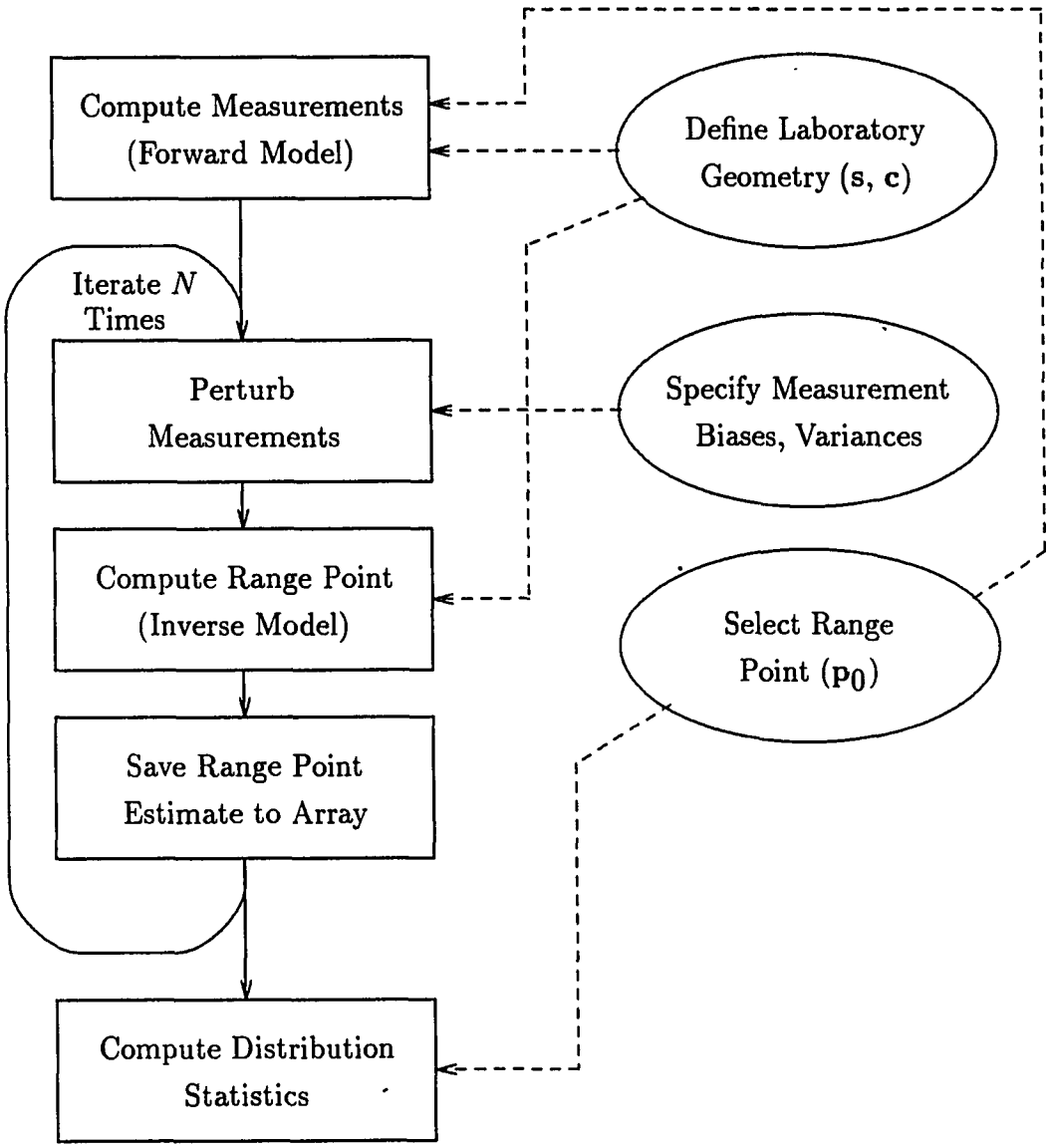

Figure 3.5: Flow diagram of 3-D measurement simulator

systematic error or bias to the measurement. Selection of measurement points from the display screen is the only variation encountered during repetition of the same experiment, so Error Source (4) contributes the random error to the depth measurement. Consequently, the simulation studies were used to determine the influence of the following factors on the systematic and random error components of the depth measurement:

- Sensitivity to random measurement errors as a function of:
    1. change in position between two views (translation)
    2. change in angle between two views (rotation)
    3. distance from center of rotation
    4. number of views between a fixed angle of rotation
    5. sample/detector distance (magnification)
- Sensitivity to bias errors in:
    1. source Z position
    2. sample positioner center of rotation Z position

Some results from Chapter 5 are used to make the simulations applicable to the laboratory measurements performed there. A precise method was developed to calculate the X and Y components of $\mathbf{s}$ and $\mathbf{c}$ once the Z component was known, so the Z component measurement dominates the error in determining these quantities . The Z position was determined using a tape measure, which was accurate to within $\pm 1/16$" (± 0.16 cm). The standard deviation associated with measuring feature points

Table 3.1: Simulation parameters for translation experiment, 4× magnification

Quantity	Nominal Value (cm)	Standard Deviation (cm)	Bias (cm)
$\mathbf{s}$	$[0\ 0\ 100]^T$	$[0\ 0\ 0]^T$	$[0\ 0\ 0]^T$
$\mathbf{c}$	$[0\ 0\ 60]^T$	$[0\ 0\ 0]^T$	$[0\ 0\ 0]^T$
$\mathbf{p}_0$	$[0\ 0\ 58]^T$	—	—
$\mathbf{m}_i$	—	$[0.012\ 0.012\ 0]^T$	$[0\ 0\ 0]^T$

from the display screen was found to be 0.5–0.8 pixels. The simulations use a standard deviation of 0.7 pixels for both X and Y measurements; this corresponds to 0.012 cm resulting from the 60 pixel/cm sampling frequency used to digitize the real-time image. A constant standard deviation for the measurement noise is justified since in practice image processing routines are used to enhance the features of interest, so the operator experiences the same level of uncertainty in selecting these features from one view to the next.

The nominal setup for the simulations places the X-ray source 100 cm from the detector. Magnifications of 4 times were most commonly used for the samples in Chapter 5; 1× and 20× magnifications are also investigated here.

Translation A two-view translation experiment was set up using the geometry indicated in Table 3.1. The table lists the quantity of interest, its nominal value, and the standard deviation and bias of the random noise added to the nominal value to make the perturbed measurement value. Here, the X-ray source was placed on the Z axis 100 cm from the detector, the positioner center was placed on the Z axis 60 cm from the detector (which results in 4× magnification), and the range point

was located on the Z axis 2 cm from the center of rotation. Measurement noise was added only to the display screen measurements. The initial view was always made with the range point positioned as shown in the table, and the second view was made after translating the range point in the $+X$ direction by an amount varying from 0 to 20 cm. Both the standard deviation of the range point depth measurement and the condition number of the inversion are plotted as functions of the change in position (Figure 3.6). Note that the sample had to be translated at least 15 cm to achieve a depth standard deviation below 0.02 cm. This much translation is impractical for a single-detector setup since the detector has limited field of view. In fact, the laboratory setup of Chapter 5 only permitted a translation of 1.5 cm at 4× magnification, so the simulation predicts at least an order of magnitude higher error for a practical geometry. A second detector would be required to image the translated sample, which obviously complicates the laboratory setup.

Translation-only measurements result in an ill-conditioned $\mathbf{X}$ matrix for two reasons. First, the long source-to-detector distance dominates the difference $\mathbf{s} - \mathbf{m}_i$ since $\| \mathbf{s} \|$ is usually 100 cm, and $\| \mathbf{m}_i \|$ is about 4 cm due to the limited detector field of view. Second, the range point transformation matrix $\mathbf{A}_i$ is identity, so the additional rows added to $\mathbf{X}$ are nearly the same as the first three rows found by the initial measurement. For example, a 2 cm sample translation with the geometry of

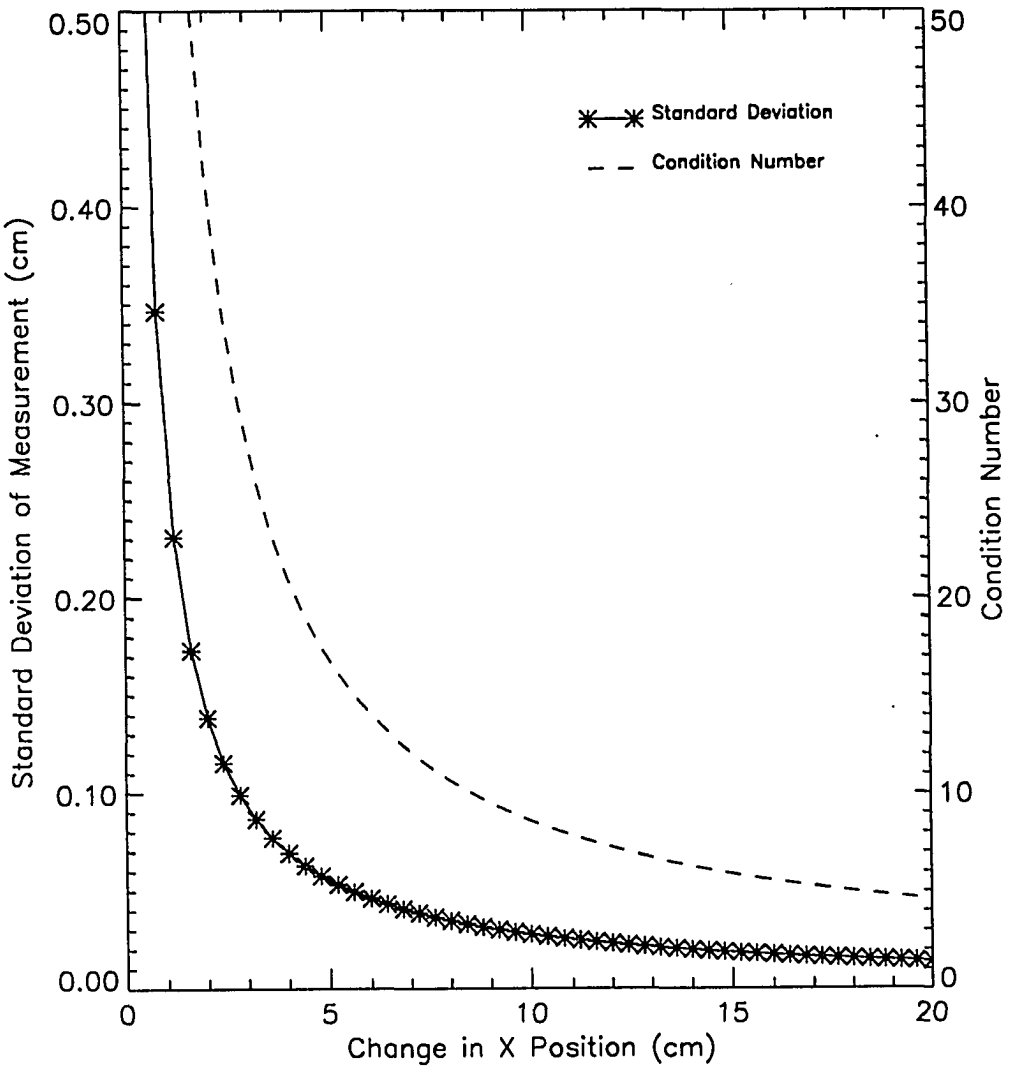

Figure 3.6: Error sensitivity as a function of translation amount

Table 3.1 results in the following $\mathbf{X}$ matrix:

$$\mathbf{X} = \begin{bmatrix} 0 & -100 & 0 \\ 100 & 0 & 0 \\ 0 & 0 & 0 \\ 0 & -100 & 0 \\ 100 & 0 & 4.76 \\ 0 & -4.76 & 0 \end{bmatrix}.$$

The first three rows result from the initial view, and the last three rows are obtained after translating to the second view. Rows 3, 4, and 6 are all linearly dependent on Row 1, and Row 5 is only marginally independent from Row 2. Consequently, the X_{53} value is the only value keeping $\rho(\mathbf{X}) = 3$; X_{53} has to be made fairly large to make $\mathbf{X}$ better conditioned. As will be seen, using a rotation matrix for $\mathbf{A}_i$ changes all the values in the last three rows of $\mathbf{X}$ to make them linearly independent from the first three rows, making $\mathbf{X}$ well-conditioned for inversion while keeping the simple geometry of a single fixed detector.

Rotation The ability to rotate the sample is one of the primary advantages of this system over a translation-only system. A two-view rotation experiment was set up using the same geometry as the translation experiment (Table 3.1). As before, the geometry shown in the table was used for the initial view. The second view was made by rotating the range point in the $+\theta$ direction in the range 0–360°. The depth standard deviation and condition number are plotted as a function of change in angle in Figure 3.7.

Here, a 20° rotation was sufficient to get an error below 0.02 cm (this required

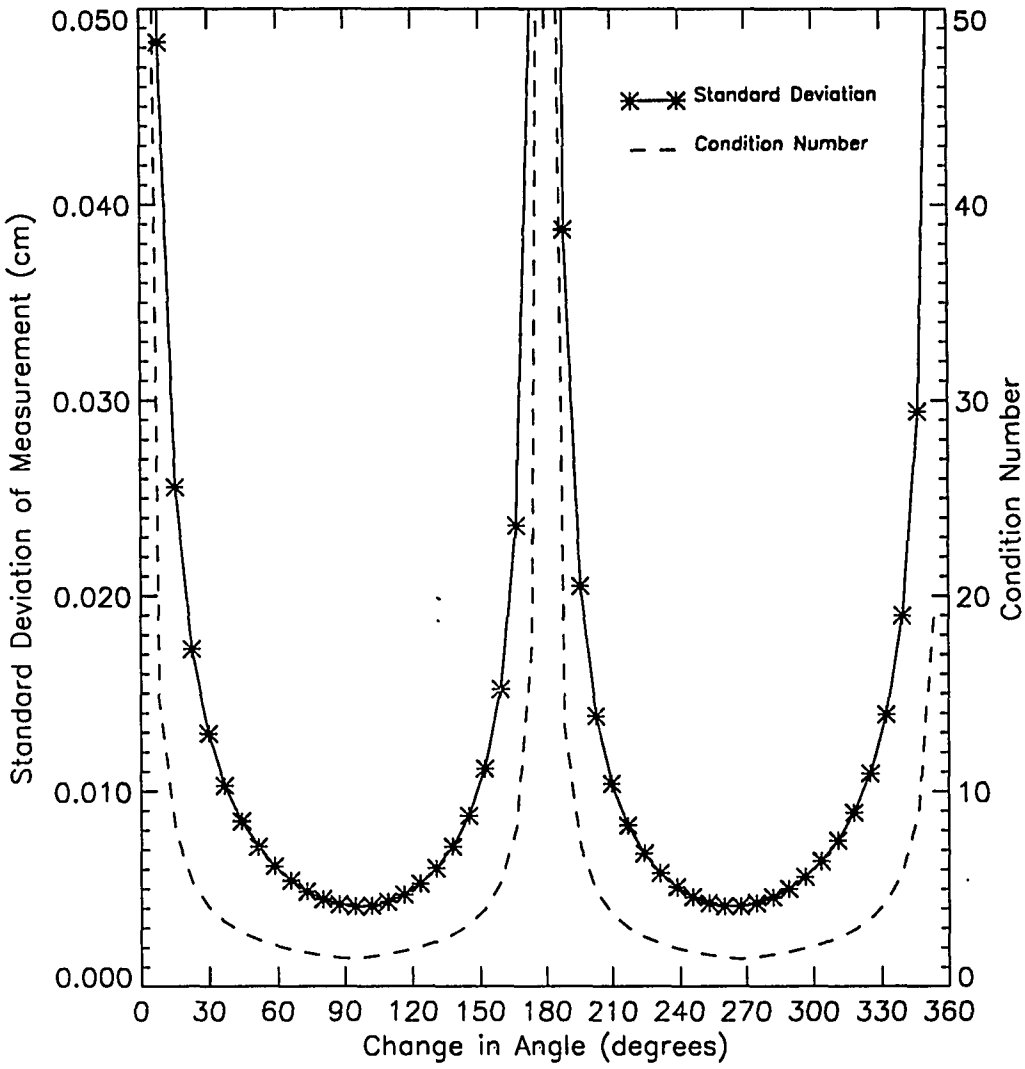

Figure 3.7: Error sensitivity as a function of rotation amount

a 15 cm translation for the previous experiment), and errors less than 0.01 cm were typical over the majority of rotation angles. The measurement was ill-conditioned using small angular changes, but was also ill-conditioned at 180° rotation. Using small angular changes does not substantially change the last three rows of **X**, so the ill-conditioned nature of this situation is evident. However, a rotation of 180° results in the following matrix:

$$\mathbf{X} = \begin{bmatrix} 0 & -100 & 0 \\ 100 & 0 & 0 \\ 0 & 0 & 0 \\ 0 & -100 & 0 \\ -100 & 0 & 0 \\ 0 & 0 & 0 \end{bmatrix}.$$

Here the rank of **X** is 2, so the inversion cannot converge to a unique solution. This problem is due to the symmetry of placing **s**, **c**, and $\mathbf{p}_0$ all on the Z axis. By moving the X-ray source off the Z axis to $\mathbf{s} = [20\ 30\ 100]^T$, the **X** matrix becomes:

$$\mathbf{X} = \begin{bmatrix} 0 & -100 & 71.4 \\ 100 & 0 & -47.6 \\ -71.4 & 47.6 & 0 \\ 0 & -100 & -78.9 \\ -100 & 0 & 52.6 \\ 78.9 & 52.6 & 0 \end{bmatrix}.$$

This matrix has $CN = 1.8$, indicating it is well-conditioned. The effect of using the off-axis X-ray source as a function of change in rotation angle is plotted in Figure 3.8.

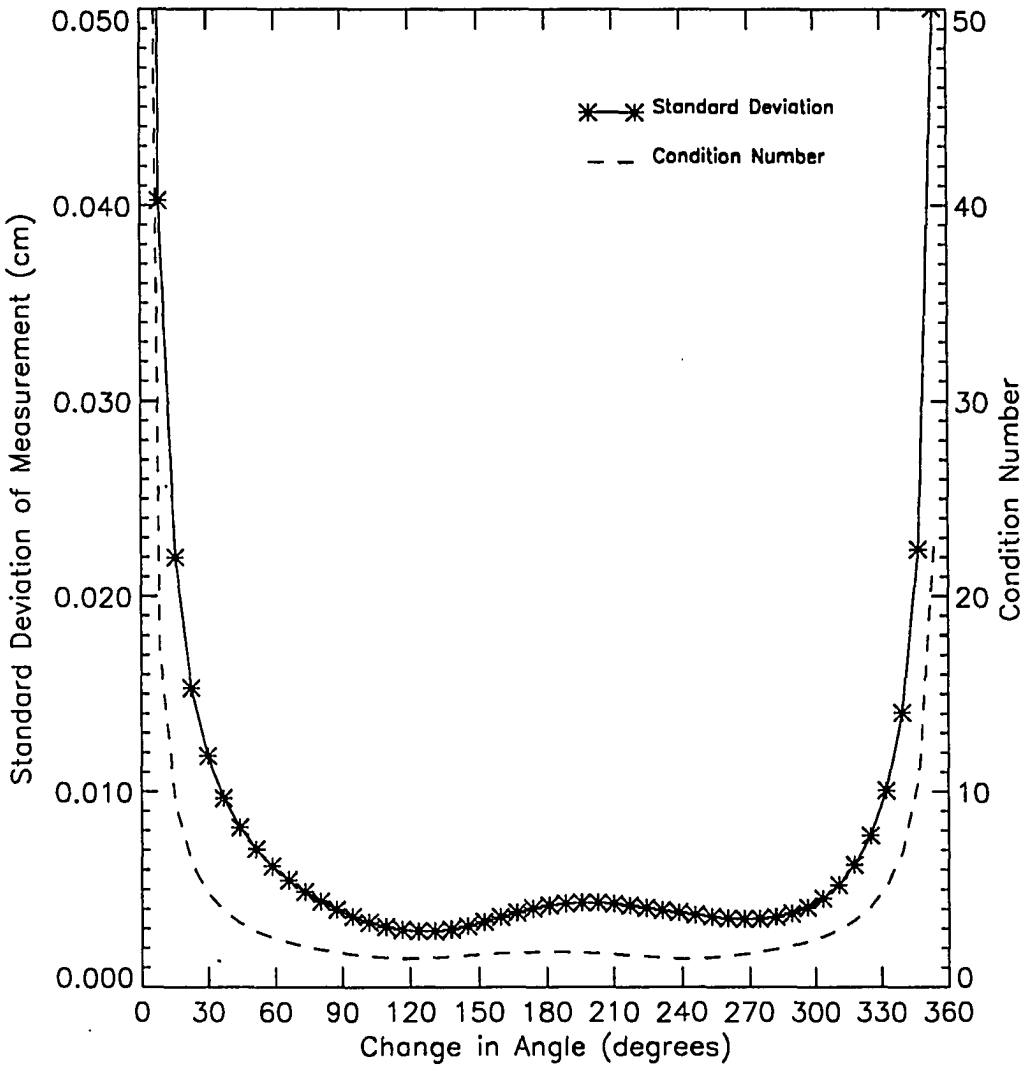

Figure 3.8: Measured depth standard deviation due to change in angle (X-ray source off the Z axis)

In comparison to translation, rotation was found to be superior to achieve a given level of depth error. As a result, rotation-only measurements are emphasized in this work since they are more efficient.

Distance from center of rotation The same geometry as the rotation experiment (Table 3.1) was used here. The initial Z position of $\mathbf{p}_0$ was varied from 58 cm to 62 cm (i.e., ± 2 cm on either side of $\mathbf{c}$). The depth standard deviation in determining the range point position was 0.013 cm at $\mathbf{p}_{03} = 58$ cm and 0.011 cm at $\mathbf{p}_{03} = 62$ cm. The error decreased monotonically between these two extremes, rather than reaching a minimum at zero distance from the center. Overall, the change was minimal; the trend of decreasing error as the point was moved closer to the source suggests the change was due to increased magnification. Using a $1\times$ configuration ($\mathbf{s} = [0\ 0\ 100]^T$, $\mathbf{c} = [0\ 0\ 5]^T$) with $\mathbf{p}_{03}$ varying from 3 cm to 7 cm resulted in depth standard deviations of 0.029 cm and 0.027 cm, respectively. Again, the change was minimal, and the error was less at the higher magnification condition of $\mathbf{p}_{03} = 7$ cm. Thus, the variance in depth estimation was not found to be a function of distance from the center of rotation.

Number of views between fixed angle of rotation So far, only two-view experiments have been considered. The system in Equation (3.11) can support M measurements, so this case was examined for a rotation experiment. The total rotation angle $\Delta\theta_T$ was kept fixed, and multiple views were made by dividing this angle into equal sub-angles. The objective was to determine whether using the intermediate views could improve upon a two-view rotation experiment. Both a well-conditioned two-view experiment ($\Delta\theta_T = 30^\circ$) and an ill-conditioned experiment ($\Delta\theta_T = 5^\circ$)

Table 3.2: Simulation results for multi-view rotation, with 30° total rotation

Number of Views	Depth Standard Deviation (cm)	CN
2	0.013	4.04
3	0.015	4.95
4	0.012	5.42
5	0.012	5.71
6	0.011	5.90

Table 3.3: Simulation results for multi-view rotation, with 5° total rotation

Number of Views	Depth Standard Deviation (cm)	CN
2	0.079	24.07
3	0.091	29.48
4	0.071	32.23
5	0.074	34.07
6	0.067	35.23

were considered. The 4× geometry of Table 3.1 was used for both tests. Table 3.2 lists the depth standard deviations and condition numbers as the number of views was increased from 2 to 6. The decrease in error from two views to six views was 0.003 cm, which is not a substantial improvement considering the amount of extra work required to obtain the additional data. Furthermore, the decrease was not monotonic since the error went up slightly from two views to three views.

The results for the ill-conditioned experiment are indicated in Table 3.3. Here, the overall decrease was only 0.012 cm, which represents a 15% reduction in error over the initial error of 0.079 cm.

Table 3.4: Simulation parameters for rotation experiment, 1× magnification

Quantity	Nominal Value (cm)	Standard Deviation (cm)	Bias (cm)
s	$[0\ 0\ 100]^T$	$[0\ 0\ 0]^T$	$[0\ 0\ 0]^T$
c	$[0\ 0\ 3]^T$	$[0\ 0\ 0]^T$	$[0\ 0\ 0]^T$
p_0	$[0\ 0\ 1]^T$	—	—
m_i	—	$[0.012\ 0.012\ 0]^T$	$[0\ 0\ 0]^T$

In both cases, it is evident that accumulating intermediate views can somewhat reduce the errors associated with measuring depth, but this marginal improvement needs to be weighed against the cost of collecting the extra data. In situations where angular rotations are limited to small angles, collecting intermediate views does not substantially improve the estimate. Thus, two-view experiments with a rotation of at least 20° are sufficient to achieve good results.

Magnification The effect of magnification on a two-view rotation experiment was considered for the cases of 1× and 20×. Magnification effectively increases resolution and reduces display screen measurement noise since the larger object is easier to see. This improvement is paid for by reduced field of view, so less material can be inspected. Tables 3.4 and 3.5 list the laboratory geometries for the 1× and 20× configurations, respectively.

Figure 3.9 shows the depth measurement standard deviation as a function of change in angle between the two views for the 1× experiment. Here, the minimum error was 0.01 cm, which required a rotation of 90°. This much rotation is acceptable

Table 3.5: Simulation parameters for rotation experiment, 20× magnification

Quantity	Nominal Value (cm)	Standard Deviation (cm)	Bias (cm)
$\mathbf{s}$	$[0\ 0\ 100]^T$	$[0\ 0\ 0]^T$	$[0\ 0\ 0]^T$
$\mathbf{c}$	$[0\ 0\ 95]^T$	$[0\ 0\ 0]^T$	$[0\ 0\ 0]^T$
$\mathbf{p}_0$	$[0\ 0\ 93]^T$	—	—
$\mathbf{m}_i$	—	$[0.012\ 0.012\ 0]^T$	$[0\ 0\ 0]^T$

for objects with axial symmetry, but is not acceptable for plate-like geometries. Using a more typical rotation of 20–30° resulted in a factor of 4 to 5 increase in error.

Figure 3.10 shows the results for the 20× experiment. The standard deviation of the depth measurement dropped to less than 0.001 cm at large rotation angles, and was less than 0.01 cm over the typical range of 5–30°. Again, this much magnification places limits on the sample size, but it is clear that using as high a magnification as possible is beneficial towards reducing measurement errors. The microfocus X-ray source makes magnification practical; however, a standard broad-focus source can also be used to achieve good results with a 1× configuration as long as the sample can be rotated a greater amount.

The previous simulations demonstrated the sensitivity to random errors in selecting the feature points for a variety of configurations. The next experiments investigate errors due to mis-measuring the Z positions of the X-ray source and positioner center of rotation with respect to the detector. Here, random noise is zero on all parameters, and bias is applied to selected quantities.

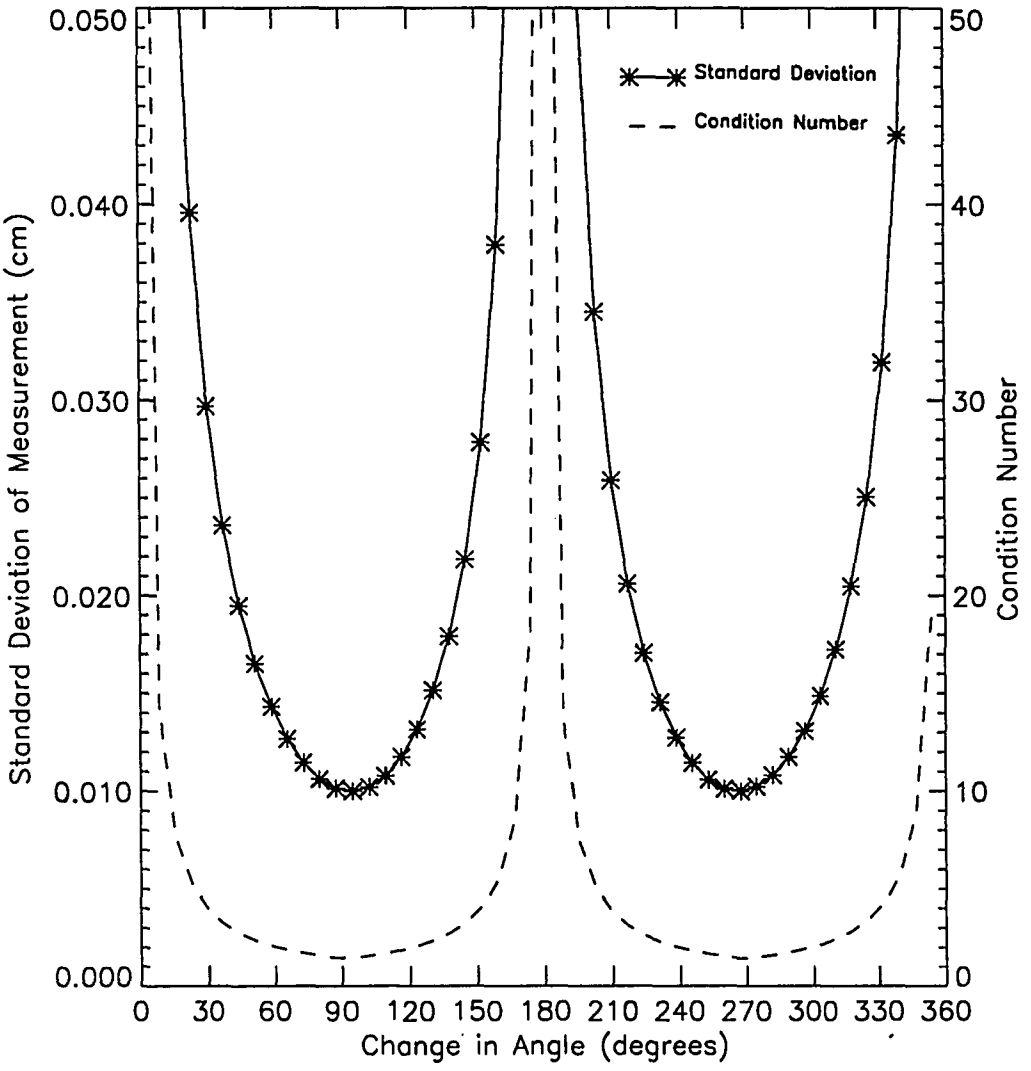

Figure 3.9: Two-view rotation experiment, 1× magnification

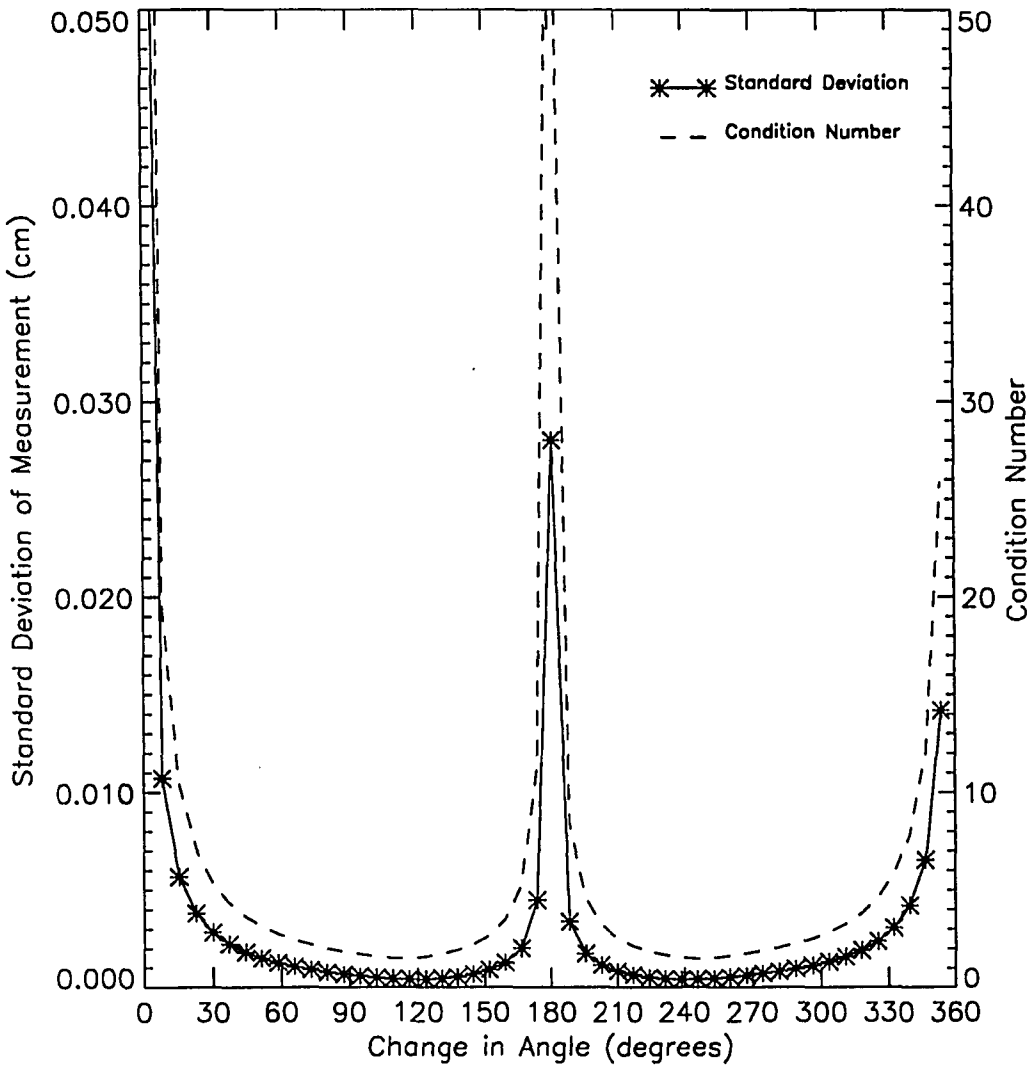

Figure 3.10: Two-view rotation experiment, 20× magnification

Source position bias The two-view rotation experiment was used as before, except the feature point measurement noise was set to zero. The forward model generated measurement data based on the nominal laboratory setup. The effect of mis-measuring the Z position of the X-ray source was simulated by adding a bias to s_3 and computing the range point estimate using the "incorrect" value. 100 runs were used to develop a distribution of estimates, and the bias was calculated by subtracting the true range point value from the average estimated value. Since changing the sign of the X-ray source Z bias simply changed the sign of the range point bias, only the results of a positive source bias values will be presented here.

The bias in the range point estimate was found to be a weak function of the rotation angle between the two views. For the 4× configuration, the bias was −0.029 cm at 0°, and −0.031 cm at 180°. In between these points, the bias followed a sinusoidal variation with a single period over the range 0–360°. Table 3.6 lists the results obtained using multiple magnifications and source bias values. From this table, it is evident that depth bias is slightly affected by the rotation angle for the two-view experiment, but this effect is down an order of magnitude compared to the effect of error in determining the Z position of the source. The magnitude of the bias is negligible for 1× magnification, and increases steadily as magnification increases. For the 4× configuration, the magnitude of the bias is limited to 0.01–0.02 cm for an error of 0.5 cm. This provides an upper limit on the bias error, since the tape measure accuracy lies between 0.1–0.2 cm.

Center of rotation position bias A similar experiment was performed to determine sensitivity to bias error in determining the positioner center of rotation Z

Table 3.6: Sensitivity to bias in X-ray source Z position measurement

Source Z Bias (cm)	Minimum Bias (cm)	Maximum Bias (cm)
1× Magnification		
0.1	+0.000	+0.000
0.5	+0.000	−0.001
1.0	+0.000	−0.001
2.0	+0.000	−0.002
4× Magnification		
0.1	−0.003	−0.003
0.5	−0.014	−0.015
1.0	−0.029	−0.031
2.0	−0.057	−0.061
20× Magnification		
0.1	−0.037	−0.039
0.5	−0.185	−0.193
1.0	−0.367	−0.386
2.0	−0.724	−0.767

Table 3.7: Sensitivity to bias in sample center of rotation Z position measurement

Source Z Bias (cm)	Minimum Bias (cm)	Maximum Bias (cm)
1× Magnification		
0.1	0.10	0.10
0.5	0.51	0.51
1.0	1.02	1.02
2.0	2.04	2.04
4× Magnification		
0.1	0.10	0.11
0.5	0.52	0.53
1.0	1.05	1.05
2.0	2.10	2.10
20× Magnification		
0.1	0.14	0.14
0.5	0.70	0.70
1.0	1.40	1.40
2.0	2.80	2.80

position; Table 3.7 tabulates the results. In this case, a positive bias in c_3 resulted in a 1:1 effect plus some residual positive bias. For example, at 4× magnification, a 0.5 cm measurement error resulted in 0.52 cm error in the range point estimate; the 1:1 effect is 0.5 cm, and the residual bias is 0.02 cm. Consequently, even small errors in determining the center of rotation are reflected directly in the result. This is a significant problem when absolute measurements are to be made in the global coordinate system. However, most measurements are made relative to the boundaries of the sample, so measurements in the local coordinate system are only subject to the residual bias effects of 0.01–0.03 cm for bias errors of 0.1–0.5 cm.

CHAPTER 4. DETECTOR CHARACTERIZATION AND MODELING

The X-ray-to-light (X/L) converter is the heart of the real-time X-ray imaging system. The optical output of this converter is digitized, computer processed, and displayed for the operator. The X/L converter is the only difference between a real-time system and a system based on digitized X-ray film. This ability to continuously convert the X-ray field is the chief advantage of the X/L over film. The dynamic image conveys more information to the operator in less time. The disadvantages of the X/L are reduced contrast sensitivity, reduced resolution, increased spatial distortion, and increased radiometric distortion. These disadvantages are traded off against each other to make a variety of X/L designs. For this research, the X/L is used to make precise measurements of the projections of points of interest within a material sample, so the spatial characteristics of the X/L are of most importance.

A variety of X/L designs are available. The main design issues are sensitivity to photons in the X-ray regime ($\geq$ 10 KeV), amplification to achieve enough illumination for an optical video camera, maximization of spatial linearity, and maximization of resolution. The image intensifier tube is the most commonly used X/L in medical and industrial applications. It operates by converting the electrically neutral X-ray photons to electrons which are accelerated and focused by an electromagnetic lens

onto a small phosphor screen to make an optical image. This design has relatively high resolution and high sensitivity, or conversion efficiency. Compared to film, it also has high geometric distortion and limited resolution. This type of X/L is used in the RTR laboratory used for this work. This chapter is devoted to characterizing the image intensifier performance and developing algorithms to overcome its design limitations. The designs of other X-ray detectors will be briefly reviewed for comparison. These include microchannel plate, solid-state X-ray detector, and digital storage phosphor.

A microchannel plate (Chalmeton, 1980) is an array of microscopic electron multiplier tubes. The plate is used instead of the electromagnetic lens of the image intensifier. Each multiplier tube diameter is typically 10 to 100 μm. The interior of the tube is covered with a layer which emits secondary electrons upon impact by a primary electron. A voltage of about 1 KV is applied to set up a longitudinal electric field within the tube. A single input electron enters the tube and is accelerated. The input electron path is at a slight angle with respect to the tube axis, so eventually it strikes the wall of the tube and generates two or three secondary electrons. These electrons are subsequently accelerated and strike the tube wall. Each of these electrons releases more electrons, and this geometric progression results in a total electron gain of 10^4 to 10^5 output electrons. The microchannel plate has low geometric distortion. The cost of large-area plates is the main disadvantage. Plate diameters of up to 25 mm are manufactured in quantity for night vision applications, although large-area plates for RTR applications are becoming available (Gupta and Krohn, 1987).

Some designs couple the photodetector array directly to the scintillation material. Zhu, Babot, and Peix (1990) compared the performance of a 1-D 1024 array

of photodiodes coupled with a scintillator to an image intensifier and found 50% improvement in resolution, 20 dB increase in signal-to-noise ratio, and 20% improvement in sensitivity. The 1-D array must be scanned to create a 2-D image. Since this process takes about 4 seconds, the improved performance comes at the cost of frame speed. The 1-D linear array can also image a continuous process as in the production of steel (Jacquemod, Odet, and Goutte, 1990) where it is not necessary to wait for a 2-D image to be created.

The photodiode is also used to directly detect low energy ($<$ 10 KeV) X-rays. Samuelson and Jaggi (1989) used a commercially available 256×256 photodiode array in an X-ray microscopy application. They found that using a large pixel pitch of 40 μm was required to minimize cross-talk between the pixels. Photodiodes also provide integration capability of up to 1 hour when cooled to minimize thermal electron noise. This design is free of geometric distortion.

The digital storage phosphor system (Hillen, Schiebel, and Zaengel, 1987) uses a photostimulable phosphor as the X-ray detector. The X-ray photon energy is temporarily stored within the crystal lattice since thermal energy is insufficient to cause the luminescent center to release the excess energy. A small diameter laser beam is scanned over the phosphor plate. The laser adds enough energy to cause the material to release the stored energy as optical photons. The local variation in emission intensity is proportional to the absorbed X-ray energy. The optical photons pass through a light guide and are converted to an electron current by a photomultiplier tube. This current is amplified and digitized to make the final image. The phosphor screen has blurring due to optical scattering just as in an image intensifier, so resolution of the storage phosphor system is the same ($\leq$ 4 lp/mm). However, this system has higher

dynamic range since the laser readout system can be adjusted to match the X-ray exposure level. The storage phosphor has inherent integration capability like X-ray film, and has minimal geometric distortion.

Principle of Operation

The image intensifier is used as the real-time X-ray detector for this laboratory. After describing its operation, important aspects of the design that lead to aberrations in the final digitized image will be discussed. Those aberrations affecting the spatial performance of the tube will be modelled and corrected in the next main section.

Figure 4.1 shows a diagram of the main components of an image intensifier. This device converts an incident X-ray flux to an optical image which is recorded by a video camera. The input scintillator screen is made of a phosphorescent material which converts the high energy X-ray photons to lower energy optical photons. Since the brightness of this optical image is very weak (typically only 1% of the incident X-ray photons are converted), intensification is used to increase the brightness. Photons are electrically neutral and cannot be amplified or manipulated using electromagnetic fields. The intensification process begins at the photocathode which converts the low energy photons to electrons using the photoelectric effect. These electrons are accelerated at 20–30 KeV towards an output conversion phosphor that is 10 times smaller in diameter than the input conversion screen. Thus the image is intensified by electron acceleration and image minification. The following sections describe this complete process in more detail.

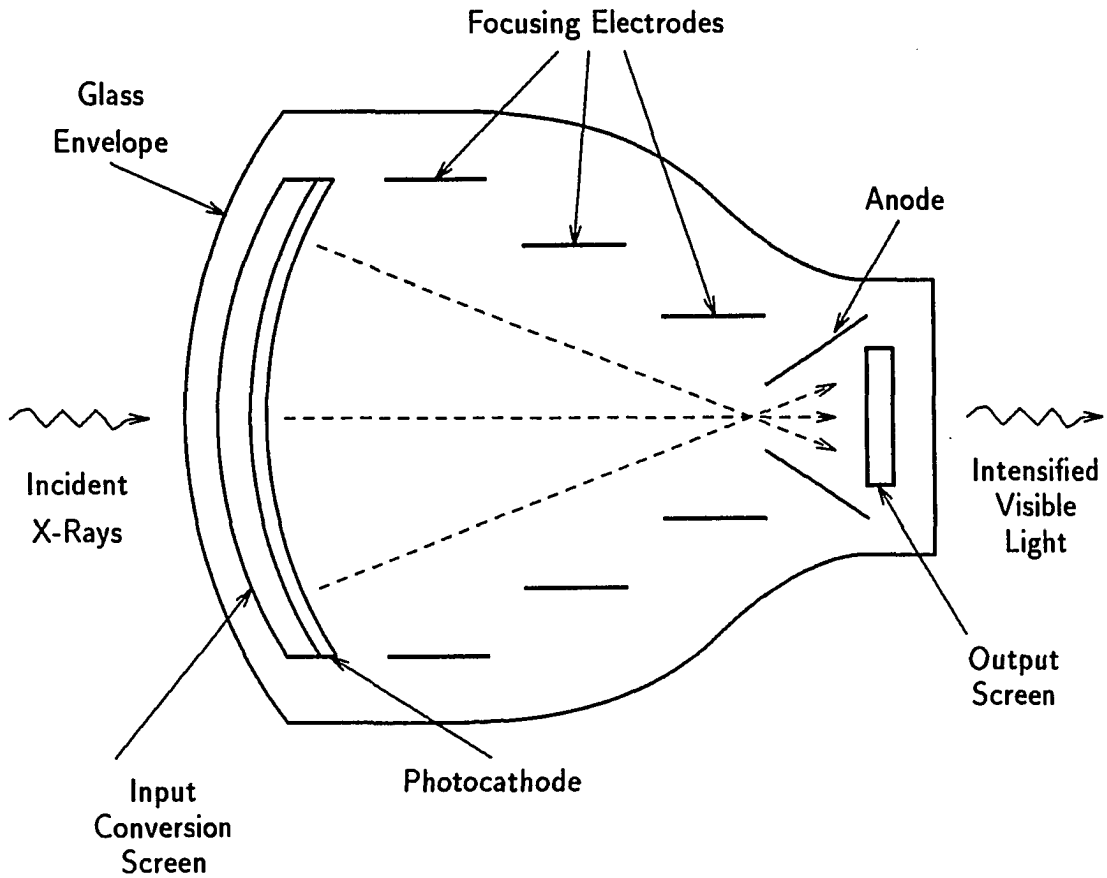

Figure 4.1: Schematic diagram of image intensifier

Input conversion screen

The input conversion screen consists of a thin layer of phosphor material. Early generation tubes used zinc sulfide (ZnS) or cadmium sulfide (CdS) as the phosphor material. Since the early 1980's, cesium iodide doped with a sodium impurity (CsI(Na)) has been the material of choice. It is more sensitive to X-rays and its material characteristics permit deposition of thinner screens which results in higher resolution (Bates, 1980). Resolution is inversely proportional to screen thickness. In a thicker screen, the optical photons have a greater scattering volume. This scattering is known as phosphor bloom. Sensitivity, on the other hand, is directly proportional to screen thickness. Here, each X-ray photon has a greater chance of interacting with the greater volume of phosphor material resulting in greater conversion efficiency. Thus, there is a fundamental trade-off between sensitivity and resolution. Special techniques have been used to reduce phosphor bloom by growing the CsI crystals as thin needle-shaped elements (Link *et al.*, 1989). This way the crystals act like optic fibers and cross-talk between the crystals is reduced.

The conversion screen is curved in a spherical shape to make an equal path length between all parts of the input screen and the output conversion phosphor screen to minimize distortion within the electromagnetic lens (Csorba, 1985). However, this curvature results in a distortion when the flat object plane is mapped onto the curved screen. The image magnification increases off-axis, resulting in "pincushion" distortion. This has the effect of making parallel lines in the object plane bow to the center of the image in the detected image plane. Furthermore, pincushion distortion is dependent on the position of the X-ray source, resulting in view-dependent distortion (Chackraborty, 1987). Any measurement procedure which uses multiple sources or

translation of a single source must take this factor into account. Pincushion distortion is the dominant spatial distortion encountered when using an image intensifier tube.

The increasing magnification off-axis also contributes to vignetting. This is a radiometric distortion where the image of a uniform intensity source has decreased gray levels at the periphery of the image. This effect was found to be about a 30% reduction for the image intensifier used here. Older generation tubes had as high as 50% reduction (Casperson, Spiegler, and Grollman, 1976).

The radial divergence of the X-ray source can be considered a part of the vignetting effect, but, as will be shown, this contribution is negligible. By treating the X-ray source as a Lambertian radiator, the off-axial intensity I relative to the on-axis intensity I_0 is proportional to $\cos\theta$, the angle between the source ray perpendicular to the detector and a ray intersecting the detector at some other location (Csorba, 1985). For a typical source/detector distance of $r = 100$ cm and a maximum distance of 8 cm from the center of the image intensifier screen (the radius of a 6" image intensifier), $\theta = \tan^{-1}(8/100) \simeq 4.57^{\circ}$, and $\cos\theta \simeq 0.997$. Thus, the X-ray intensity only falls off 0.3% at the edge of the image intensifier input screen, so the X-ray source can be considered to be a uniform field to within less than a percent.

The scintillator is mechanically coupled to a photocathode. This material uses the photoelectric effect to convert the output photons of the scintillator to electrons. Photocathode materials sense optical radiation with wavelengths in the range 1200–120 nm, or approximately 0.01–0.1 KeV (Csorba, 1985), so the input scintillator is required to "downconvert" the energy of the X-ray photons (10–200 KeV) to this regime. The electron field is proportional to the input X-ray field, and is input to the electromagnetic lens for amplification.

Electromagnetic lens

The electrons released by the photocathode are accelerated at 30 KeV towards the output conversion screen. This acceleration is the first method by which the X-ray image is intensified. The output conversion screen is also 10 times smaller in diameter than the input conversion screen. The electromagnetic lens focuses all photocathode electrons onto the output screen. Image minification is the second method of intensification. The overall increase in brightness is on the order of 10^4 (Christensen, Curry, and Nunnally, 1972).

The focusing quality of the electromagnetic lens steadily degrades away from the central axis (Csorba, 1985). Curving the input conversion screen alleviates this problem to a certain extent, but image sharpness is still maximum in the center of the image. For this reason, the electron lens of multi-field image intensifiers is externally adjustable to map reduced portions of the input screen onto the output screen. For example, a 9" tri-field image intensifier has 4.5", 6", and 9" operation modes. This permits the operator to conveniently change the field of view. The smaller fields use a restricted area in the center of the tube where electron focusing is better and geometric distortion is reduced. This reduced field of view means less material of the sample can be inspected at once.

Spiral distortion is another aberration introduced by the electromagnetic lens. Inhomogeneities in the lens field as well as external magnetic fields cause straight lines in the object plane to be mapped into S-shaped curves.

Output conversion screen

The output phosphor is a circular screen from 15 to 20 mm in diameter. The output phosphor is the primary limit on overall resolution. Due to the ten-fold reduction in image size, the phosphor crystals must be small and closely packed to minimize granularity. However, for a monolayer structure, the screen thickness determines the resolution (Csorba, 1985). The final output of the image intensifier output conversion screen is on the order of 5×10^6 photons per second per square millimeter (Link *et al.*, 1989).

Veiling glare is a radiometric degradation that shows up on the output conversion screen (Seibert, Nalcioglu, and Roeck, 1984). Electron and photon scatter within the image intensifier tube contribute to a large-scale blurring effect. This is most pronounced when the object has adjacent regions of low and high X-ray transmission, for example a step transition in thickness. This aberration affects the low-frequency response of the tube and distorts the gray level response of the digitized image.

Reduction of Spatial Distortion

The distortions inherent in the image intensifier must be characterized to linearize the detector and improve its resolution. The spatial aberrations are of most concern for this work. An image warping method was used to reduce geometric distortion. This procedure images a known object, say a grid of uniformly spaced holes in a plate, and fits a model to describe how the uniformly space features were distorted by the image intensifier to make the measured image. Once the distortion mechanism is known, the model is inverted to map the measured (distorted) values onto a linearized (undistorted) image. The mapping is either applied to every pixel

in the distorted image, or only to specific features of interest. Mapping only the isolated features is more computationally efficient, and is the technique used for this work.

Two main modelling techniques are reported in the literature. The first takes account of the spherical geometry of the screen and models how the image magnification increases away from the image center. The second technique uses a two dimensional third order polynomial.

Casperson, Spiegler, and Grollman (1976) use a single parameter model to account for pincushion distortion:

$$\begin{aligned} x' &= x + Dx(x^2 + y^2), \\ y' &= y + Dy(x^2 + y^2), \end{aligned} \tag{4.1}$$

where x and y are the coordinates in the input object plane, x' and y' are the (distorted) coordinates in the output image plane, and D is the distortion parameter. This model is only valid for the pincushion distortion aberration (i.e., it does not account for coma, spherical aberration, or higher order effects).

Chakraborty (1987) proposes a more advanced model to account for different positions of the X-ray source. This model was developed for a tomosynthesis application which uses multiple X-ray sources at different angulations with respect to the detector. The object plane is not in intimate contact with the phosphor conversion screen (due to its curvature), so the pincushion distortion is dependent on the position of the X-ray source. This is termed view-dependent distortion. This additional generality is not required when a fixed source/detector arrangement is used.

Haaker *et al.* (1988) make use of a two-dimensional third order polynomial to implement a high speed correction during tomosynthesis data acquisition. A dedicated

Motorola 68020 microprocessor was able to apply this polynomial to a $512 \times 512 \times 8$ image in 100 ms. The polynomial coefficients were computed off-line as part of calibration procedure. This procedure was implemented here and was found to correct the the pincushion distortion of the image intensifier to a maximum error of 0.5 pixels, or 0.008 cm at 60 pixels/cm sampling frequency.

Once the image intensifier and X-ray source are setup in the desired position, a reference object containing a uniform grid of holes of known spacing is imaged by the system. The image of this object is analyzed to determine how the imaging process distorted the relative positions of the imaged hole pattern. The objective of the measurement is to precisely determine the coordinates of the imaged holes. This data is used to determine a mapping function which describes how the uniformly spaced holes in the object plane were moved to their distorted positions in the image data. The hole coordinates are determined by thresholding the image to make the background zero (black) and the hole features one (white). The centroid of each cluster of white pixels is used as the location of the imaged hole.

Distortion measurement

A 10.5" by 10.5" piece of wire-wrap circuit board was used as the reference object. The board consists of a square array of 0.042±0.005" diameter holes on 0.1±0.005" centers. The board was affixed to the image intensifier input screen, and was aligned with a level to ensure that the holes were lined up properly with the XY plane of the global coordinate system. The video camera mount was rotated until the image of the hole pattern was lined up with the scan lines of the digitizer, and a gray level image was acquired. Figure 4.2 shows a slice along the center row of

this image. Note that radiometric distortion accounts for a significant change in the background gray level as a function of pixel location, so simple thresholding cannot successfully separate the hole features from the background.

The grid object was removed and a flat-field image was acquired. Figure 4.3 shows a slice at the same row position for this image. This image is called a "flat-field" image since it is an image of a uniform source. Following a calibration procedure used for CCD sensors (Photometrics, 1991), the gray level grid image was divided point-wise by the flat-field image; a slice at the same row location for this quotient image is shown in Figure 4.4.

The background is now uniform, so a constant threshold value in the range 0.7–0.8 effectively thresholds the image (the quotient image gray levels range from 0 to 1). This result is indicated in Figure 4.5 (it is displayed using black for the hole features and white for the background). The characteristic pincushion distortion is evident in this image, and is most pronounced at the edges of the image.

A procedure was developed to automatically determine the centroids of the white pixel clusters. Previous workers (Chakraborty, 1987) used a manually-guided cursor to identify these centroids, which limited the amount of data that could be practically obtained. The basic idea of the automatic method is to identify a small region of interest (ROI) about each hole and calculate the centroid of all white pixels within that ROI. This procedure requires the user to identify a minimum X (x_{min}) and Y (y_{min}) hole spacing from the center of the image where distortion is minimal to define the dimensions of the ROI.

Figure 4.6 shows a diagram of the upper left corner of the image data. The true centroids of the top three features are $C_1 = (x_1, y_1)$, $C_2 = (x_2, y_2)$, and

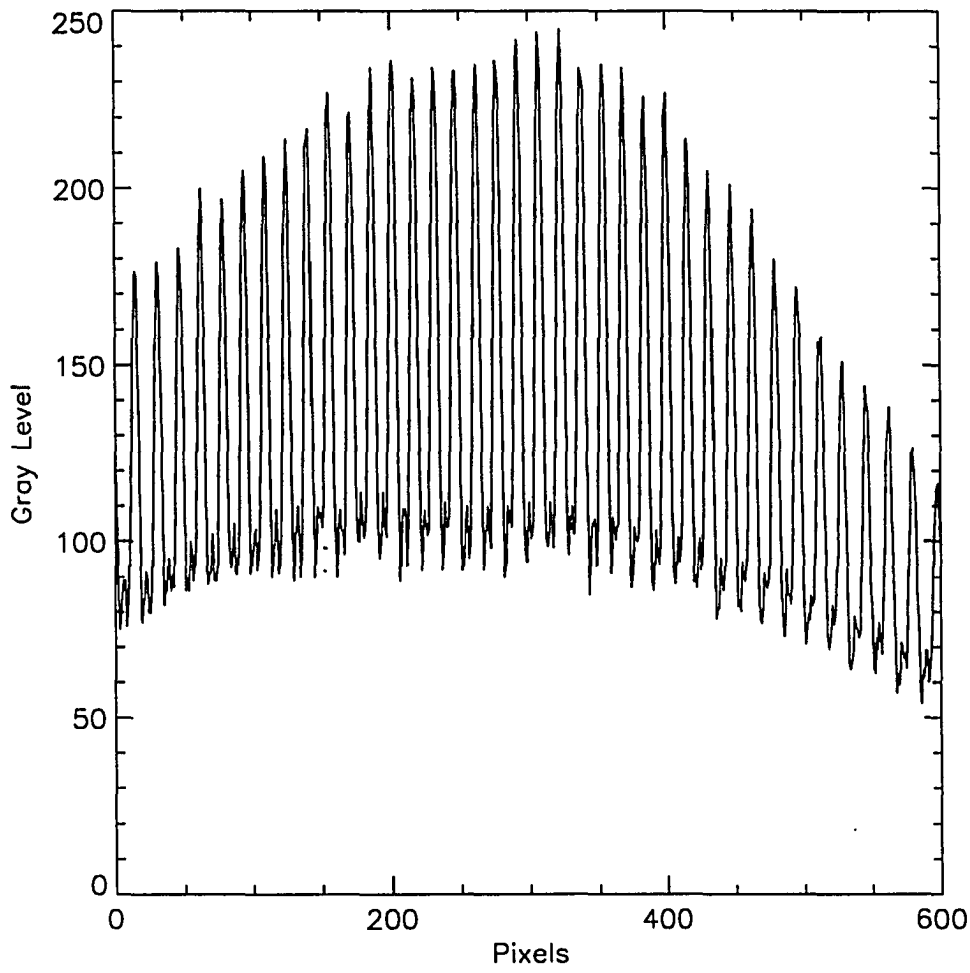

Figure 4.2: Row slice of reference grid image for pincushion distortion measurement

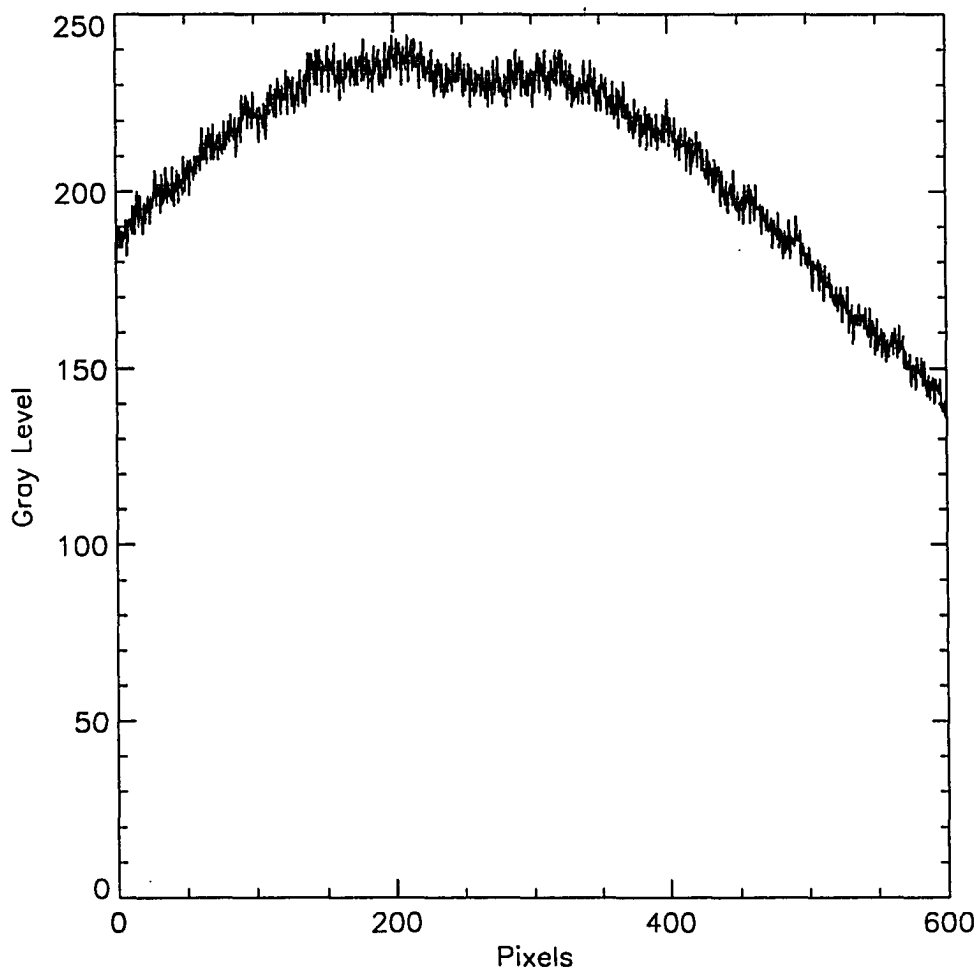

Figure 4.3: Row slice of flat-field image obtained by imaging only the X-ray source

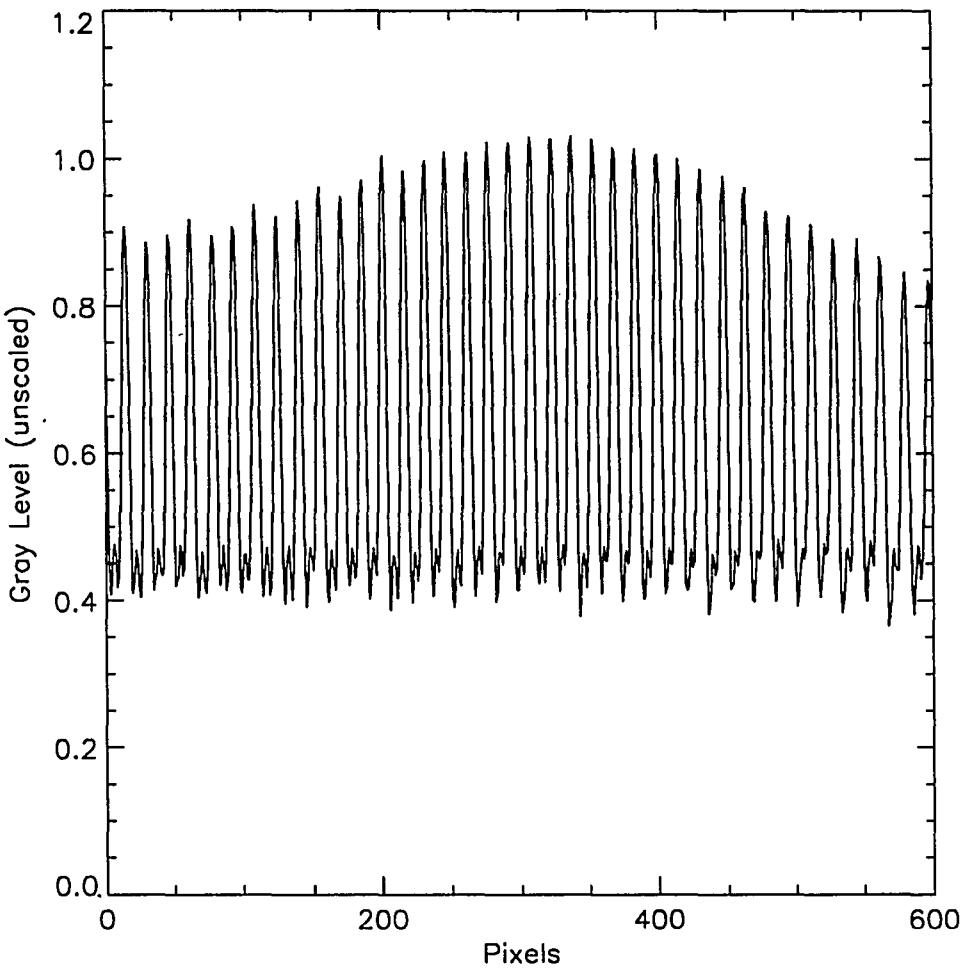

Figure 4.4: Row slice after dividing by flat-field image

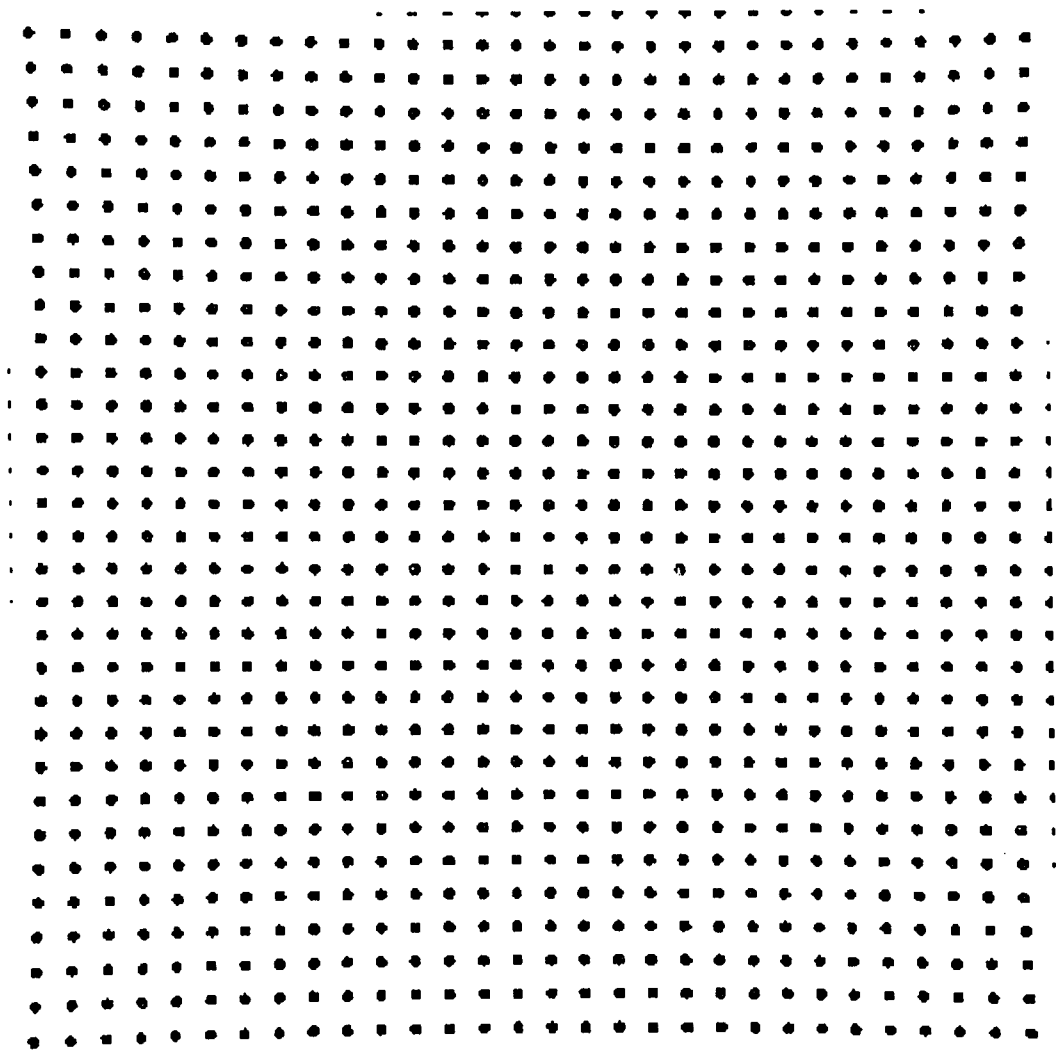

Figure 4.5: Thresholded pincushion distortion image

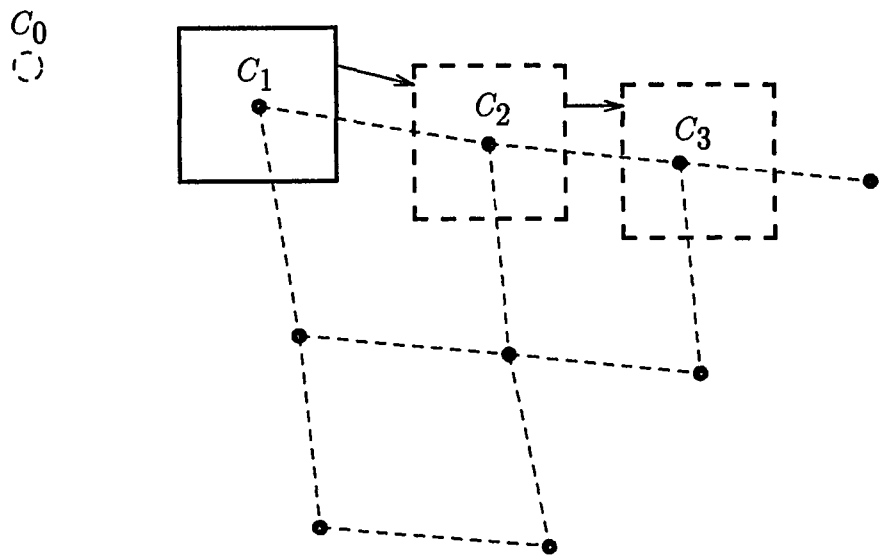

Figure 4.6: Diagram of upper left corner of pincushion distortion data

$C_3 = (x_3, y_3)$. The user supplies an initial guess about the positions of the first two centroids using a mouse-guided cursor. These guesses are denoted $\tilde{C}_1 = (\tilde{x}_1, \tilde{y}_1)$ and $\tilde{C}_2 = (\tilde{x}_2, \tilde{y}_2)$. From these guesses, a hypothetical centroid $C_0 = (x_0, y_0)$ is determined as

$$x_0 = \tilde{x}_1 - (\tilde{x}_2 - \tilde{x}_1) = 2\tilde{x}_1 - \tilde{x}_2 \tag{4.2}$$

$$y_0 = \tilde{y}_2. \tag{4.3}$$

This hypothetical centroid is used to initialize the following centroid prediction equations:

$$\hat{x}_{i+1} = 2x_i - x_{i-1}, \quad i = 1, 2, \ldots \tag{4.4}$$

$$\hat{y}_{i+1} = y_i.$$

At each step i, the ROI is centered about the estimated centroid position $(\hat{x}_i, \hat{y}_i)$.

The centroid of the white pixels within the ROI is determined as

$$x_c = \frac{1}{W} \sum_{j=x_b}^{x_e} \sum_{k=y_b}^{y_e} x(j,k) \qquad (4.5)$$

$$y_c = \frac{1}{W} \sum_{j=x_b}^{x_e} \sum_{k=y_b}^{y_e} y(j,k)$$

where W equals the number of white pixels within the ROI, $x_b = \hat{x}_i - (x_{min}/2)$ is the beginning index of the window x coordinate, and $x_e = \hat{x}_i + (x_{min}/2) - 1$ is the ending index of the window x coordinate (similarly for y_b and y_e). This value is saved and used as the true centroid (x_i, y_i). This process is repeated until all hole centroids of the first row are measured. A similar prediction procedure is used to predict the initial hole position of the next row. The entire process is repeated until all hole centroids in the image are measured. The centroid data set is subsequently analyzed to determine the pincushion distortion image warp coefficients.

Calculation of image warp coefficients

The distorted hole positions were determined using the display screen coordinate system. The center of the image intensifier phosphor screen was estimated by affixing a lead marker to the center of the input screen and recording its coordinates in the screen coordinate system. This was subtracted from each data point to center the centroid data about zero. The sampling frequency was determined by counting the number of pixels between a series of holes in the center of the image where distortion is minimal, averaging them, and dividing by 0.254 cm (the hole spacing of the grid phantom). This value was 59.7 pixels/cm in the horizontal direction and 57.7 pixels/cm in the vertical direction. A reference data set was computed

and aligned with the distorted data set, with the result plotted in Figure 4.7. The distance between each distorted hole from the origin was compared to the distance of the reference grid. This error is plotted in Figure 4.8. The plot points correspond to traversing the centroids from left to right and top to bottom. The vertical dashed lines in Figure 4.8 indicate each row. The error is low in the center of each row and high at the ends of each row. Also note that the error reaches a maximum of 0.45 cm (27 pixels).

These data sets were input to a polynomial curve fitting routine to determine the following mapping function:

$$X_c = \sum_{i=0}^{3} \sum_{j=0}^{3} A_x(i,j) X_d^j Y_d^i \tag{4.6}$$

$$Y_c = \sum_{i=0}^{3} \sum_{j=0}^{3} A_y(i,j) X_d^j Y_d^i \tag{4.7}$$

where (X_d, Y_d) are the coordinates of the distorted hole position, (X_c, Y_c) are the coordinates of the corrected hole position, and $\mathbf{A}_x$, $\mathbf{A}_y$ are 4×4 matrices of polynomial coefficients. Figure 4.9 shows a plot of the distance errors for the corrected data. The average error was 8×10^{-5} cm, the standard deviation was 0.002 cm, and the maximum error was -0.008 cm. The maximum error matches the half-pixel uncertainty due to quantization of $(2{\times}60 \text{ pixels/cm})^{-1} = 0.008$ cm. Figure 4.10 shows an overlay plot of the original centroid locations, the expected (reference) locations, and the corrected locations.

This mapping function is invoked whenever a display screen coordinate value is converted to the global coordinate system. Changing the X-ray source position introduces a view-dependent distortion (Chakraborty, 1987), so the coefficients of this technique are only valid for a specific source/detector geometry.

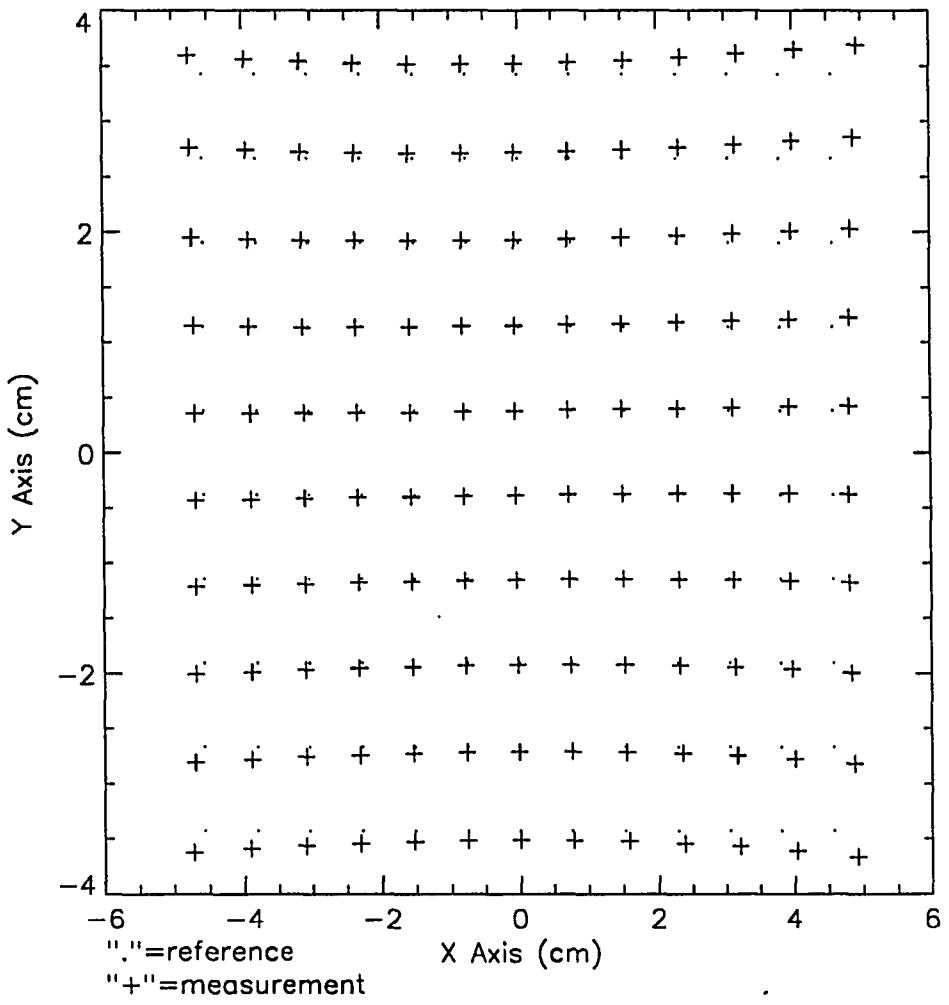

Figure 4.7: Measured centroid locations compared to reference

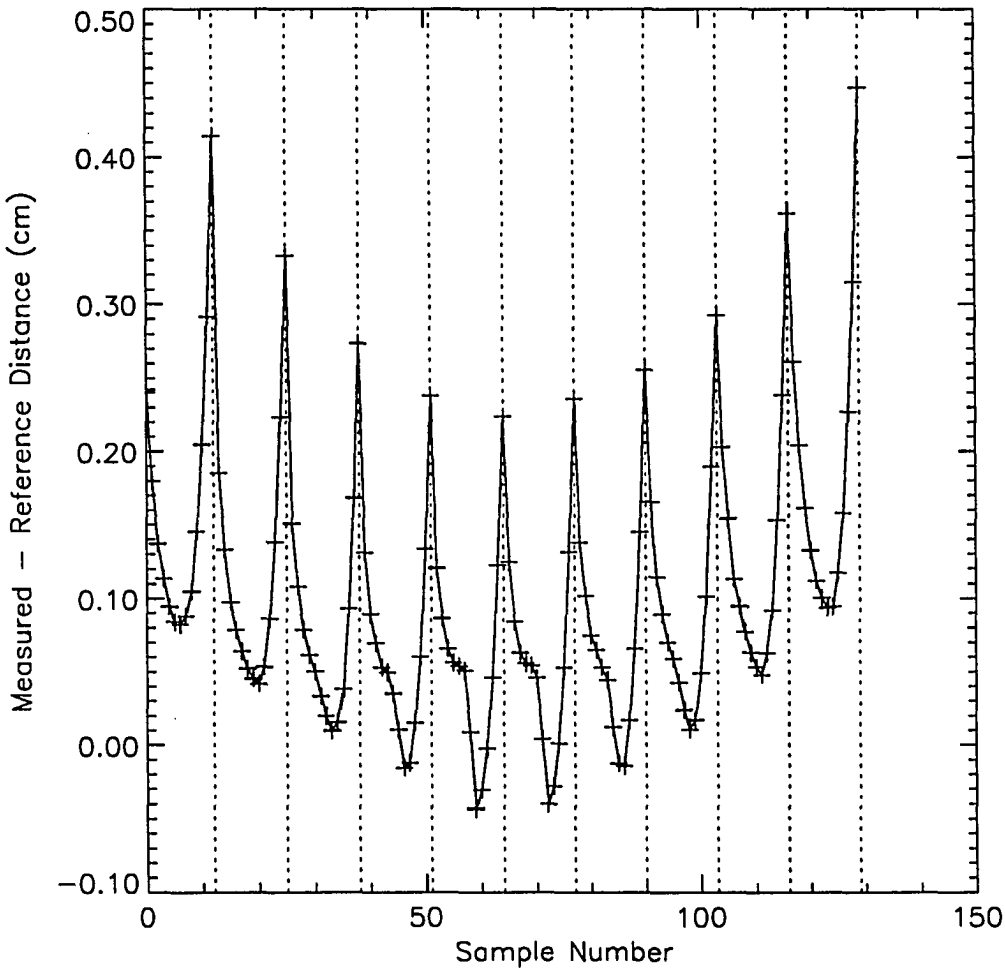

Figure 4.8: Positional error of measured centroids compared to reference

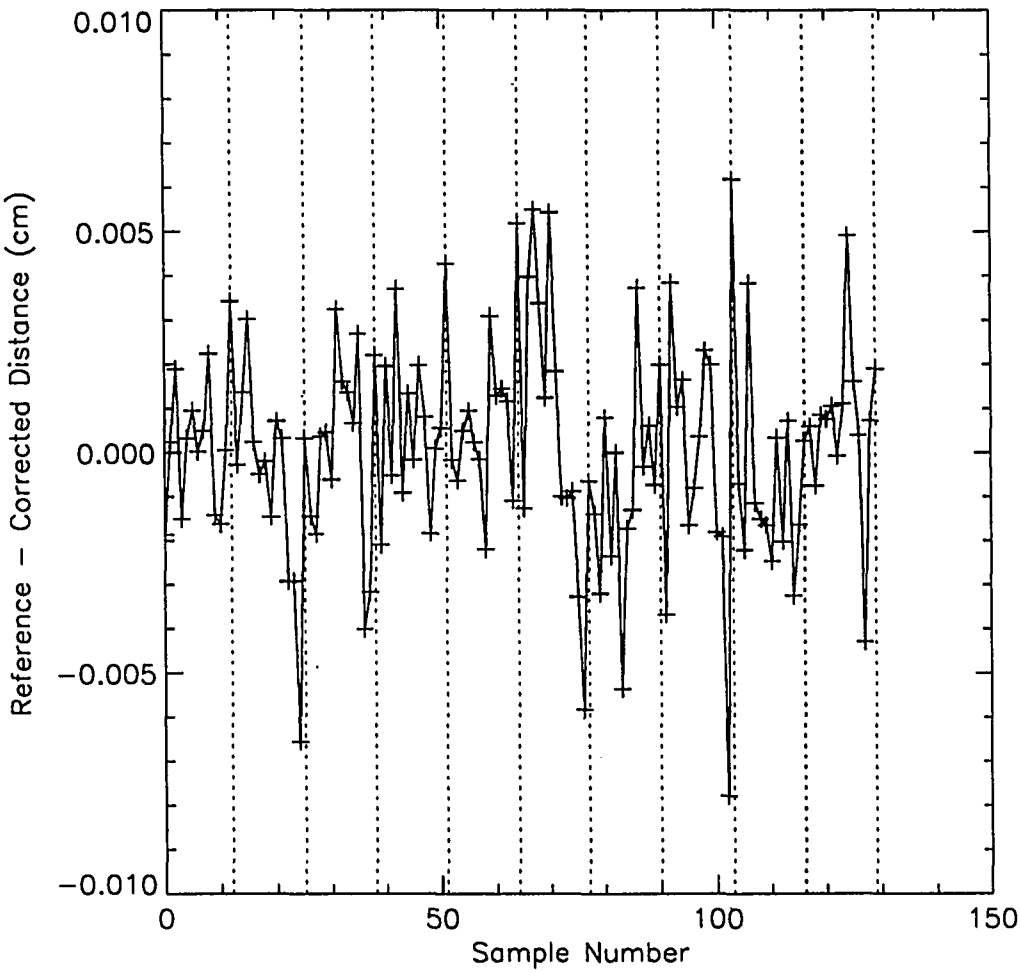

Figure 4.9: Residual error of polynomial warp model

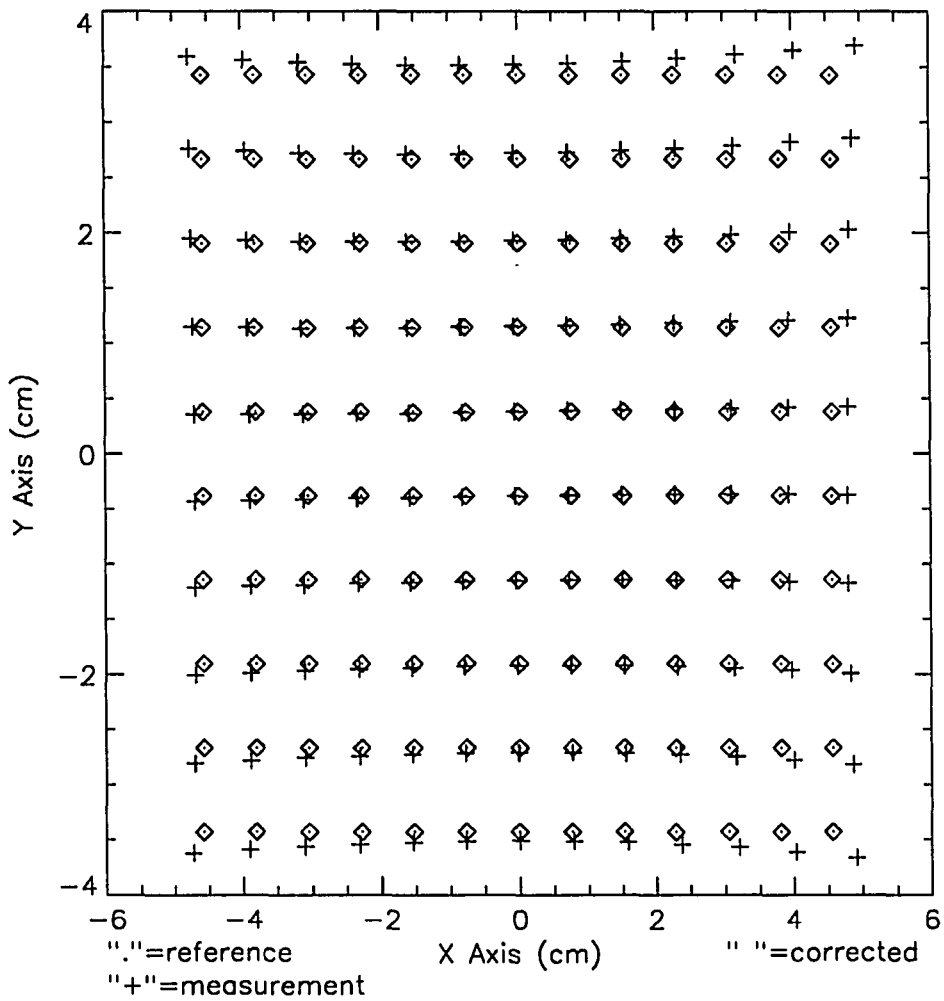

Figure 4.10: Corrected centroid locations using polynomial model

Improvement of Spatial Resolution

An image restoration routine is used to reduce the blurring caused by phosphor bloom within the image intensifier. Phosphor bloom causes the image of an input ideal impulse function to blur into an output image function with non-zero width (Csorba, 1985). This impulse response of the imaging system is known as the point spread function (PSF). Image restoration routines have been to developed to reduce image blurring by deconvolving an estimate of the PSF from the measured image. The first part of this section describes a method used to identify the PSF of the image intensifier with enough accuracy to be used in an image restoration routine, and the second part describes the use of the Maximum Entropy Method as a means to deconvolve the measured PSF.

Point spread function determination

The point spread function describes the impulse response of an optical system. The modulation transfer function (MTF) is the magnitude of the Fourier transform of the point spread function and measures the frequency response of the optical system. Creating an impulse function as an input to the image intensifier is experimentally difficult since an infinite amount of X-ray photons are required to be collimated in an infinitesimally small beam. Optical systems have similar difficulties in obtaining a light beam impulse. A practical approach is to use an optical knife edge which presents a step function input to the system (Williams, 1989). This has been used to measure the MTF of optical lenses and CCD arrays. A step function is an integrated impulse function, so differentiating the knife edge response function yields what would have been imaged had an impulse function been applied to the system. The measured

response is unavoidably corrupted by some amount of noise. This noise is amplified by numerical differentiation, hence this technique has limitations. The simplest approach is to image the edge and estimate the derivative using the first difference of an image row (or column) across the edge. The optical knife edge-based measurement for X-ray systems is implemented using the edge of a lead plate. The primary drawback of this method is undersampling in the edge transition region, where only 5 to 10 pixel values are available to characterize the edge (Doering, Gray, and Basart, 1992).

Reichenbach, Park, and Narayanswamy (1991) apply a more sophisticated approach to CCD characterization where the knife-edge is positioned at a very slight angle with respect to the row of pixels. This yields an ensemble of edge profiles, each slightly shifted, that when properly registered and averaged provide a sub-pixel resolved edge profile with minimal measurement noise. Unfortunately, pincushion distortion makes the technique impractical for characterizing image intensifiers. Reichenbach's technique relies heavily on the inherent uniformity of the CCD array, while the non-uniform magnification caused by pincushion distortion and other aberrations (Csorba, 1985) prohibits accurate registration of edge scans acquired over a large area of the intensifier screen. Glasser, Vaillant, and Chazallet (1988) describe an alternative method where the output of a single pixel is monitored while the knife-edge is shifted in sub-pixel increments. This avoids the problems due to spatial distortion and provides an accurate PSF estimate in a local area. This technique has more noise than Reichenbach's method, but this problem can be alleviated by acquiring and averaging many scans over the edge transition region. Both techniques are limited to estimating the 1-D PSF; however, the tube may be rotated relative to

the plate in order to characterized the 2-D PSF. Glasser's technique was implemented here for characterizing the image intensifier PSF.

The imaging chain from the image intensifier input screen to the focal plane of the CCD detector is modelled as a continuous convolution (Andrews and Hunt, 1977); in 1-D notation this is

$$g(x) = f(x) * h(x), \tag{4.8}$$

where $f(x)$ is the input X-ray field, $g(x)$ is the output optical field at the focal plane of the detector, and $h(x)$ is the system PSF. In this work the effects of finite pixel width and coupling optics are lumped into $h(x)$ and the sampler is considered an ideal point sampler (Cunningham and Fenster, 1987). Now, let the input function $f(x)$ be an ideal step function $s(x)$. For this special case, the system function is found by differentiating the step function output with respect to the position x (Williams, 1989):

$$h(x) = \frac{dg(x)}{dx}. \tag{4.9}$$

The sampled function is $h(na)$, where a is the distance between pixels, also called pixel pitch, and n is the pixel index. As mentioned previously, a is too large to provide enough resolution in the edge transition region. Since a is fixed, the step input $s(x)$ is shifted an amount $\Delta x \leq a$. This new input $s(x - m\Delta x)$ yields $h(x - m\Delta x)$ upon differentiation, where m is the index of the plate position.

For example, the 6" image intensifier was set up for a sampling frequency of 6 pixels/mm referred to the input screen of the image intensifier. This resulted in an effective pixel pitch of $a \simeq 170\mu m$. Using a step size of $a = 10\mu m$ yields a sampling frequency of 100 pixels/mm, which is 17 times greater than that possible with the

CCD array alone. This resulted in much better resolution in the edge transition region and hence a better estimate of the PSF shape.

The X-ray source was placed 110 cm from the lead plate and was operated at 75 kV at 300 μA. The lead plate was mounted on the sample positioner and placed 4 cm from the input screen of the image intensifier resulting in 1:1 magnification. The edge of the plate was aligned with the central axis of the X-ray source to minimize blurring due to geometrical unsharpness.

Two image intensifiers were used: a 6" single field and a 9" dual field (normal mode and magnification mode). The same coupling lens and CCD video camera were used for both tubes. The video signal was digitized to a 480 $\times$ 640 pixel 8-bit image. The video gain and offset were held constant for both tube configurations to maintain the same electronic noise level for all measurements. Since the optical output of the 9" image intensifier was significantly reduced when operated in the magnification mode, the X-ray source current was increased to 900 μA to maintain the same signal level.

Data were acquired by first selecting the measurement pixel (typically the center pixel of the image) and adjusting the lead plate position until the pixel response (gray level) reached half maximum. This position was selected as the zero location. Following this procedure the plate was moved to the starting point of the scan. At this point the plate covered the measurement pixel for the scan. The plate was stepped in 10 μm increments and at each position 64 video frames were averaged. The total scan length (400 points) was chosen to include enough measurements outside the transition region to identify where the gray values leveled off. The sampling frequency was determine by first acquiring an image of the lead plate in a reference position and

acquiring a second image of the plate translated 2 cm from the reference position. The pixel location of the edge was determined from each image. The difference in pixels divided by 2 cm yielded the sampling frequency of 60 pixels/cm. This value was used to convert the plate position into pixel units.

Generally the central pixel was used for the measurement pixel and the plate was translated vertically. Variation due to pixel location was investigated for the 9" image intensifier using measurement pixels in the four corners of the acquired image. Variation due to plate translation direction (horizontal instead of vertical) was investigated with the 6" image intensifier. A total of nine data sets was collected.

An example measurement of the 9" image intensifier operated in normal mode is shown in Figure 4.11. The signal-to-noise ratio (SNR) is calculated as

$$SNR_{dB} = 10 \log_{10} \frac{(g_{max} - g_{min})^2}{s_{min}}, \tag{4.10}$$

where g_{max} is the average value of the high intensity portion of the scan, g_{min} is the average value of the low intensity portion of the scan, and s_{min} is the standard deviation of the signal in the low intensity portion of the scan. All three values were measured outside the transition region where the signal is stationary. The first 50 and last 50 samples of the edge scan were used for these regions. The SNR for the scan in Figure 4.11 was 51 dB which is consistent with an 8-bit digitizer. The typical gray level fluctuation outside the edge transition region was 1 gray level. The samples between +7 and +10 pixels in Figure 4.11 contained only digitizer-related noise while the samples between −7 and −10 pixels included photon counting noise.

Figure 4.12 shows the result of numerically differentiating the scan in Figure 4.11 using the forward difference approximation $y(n) = x(n+1) - x(n)$. Due to the small step size, the difference in intensity between successive pixel values never exceeds 4

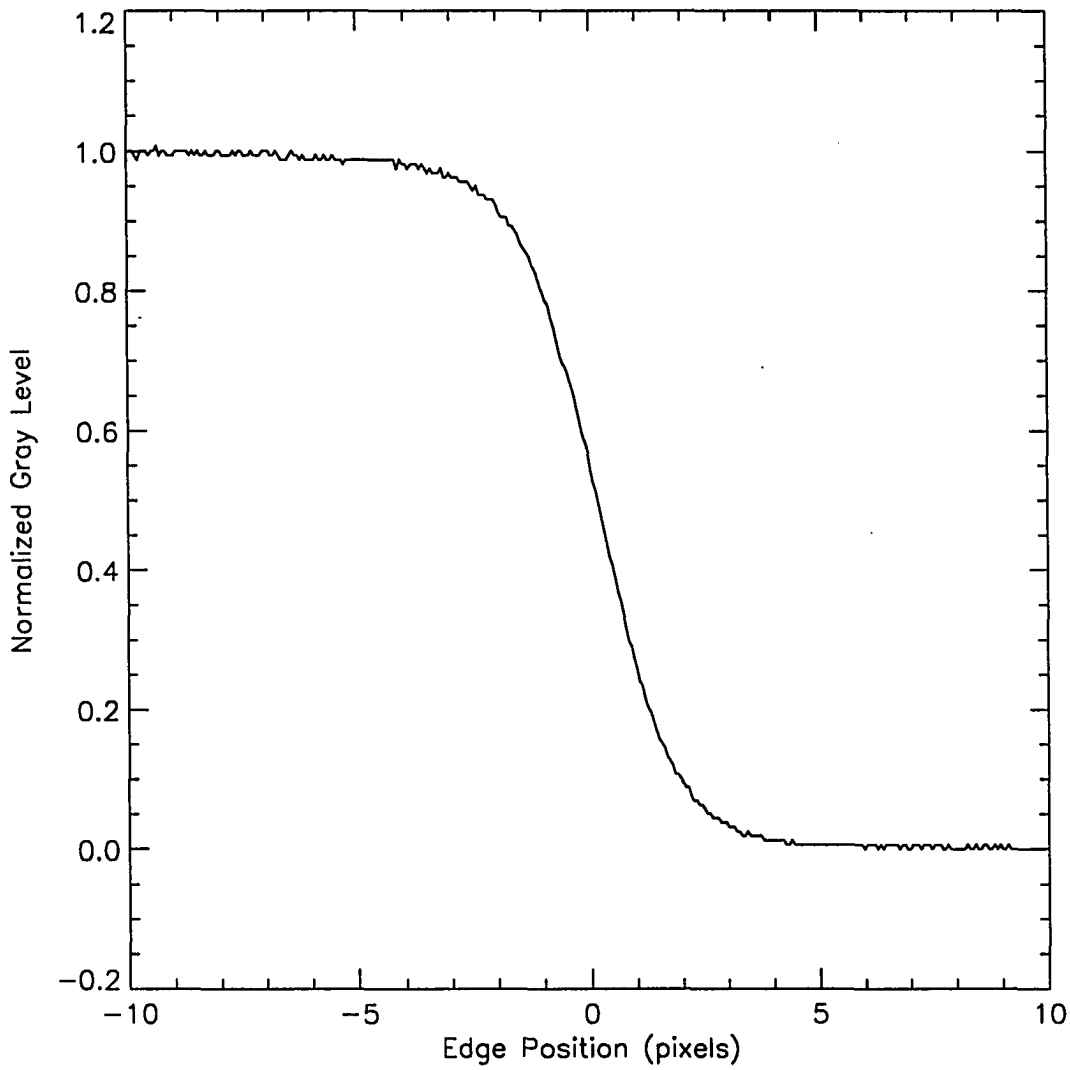

Figure 4.11: High resolution edge scan data for PSF measurment

in the transition region, so the 1 gray level noise variation becomes very prominent. To reduce the effects of noise, the scan in Figure 4.12 was smoothed with a uniformly weighted convolution filter nine pixels wide prior to differentiation; the result is shown in Figure 4.13. The shape of the PSF is now much more evident. Smoothing increases the width of the measured PSF, although the increase was only 1% for this choice of convolution filter.

A Gaussian function was fit to the differentiated data to measure the full-width-at-half-maximum (FWHM; FWHM=2.354 times the standard deviation of the Gaussian function). Note that the Gaussian follows the smoothed derivative in Figure 4.13 very well. This is expected since the combined PSFs of the many separate components in the imaging chain tend to a Gaussian due to central limit effects (Andrews and Hunt, 1977). However, it is known that some aspects of the combined system PSF are not described by a Gaussian PSF, notably the PSF of the circular aperture of the video camera lens. This PSF has a sinc function-like form in the frequency domain and hence has zeroes which are not modeled with a single Gaussian function. The lens aperture for this study (f/5.8) resulted in the first zero occurring beyond the folding frequency, so the zero occurred outside the passband of the image intensifier/video camera chain. Decreasing the aperture would further increase the frequency of the first zero crossing, but this would require a greater X-ray field intensity to maintain a given average image intensity.

The goodness of fit was assessed using the reduced chi-square statistic $\chi^2_\nu = s^2/\sigma^2$ (Bevington, 1969), where s^2 is the variance of the fitting error and σ^2 is the variance in the data due to measurement error. The measurement error was estimated

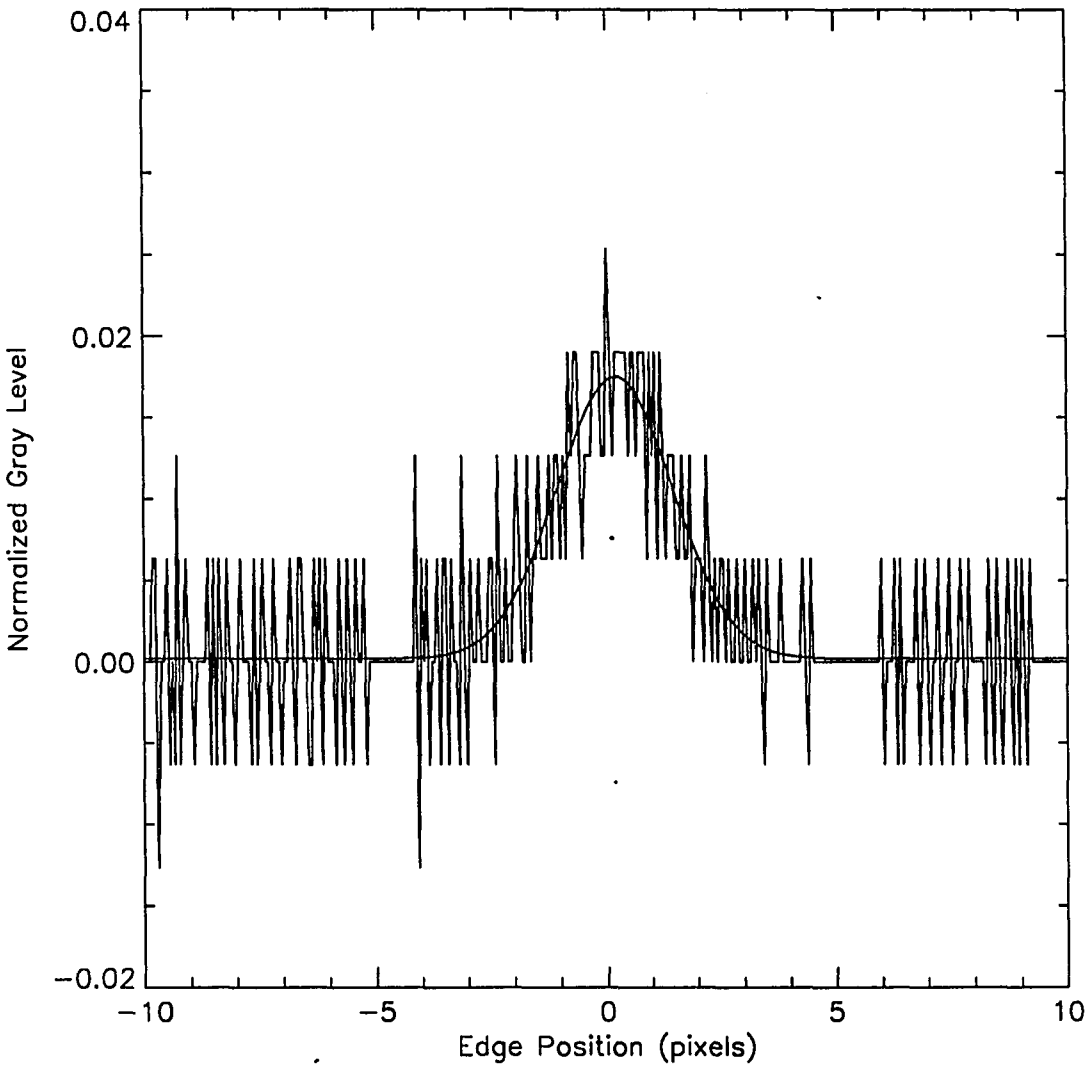

Figure 4.12: Numerical derivative of edge scan data (pulse-like signal), with overplot of fitted Gaussian (smooth signal)

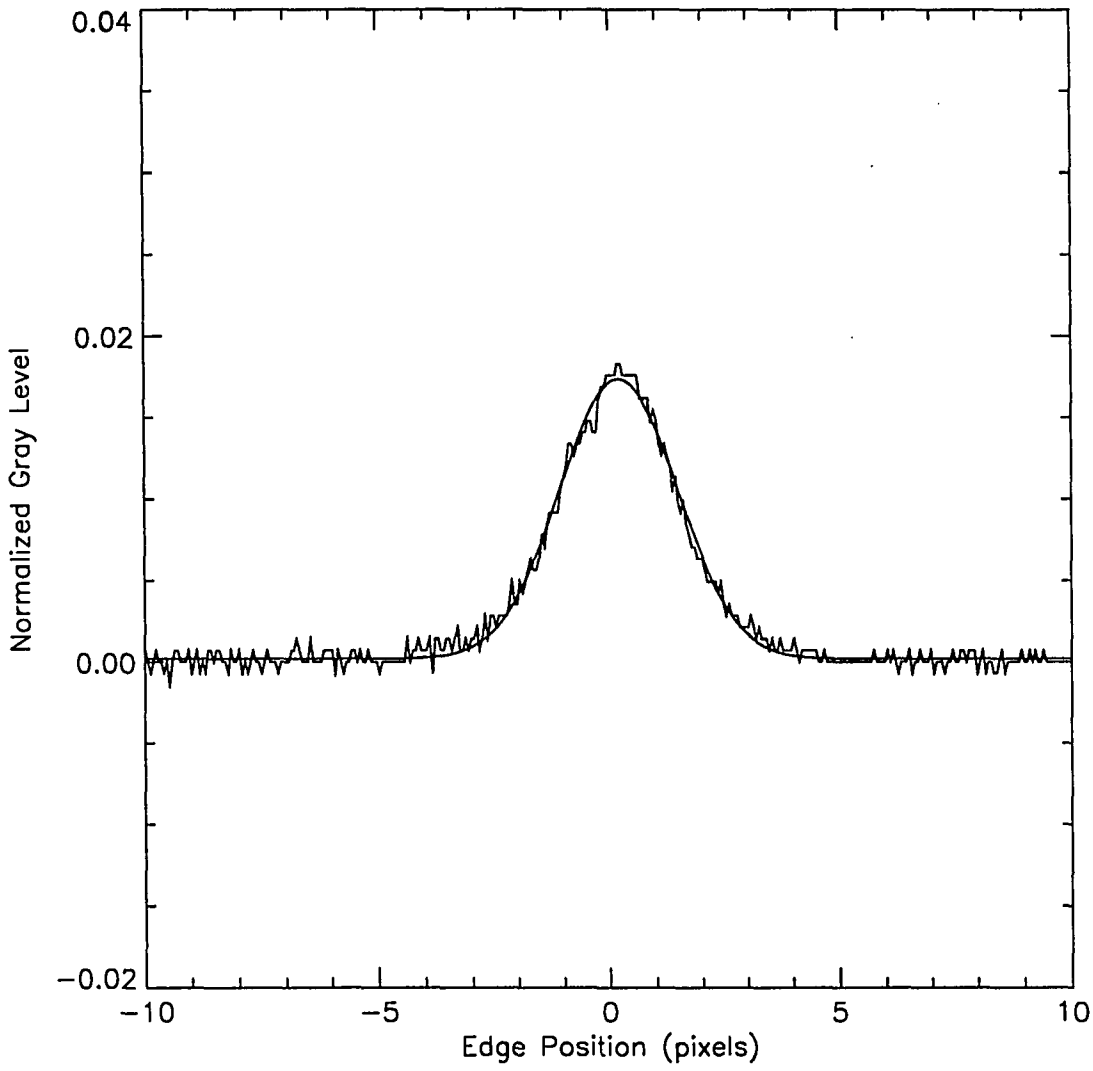

Figure 4.13: Numerical derivative of smoothed edge scan data (noise-like signal), with overplot of fitted Gaussian (smooth signal)

Table 4.1: FWHM values for edge scan measurements

Data Set Number	Image Intensifier	Measurement Pixel Location	Scan Direction	SNR (dB)	χ^2_ν	FWHM (pixels)
1	9" normal	center	vertical	51	0.81	4.2
2	9" mag	center	vertical	52	1.22	4.2
3	9" normal	upper left	vertical	51	0.86	3.9
4	9" normal	upper right	vertical	50	1.01	5.8
5	9" normal	lower right	vertical	51	0.92	5.1
6	9" normal	lower left	vertical	50	0.93	4.2
7	9" normal	center	horizontal	50	0.92	3.9
8	9" mag	center	horizontal	50	1.09	4.2
9	6"	center	horizontal	56	0.69	2.9

by computing the variance of 100 samples outside the edge transition region. χ^2_ν for this data set was 0.95 ($\chi^2_\nu \simeq 1$ indicates a good fit).

The Gaussian fit was made to the derivatives of both the smoothed and unsmoothed scans. Since there was less than 1% change in any of the fitting parameters, smoothing the scan data is acceptable for revealing the shape of the PSF, but is not required to determine the PSF width (i.e., the FWHM).

Table 4.1 lists the experimental results for the 6" and 9" image intensifiers. The measurement error was determined by repeating the FWHM measurement for the 6" image intensifier nine times. The standard deviation was 5% of the mean FWHM value. Variation due to lead plate orientation was investigated using the 9" image intensifier in both normal and magnification modes. Data sets 1,2,7, and 8 correspond to this investigation. Note that the FWHM values remain essentially unchanged between normal and magnification modes. However, the FWHM value for data set 7 differs by 8% compared to the other 3 measurements. Since this measurement

was not repeated, additional experimentation is necessary to determine if this is a significant difference. Except for data set 7, no significant variation was found due to orientation of the lead plate.

Data sets 3 to 6 investigate the effect of choosing different measurement pixel locations in the image. The standard deviation of these data sets including data set 1 was 0.79 pixels, or 19% of the FWHM value for the center pixel location. This large variation is attributed to non-uniform magnification due to pincushion distortion. This distortion is expected to give a wider PSF away from the central pixel, particularly in the corners which are furthest from the center. The FWHM values for data sets 4 and 5 were significantly larger than the central value (data set 1) as expected, yet the values for data sets 3 and 6 were nearly the same as the central value. The same camera mount was used for both tubes (but was designed only for the 6" tube) and was not a good match for the 9" tube in terms of centering the output phosphor on the acquired image. Furthermore, the entire output phosphor was not in the field of view of the video camera. Consequently, the measured FWHM values did not follow the pattern expected by a properly centered camera.

The motivation for this method was to estimate the PSF with enough accuracy to use in an image restoration algorithm. This method is sufficient to determine the FWHM parameter when a Gaussian model is selected for the analytical PSF. However, the shape estimate is too noisy to be used directly in the restoration routine. Many scans would need to be averaged to achieve low enough noise. Since this is very time consuming, an alternative method would be to use a cluster of measurement pixels about the central measurement pixel. Spatial invariance of the image intensifier

PSF is valid for this small neighborhood, and this ensemble of the edge scans can be precisely registered since they are offset by a known amount (i.e., the pixel pitch).

Image restoration

Image restoration techniques attempt to recover some aspect of an image that was degraded due to the action of the image acquisition device. In optical imaging, camera movement during exposure causes motion blur in the acquired image, and a defocused lens also results in a blurry image. Once a model of the degradation process is determined, image restoration procedures estimate an input image, that when degraded by this modelled process, closely matches the measured image at hand. The point spread function serves as the degradation model. Many image restoration techniques have been developed; most computationally tractable methods assume a convolution with a spatially invariant PSF as the blurring mechanism, and the addition of Gaussian noise as the noise mechanism (Andrews and Hunt, 1977); methods also have been developed using a Poisson noise model (Meinel, 1986), which better models image formation processes based on photon counting.

The more well-known techniques include inverse filtering, least-squares (Wiener) filtering, and constrained least-squares filtering (Gonzalez and Wintz, 1977). Inverse filters deconvolve the PSF by converting the measured image to the frequency domain, dividing by the Fourier transform of the PSF (system function), and converting the result back to the spatial domain. This technique is extremely noise-sensitive, and any zeroes in the system function result in singularities. The least-squares filters use both a system model and a noise model to reduce noise sensitivity. These linear methods

are implemented in the frequency domain to take advantage of the computational efficiency of the fast Fourier transform (FFT) algorithms.

Nonlinear restoration methods (Meinel, 1986) often do a better job of modeling the imaging system. For example, image sensors (both film and solid state) have nonlinear characteristics that influence the conversion of a pixel's gray level to a physical unit. This characteristic can be modelled and incorporated into a nonlinear image restoration algorithm. Furthermore, linear methods do not place a constraint on the sign of the pixel values of the restored image, so negative pixel values can result, even though this is physically meaningless. Nonlinear routines can be designed with constraints to eliminate this problem. The major drawbacks to nonlinear methods include computational complexity, and the need to use iterative solutions (hence, they are time-consuming).

The Maximum Entropy Method (MEM) image restoration technique was implemented to restore the real-time image which has been blurred by phosphor bloom. The primary advantages of MEM are positivity of the restored image and minimization of the ringing artifacts and noise sensitivity associated with inverse filters. MEM (or any other image restoration technique) requires an estimate of the point spread function (PSF) responsible for blurring the image. In some applications the image formation system is not available, so the PSF must be estimated directly from the image (Tekalp, Kaufman, and Woods, 1986; Chalmond, 1991). This is not a problem in the RTR laboratory, so the PSF is measured separately from acquiring the image data, as described previously.

The Maximum Entropy Method (MEM) has been used successfully for spectral estimation and image restoration (Freiden and Wells, 1978; Burch, Gull, and Skilling,

1983; Gonsalves *et al.*, 1990). The methods of Burch, Gull, and Skilling and others have been steadily refined and implemented in a commercial software package called MEMSYS3. This is considered the standard MEM reconstruction algorithm (Fougère, 1990). The latest version is MEMSYS5. These algorithms are general purpose, proprietary, expensive, and require hundreds of 2-D (FFTs) per image. A method based on Newton-Raphson iteration (Cornwell and Evans, 1985; Zheng and Basart, 1988; Doering and Basart, 1991b) was implemented instead. It has the advantage of requiring only two 2-D FFTs per iteration at 15–20 iterations per image.

The MEM restoration is based on a linear image formation process, a spatially invariant blurring function, and additive white noise (the invariant PSF requirement is not inherent to the MEM technique, but is required for efficient computation of convolutions using the FFT):

$$\mathbf{g} = \mathbf{H}\mathbf{f} + \mathbf{n}, \qquad (4.11)$$

where $\mathbf{f}$ is the original uncorrupted image, $\mathbf{H}$ is a square matrix containing the point spread function, $\mathbf{n}$ is a white noise sequence, and $\mathbf{g}$ is the measured image. The two-dimensional image is lexicographically ordered to form the column vector $\mathbf{f}$. These assumptions are not strictly correct for the real-time image. The PSF width increases off-axis due to pincushion distortion, and the noise distribution is Poisson due to the photon counting process. However, trying to use a more physically correct model substantially increases the complexity of the restoration problem. The real-time image does not substantially deviate from the ideal, so the method is applied while acknowledging the possibility of sub-optimal performance.

The objective of the restoration is to find an estimate of the original image $\hat{\mathbf{f}}$ that incorporates a minimum of additional configuration or image modelling information.

Furthermore, the blurred estimate $\mathbf{H}\hat{\mathbf{f}}$ should be consistent with the original measurement in a squared-error sense. The first condition corresponds to an estimated image with maximal entropy and the second condition corresponds to an estimated image that when blurred closely matches the measurement.

The entropy S of the estimated image is calculated as

$$S = -\sum_{i=0}^{N-1} p_i \ln p_i, \tag{4.12}$$

where $p_i = \hat{f}_i / \Sigma \hat{f}_i$ is the probability density of the image gray levels, i is the pixel index, and N is the number of pixels in the image. The chi-squared statistic χ^2 is used to measure the consistency of the blurred estimate with the measurement:

$$\chi^2 = \| \mathbf{g} - \mathbf{H}\hat{\mathbf{f}} \|^2. \tag{4.13}$$

In general, χ^2 is defined by weighting each squared difference by $1/\sigma_i^2$, where σ_i^2 is the variance associated with each measurement; here the variance of each element is taken as unity since all pixels in the image are considered to have the same variance. An objective function Q is formed from the entropy and chi-squared functions by:

$$Q(\hat{\mathbf{f}}) = S(\hat{\mathbf{f}}) - \lambda \chi^2(\hat{\mathbf{f}}), \tag{4.14}$$

where λ is a Lagrange multiplier. The goal of the MEM is to search for an image $\hat{\mathbf{f}}$ that maximizes the objective function Q, since this maximizes entropy (S), and minimizes the error (χ^2). This maximization is carried out by finding a root of

$$\frac{\partial Q(\hat{\mathbf{f}})}{\partial \hat{\mathbf{f}}} = \frac{\partial S(\hat{\mathbf{f}})}{\partial \hat{\mathbf{f}}} - \lambda \frac{\partial \chi^2(\hat{\mathbf{f}})}{\partial \hat{\mathbf{f}}} = \mathbf{0}. \tag{4.15}$$

The entropy gradient is computed as

$$\frac{\partial S(\hat{\mathbf{f}})}{\partial \hat{\mathbf{f}}} = -\frac{1}{\Sigma f_i} \ln(\hat{\mathbf{f}} + \epsilon), \tag{4.16}$$

where ϵ is a small constant (1.0^{-12}) to keep the logarithm argument non-zero. The chi-squared gradient is computed by blurring (convolving) the residual $\hat{\mathbf{g}} - \mathbf{g}$ with the PSF. Convolution is carried out in the frequency domain by multiplication:

$$\frac{\partial \chi^2(\hat{\mathbf{f}})}{\partial \hat{\mathbf{f}}} = 2\mathcal{F}^{-1}\{\mathcal{F}\{h\}\mathcal{F}\{\hat{g} - g\}\}, \tag{4.17}$$

where $\mathcal{F}\{h\}$ is the forward Fourier transform of the PSF, $\mathcal{F}\{\hat{g} - g\}$ is the forward Fourier transform of the residual image, and $\mathcal{F}^{-1}\{\cdot\}$ is the inverse Fourier transform operator. $\hat{\mathbf{g}} = \mathbf{H}\hat{\mathbf{f}}$ is computed using the FFT once each iteration, and the inverse transform requires an FFT computation as well, hence there are two required FFTs per iteration.

The Newton-Raphson method is used to iteratively solve the nonlinear function (Equation 4.15) as an optimization problem (Cornwell and Evans, 1985). A new estimate of the restored image is found using

$$\mathbf{f}^{(n+1)} = \mathbf{f}^{(n)} - \left(\frac{\partial^2 Q^{(n)}}{\partial \hat{f}_i \partial \hat{f}_j}\right)^{-1} \cdot \frac{\partial Q^{(n)}}{\partial \hat{\mathbf{f}}}, \tag{4.18}$$

where n is the iteration index.

The quantity $\left(\frac{\partial^2 Q^{(n)}}{\partial \hat{f}_i \partial \hat{f}_j}\right)^{-1}$ is an $N^2 \times N^2$ matrix, where N is the number of pixels in the image. Cornwell and Evans (1985) show that the off-diagonal elements are much smaller than the on-diagonal elements, so they compute the required inverse matrix by setting the off-diagonal elements to zero and taking the reciprocal of the on-diagonal elements; this technique was followed here.

$\hat{\mathbf{f}}$ is initialized to a constant valued image using the average value of $\mathbf{g}$. This is the maximum entropy image, with a correspondingly large value of χ^2. Thus λ must start at a small value. As the iteration progresses, λ is increased to approach its final

value by adding the increment $\Delta\lambda$ defined as

$$\Delta\lambda = \frac{-\Delta\chi^2}{\sum_{i=0}^{N-1}\left[\frac{\partial\chi^2}{\partial\hat{f}_i}\right]^2}, \tag{4.19}$$

where $\Delta\chi^2$ is the change in error from the previous iteration. Convergence occurs when the residual of the blurred estimate and the originally measured image approaches a Gaussian noise image. It was found that fifteen to thirty iterations were typically required to get an acceptably low value of χ^2. At the end of each iteration, any negative values in $\mathbf{f}^{(n)}$ are clipped to zero. This was found to have a major influence on the convergence of the routine.

Some general characteristics of the MEM algorithm are noteworthy (refer to Figure 4.14 for a block diagram of the process). The original image $\mathbf{f}$, the imaging system $\mathbf{H}$, and the noise component $\mathbf{n}$ are all hidden from the observer. The observer only has the corrupted image $\mathbf{g}$, and an estimate $\hat{\mathbf{H}}$ of the true system point spread function $\mathbf{H}$. The noise process is assumed to be additive white noise. The MEM routine starts out by estimating the original image as a constant, which has maximal entropy. Since the uncorrupted image is unavailable for comparison, the estimate is blurred by the estimated PSF and compared in a least-squares fashion to the observed image $\mathbf{g}$. This first comparison has a high gray level mismatch (χ^2) for all but the trivial case of a constant original image. Each subsequent estimate from the Newton-Raphson iteration decreases the entropy of $\hat{\mathbf{f}}$, but makes the blurred estimate agree more and more with the original measurement data. The solution converges on an image that provides the best compromise between maximal entropy and minimum chi-squared. The algorithm favors estimates with smooth gray level transitions since this maximizes entropy. Suppose there were two estimates to choose from, one with

abrupt gray level changes and the other with more gradual changes. The blurred versions of these images do not have a significantly different chi-squared value, yet the sharper image has lower entropy. Thus, the algorithm chooses the smoother image. Consequently, the final result of MEM does not have the "crispness" associated with an inverse filtered image, but it also does not blow up the noise like an inverse filter.

The capability of MEM to improve resolution of the real-time image was assessed by processing the image of a resolution gauge and comparing the input/output image pair based on visual and quantitative means. Quantitative comparison was made by comparing slice profiles across the gauge elements and examining the increase in spectral response of the fundamental frequency.

The resolution gauge is a square-wave pattern of alternating X-ray opaque and X-ray transparent regions increasing continuously in frequency from 1 to 10 lp/mm. The gauge was placed in contact with the input screen of the image intensifier and was digitized using the same experimental setup used to measure the PSF. A 256×256 subimage was extracted for restoration and is shown in Figure 4.15. The blurring of the image intensifier is evident in the letters, tic marks, and square-wave pattern, which is visible to about 1.5 lp/mm. This image was processed using 20 iterations and the result is indicated in Fig 4.16. The blurring has been reduced since the contrast of the gauge pattern is higher and the lettering is easier to read.

The improvement in contrast was assessed quantitatively by first examining slice profiles across the square-wave pattern at 1.0 lp/mm (Figure 4.17) and at 1.5 lp/mm (Figure 4.18). The output slice is offset in these plots to facilitate comparison. At 1.0 lp/mm the contrast increased by a factor of 3 and the regularity of the square-wave

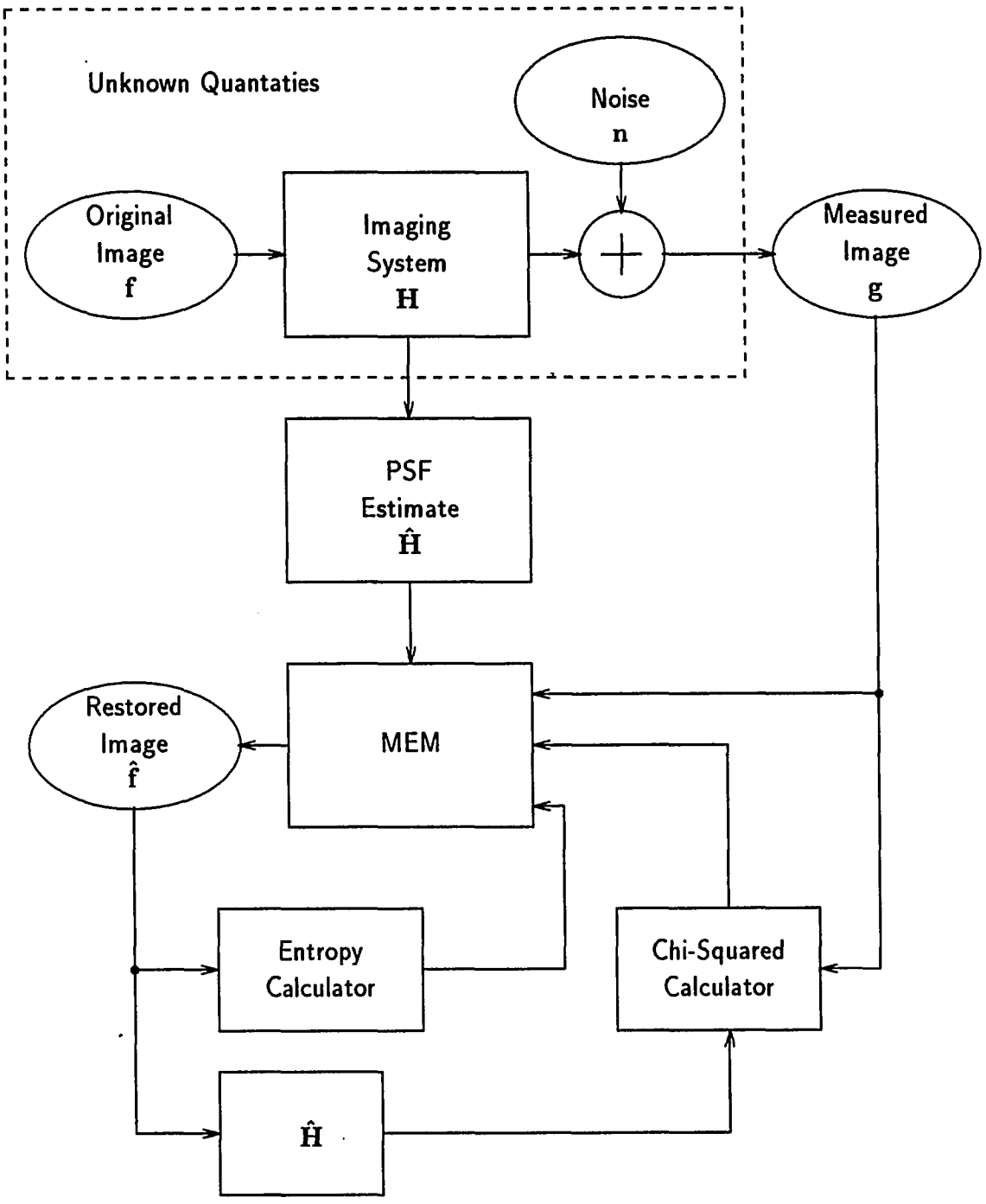

Figure 4.14: Flow diagram of the MEM restoration process

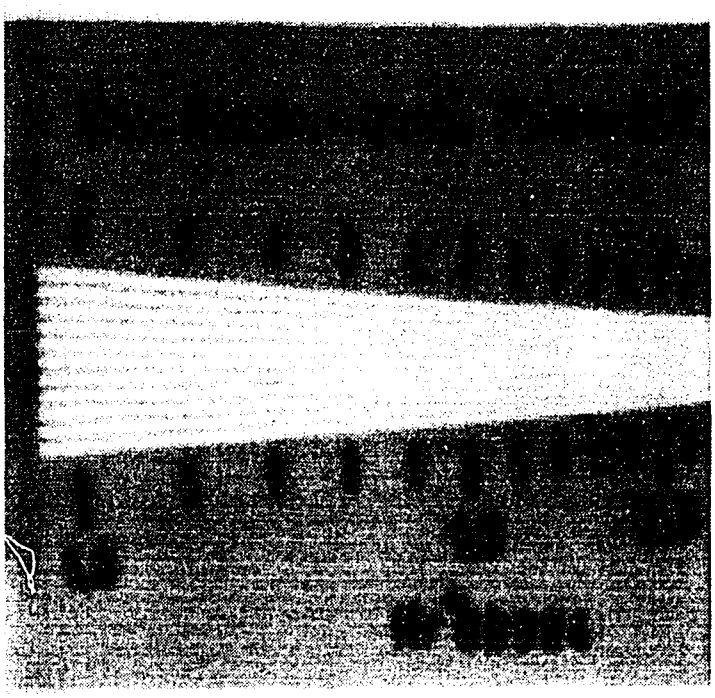

Figure 4.15: Resolution gauge image before MEM processing

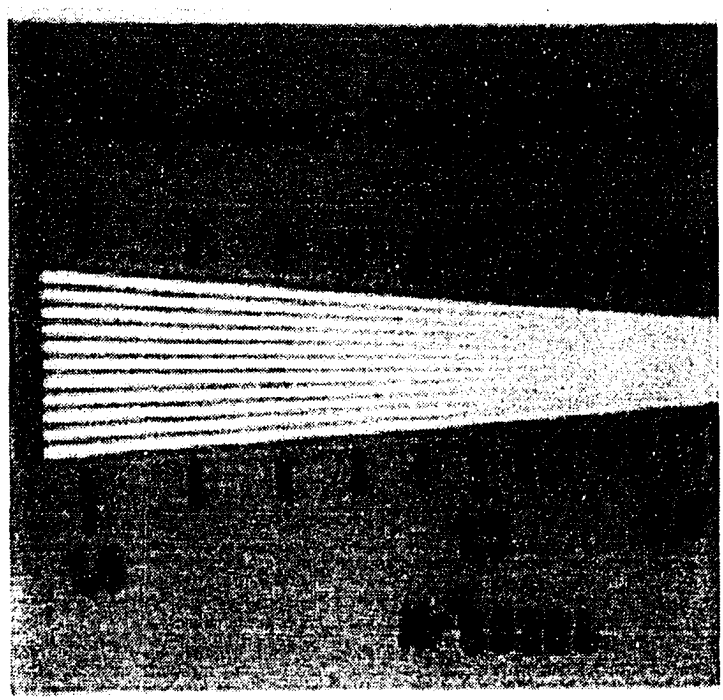

Figure 4.16: Resolution gauge image after MEM processing

signal was improved. At 1.5 lp/mm the contrast improvement was not as significant, but the regularity of the pattern was still improved. MEM smoothed the noise, and did not generate significant artifacts.

Improvement in contrast was also investigated by examining the spectral content of each row slice for the original and processed images. A Hanning window was applied in the spatial domain to isolate the square-wave pattern. The Hanning window was selected instead of a rectangular window to minimize sidelobes in the frequency domain. This 256 sample record was zero padded to 1024 samples and the 1-D FFT was computed. The amplitude of the fundamental frequency was used as a measure of contrast. Figure 4.19 shows a plot of amplitude versus frequency for the input and output images. The amplitude was referenced to 0 dB for the input image at 1.0 lp/mm. The MEM processed image had a gain of +8 dB in contrast at 1 lp/mm, a +4 dB gain at 1.5 lp/mm, and broke even at approximately 1.7 lp/mm.

A radiograph was also made of the resolution gauge. The square-wave pattern on the radiograph was visible to 10 lp/mm. This radiograph was digitized using the same sampling frequency and dynamic range as the real-time image of the resolution gauge. Its digitized resolution was limited to 1.8 lp/mm. The amplitude of the square-wave pattern for both images at 1.0 lp/mm was 30 gray levels, or 12% of the dynamic range of the 8-bit digitizer. The square-wave amplitude was closer to 80% of the dynamic range at 1.0 lp/mm when the resolution gauge was imaged directly by the video camera. In this image, the square-wave pattern was visible to nearly 10 lp/mm, although aliasing was clearly evident after the folding frequency of 3 lp/mm. This suggests that much of the loss of resolution in the real-time image used for this analysis was due to an insufficient number of gray levels to sample the

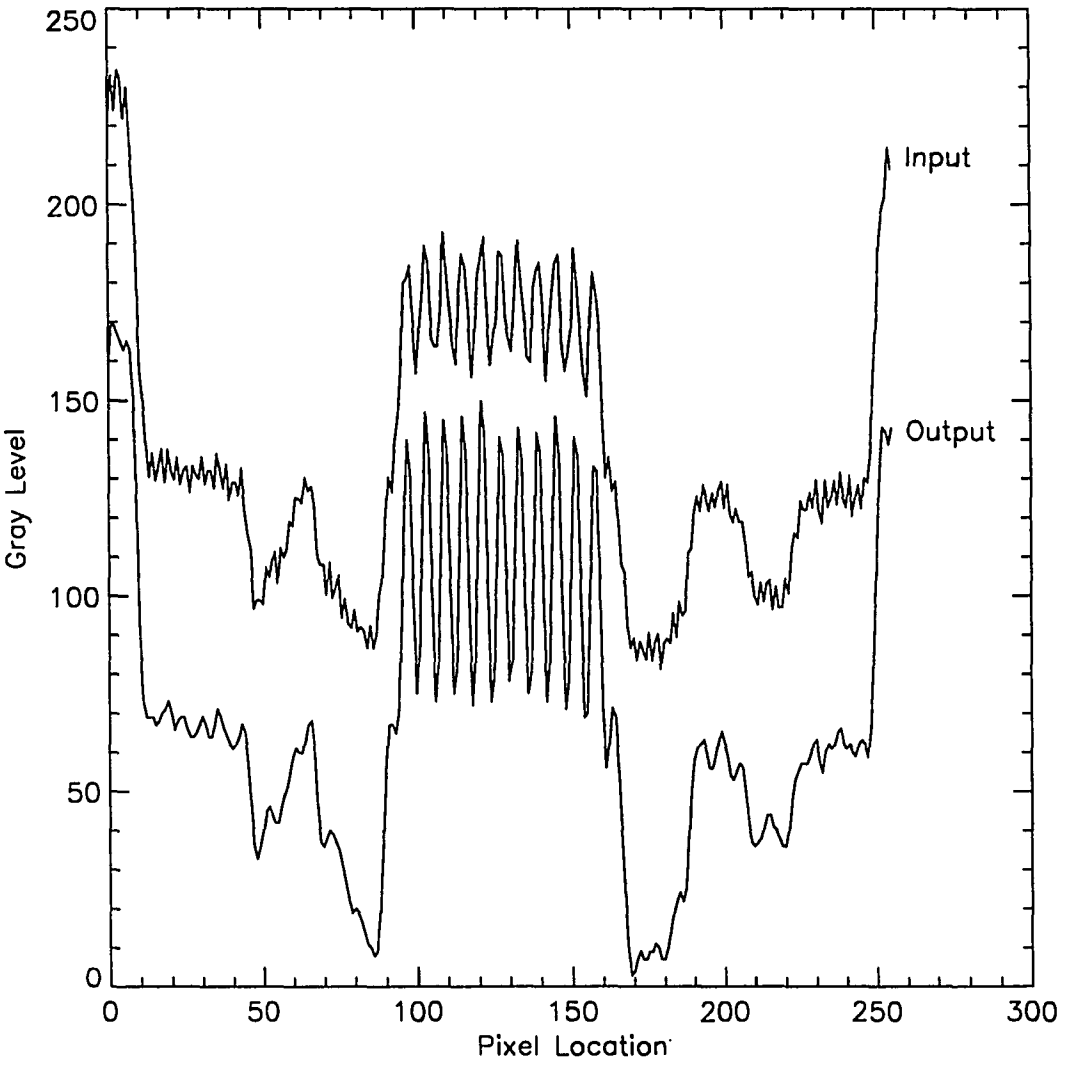

Figure 4.17: Input and MEM processed slice profiles at 1.0 lp/mm

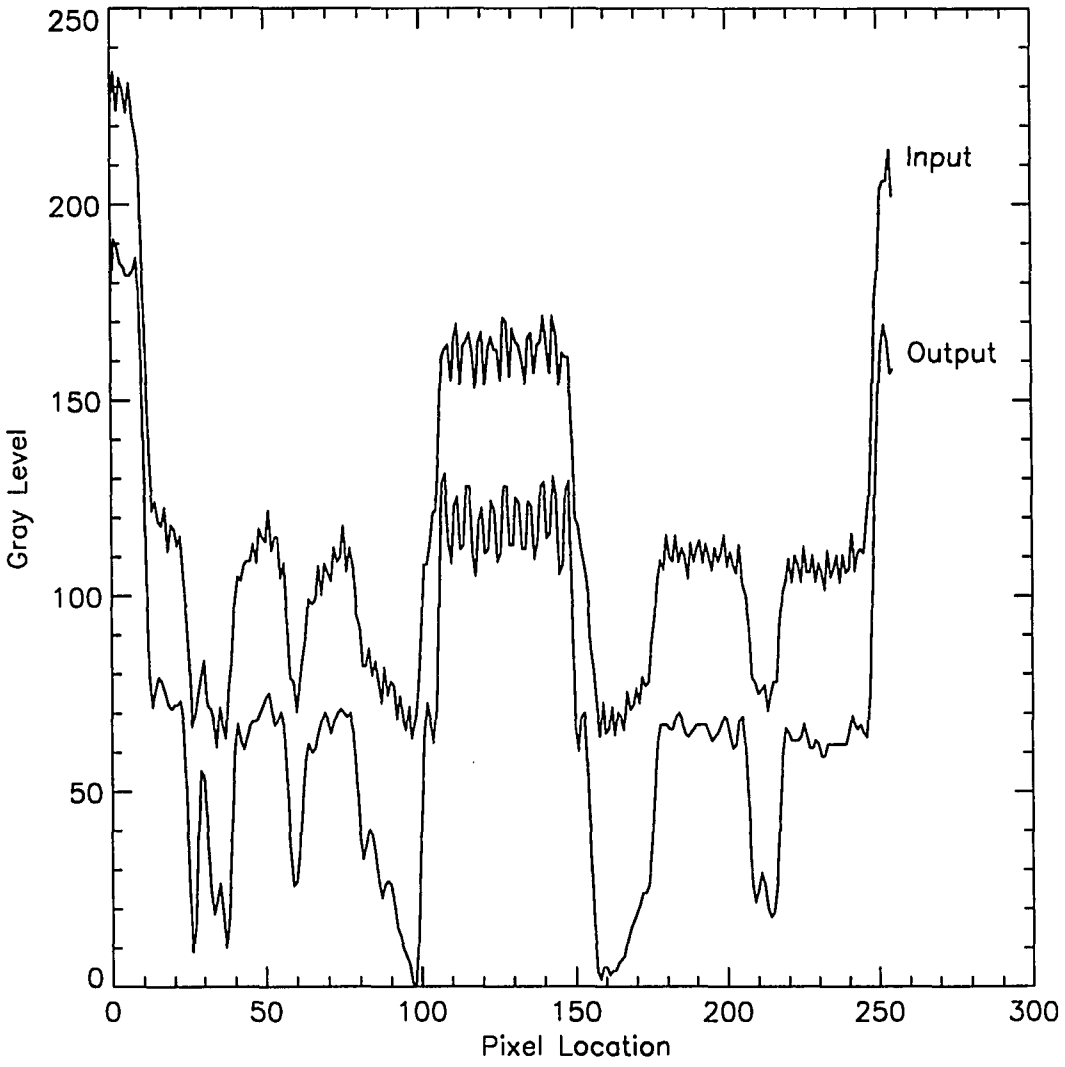

Figure 4.18: Input and MEM processed slice profiles at 1.5 lp/mm

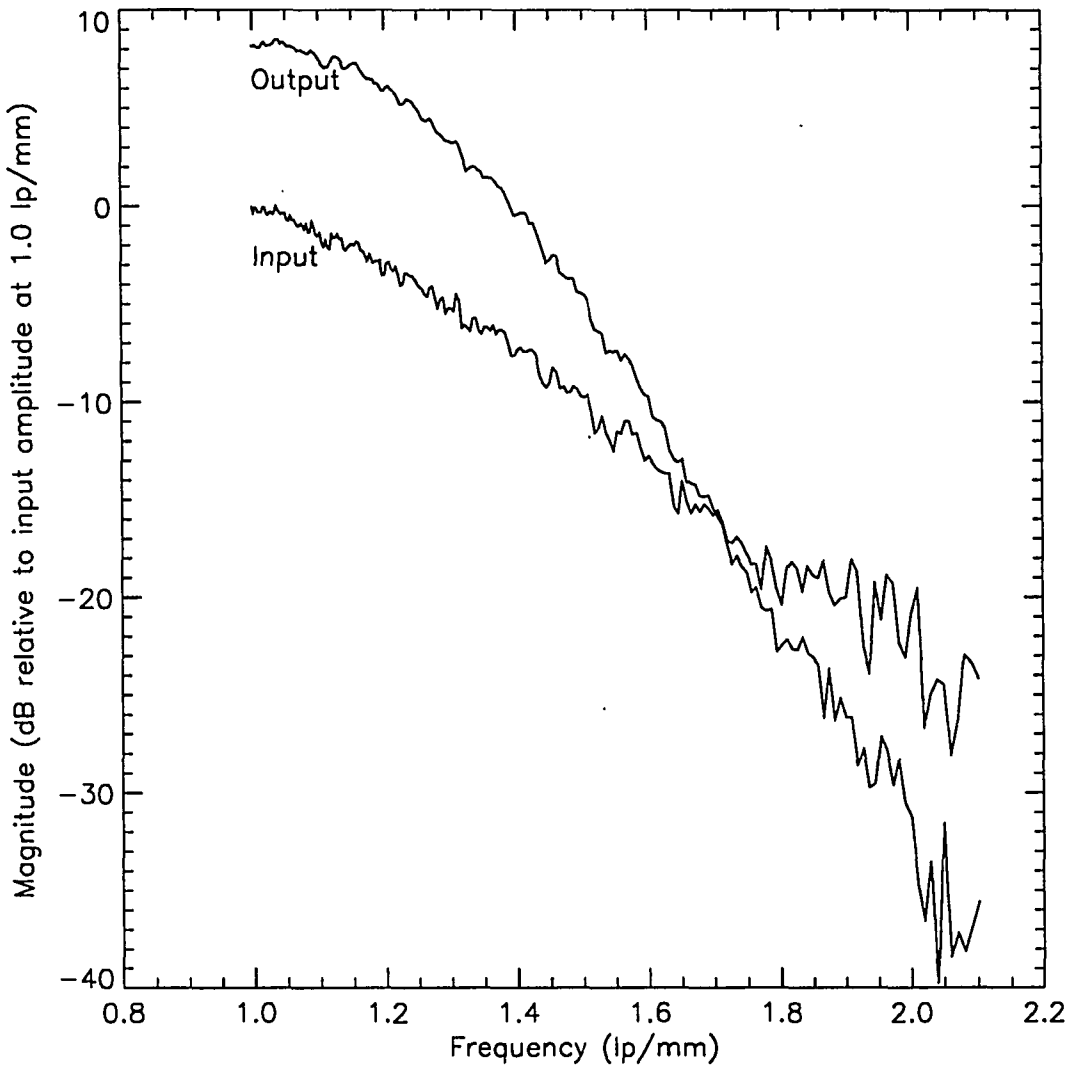

Figure 4.19: Improvement in frequency response due to MEM

square-wave pattern. Thus, *the success of the MEM restoration at higher frequencies was limited by loss of information in the input image.*

The maximum entropy method has been found to improve the resolution of a real-time radiography system by deconvolving the system point spread function. The PSF was measured using a high resolution edge scan followed by numerical differentiation. A Gaussian model was found to fit this data satisfactorily, and was subsequently used as the PSF to be deconvolved by MEM. The MEM image was estimated using a multivariate Newton-Raphson technique. MEM was applied to the image of a resolution gauge, and was found to increase the contrast of the resolution gauge over the visible range of the digitized image by as much as 8 dB. Furthermore, MEM smoothed the image noise, restored the square-wave pattern, and did not generate significant artifacts. This particular MEM implementation is computationally efficient, especially when a hardware accelerator is available to perform the 2-D FFTs.

The relatively low resolution of the digitized resolution gauge radiograph indicated that the video camera and digitizer setup were significant in limiting the potential increase in resolution from MEM restoration. The performance of the real-time detector from the input of the X-ray field to the digital image is no better than the poorest performing device in the imaging chain. Link *et al.* (1989) characterized a system using an image intensifier with 4.4 lp/mm resolution and a video camera with 625 TV lines of resolution. The overall system response was 1.8 lp/mm. The system at hand is quite similar, with 4 lp/mm specified for the image intensifier, and a CCD video camera with 512 TV lines. The sampling frequency of this system was 6 pixels/mm, resulting in a folding frequency of 3 lp/mm. The resolution gauge response fell off rapidly after 1.7 lp/mm, so the findings of Link *et al.* are confirmed.

Thus, the video camera was the limiting factor for resolution in this system. Using a higher resolution digitizer would allow the PSF of the image intensifier to be determined more accurately.

These techniques were evaluated in detail for the case of a resolution gauge object. Their contribution to improving the accuracy of the overall 3-D measurement system will be discussed in Chapter 5.

CHAPTER 5. EXPERIMENTAL PROCEDURES AND RESULTS

This chapter uses the 3-D measurement system in a variety of scenarios and using different materials and geometries. The experiments progress from simple to complex. The first sample is an aluminum cylinder with a single drilled hole, and the second sample is an aluminum plate with copper wires embedded at different depths. These samples are used to test the system's ability to properly locate and size features of interest. A turbine blade is used for the third sample as an example of a dimensional analysis problem. The fourth and final sample is an automobile air conditioner part containing shrinkage porosity; this example demonstrates a crack sizing and orienting problem for a real part.

The first section details the practical aspects of system setup required for accurate reconstruction results. The remaining sections describe results obtained by making 3-D measurements on two fabricated and two actual samples.

Laboratory Setup

The X-ray source, positioner, and detector all need to be properly aligned. The XY plane is placed at the protective plate of the image intensifier. While the actual conversion screen tangent plane is located 4 mm behind this plane, the sampling frequencies and image warp coefficients are selected to yield correct measurements in

the XY plane. The objective of the laboratory calibration is to determine the 3-D coordinates of the X-ray source and sample position center of rotation with respect to the global coordinate system (X_g, Y_g, Z_g). The center of rotation defines the local coordinate system for the sample (X_s, Y_s, Z_s). The 3-D measurement software reports results in both coordinate systems, although the local coordinate system is used to display data in this chapter.

X-ray source position

The objective of this calibration is to determine the 3-D coordinates of the X-ray source S in a global coordinate system centered at the detector plane. The center of the image intensifer is selected as the origin and a mark is affixed to this position (denoted D). The Z-axis translation of the sample positioner is taken as the global coordinate system Z-axis. Now, the X-ray source is considered to be at some arbitrary location in the positive Z direction. This situation is depicted in Figure 5.1. A sharp point, or other easily identified feature, is attached to the center of the sample positioner; this is the origin of the local coordinate system for the sample, and is denoted P. The X-ray source is activated, the X-ray image is viewed, and the sample positioner translational axes are adjusted to make the image of point P coincident with the detector point D. In addition, P is located as close to the detector as possible. This first step is indicated by the circled number in Figure 5.1. Next, the Z coordinate of the positioner point P is increased in Step 2. The image of P will wander away from the image of D except when S is perfectly lined up on the Z-axis. P is moved as close as possible to the source S. In Step 3, the X position of the sample positioner is manipulated to bring P back in coincidence with D. In Step 4

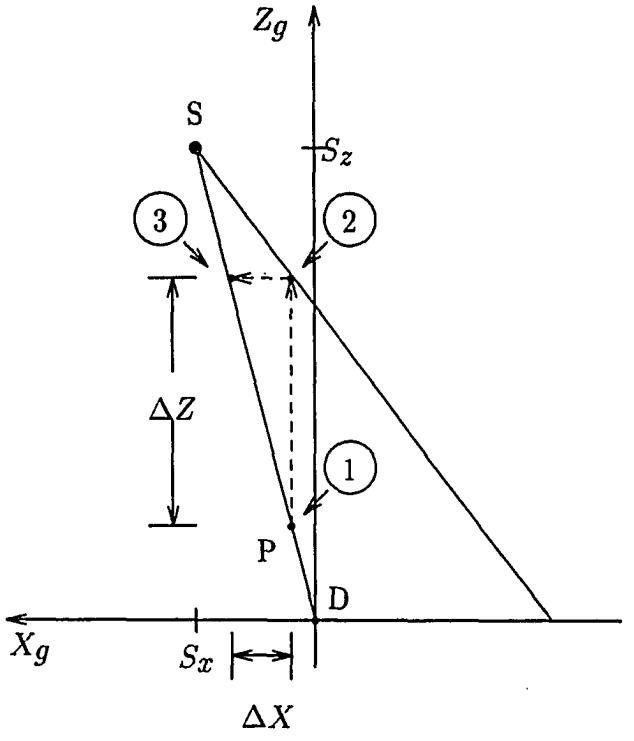

Figure 5.1: Determining the 3-D X-ray source position

(not indicated on the diagram), the Y position of P is also adjusted to make P and D coincident. The total change in position of P from the beginning of the procedure is recorded as ΔX, ΔY, and ΔZ.

The Z position of the source S_z is determined using a tape measure. The remaining quantities are determined as

$$\begin{aligned} S_x &= S_z(\Delta X/\Delta Z) \\ S_y &= S_z(\Delta Y/\Delta Z) \end{aligned} \tag{5.1}$$

Sample coordinate system position

The point P identifying the origin of the sample coordinate system is moved to the desired Z position. This distance P_z is measured with a tape measure. The position of P is manipulated to make its image again coincident with the image of the detector point D. The remaining coordinates are subsequently determined as

$$\begin{aligned} P_x &= P_z(\Delta X/\Delta Z) \\ P_y &= P_z(\Delta Y/\Delta Z) \end{aligned} \tag{5.2}$$

These values are stored in the laboratory geometry file used by the 3-D measurement system.

Experiment 1: Cylinder With Drilled Hole

The object used for this experiment is a 1" diameter aluminum cylinder with a single 0.2 cm diameter hole drilled near the edge of the cylinder and parallel to the cylinder axis. A schematic diagram of this sample is shown in Figure 5.2. Two thin lead markers were attached to the periphery of the cylinder. The objective of

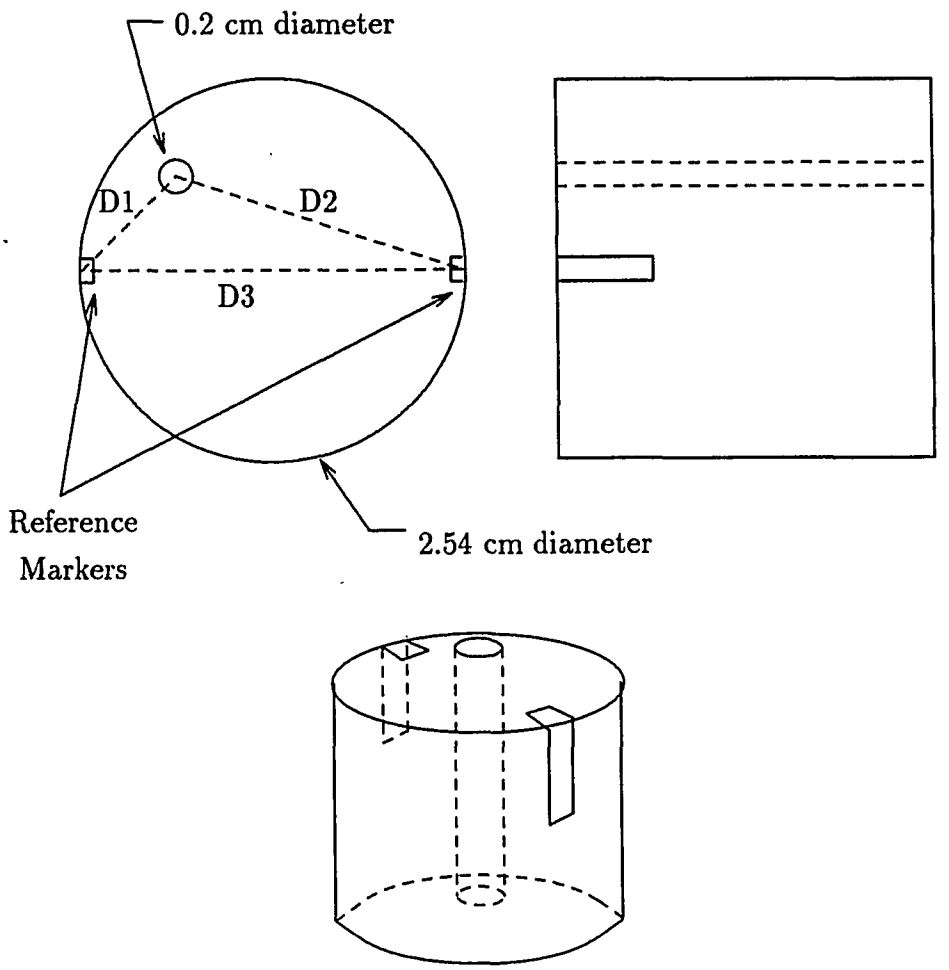

Figure 5.2: Schematic diagram of aluminum cylinder sample

this experiment was to determine the position of the central axis of the drilled hole relative to the two external markers. The position was determined by measuring the distances D_1, D_2, and D_3 as indicated in Figure 5.2.

Since the hole was drilled completely through the sample, the circular face of the cylinder was used as a comparative reference. The tips of the lead markers were folded over onto the circular face to be made visible to a CCD camera which digitized the face to a 640×480 image. The horizontal and vertical sampling frequencies were determined by including a millimeter scale in the image; they were 178.5 pixels/cm and 170.9 pixels/cm, respectively. The distances determined from this image were D_1=1.19 cm, D_2=1.84 cm, and D_1=2.53 cm.

The cylinder was placed on the sample positioner with its central axis aligned with the center of rotation of the sample positioner stage, and with its face containing the lead markers in contact with the platter. The detector-side marker was made slightly longer than the source-side marker to make them distinguishable. The X-ray source position was $(0.00 \pm 0.2, 0.00 \pm 0.2, 123.8 \pm 0.2)$ cm and it was operated at 100 KV and 600 μA. The origin of the sample's local coordinate system was $(0.00 \pm 0.2, 0.00 \pm 0.2, 91.4 \pm 0.2)$ cm, resulting in a magnification factor of 3.82.

Figure 5.3 shows a picture of the real-time image of the sample oriented at $\theta = 0^{\circ}$. The best way to interpret the image is to imagine yourself at the source position looking through sample. This way, the $X_g Y_g$ plane falls with its origin in the center of the image, with the X_g axis increasing towards the right and the Y_g axis increasing towards the top of the image.

The lead markers correspond to the dark strips in the center of the image (they overlap in this view), and the light strip to the left of the markers corresponds to the

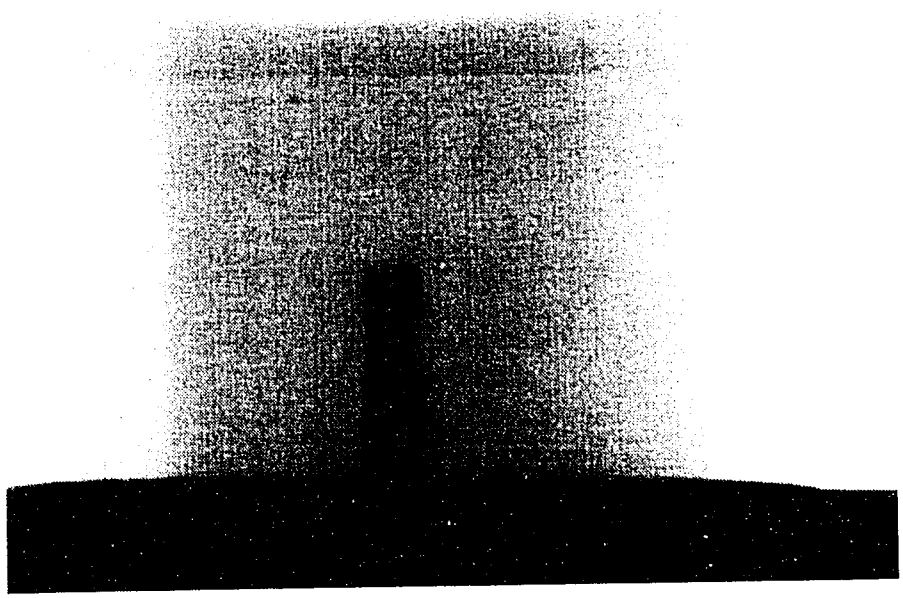

Figure 5.3: Real-time image of aluminum cylinder, $\theta = 0^{\circ}$

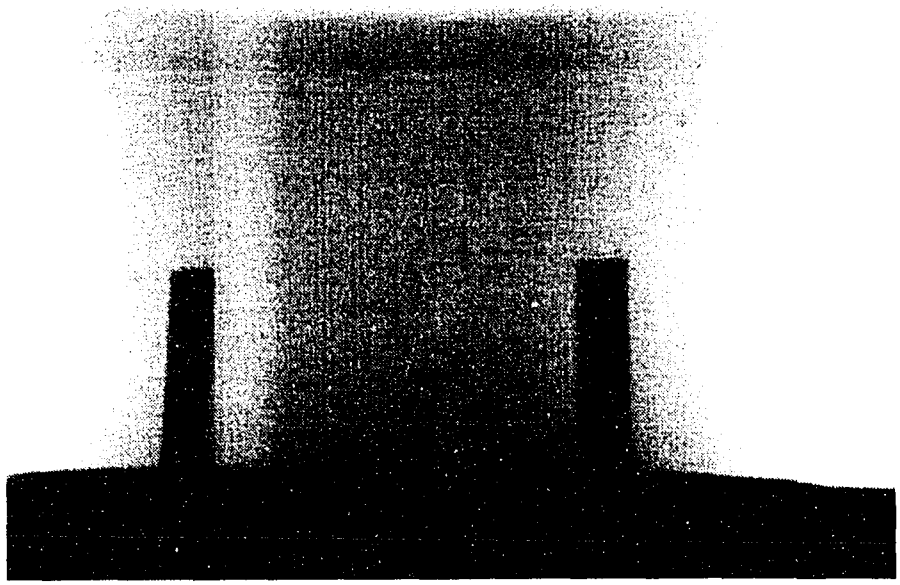

Figure 5.4: Real-time image of aluminum cylinder, $\theta = -30^{\circ}$

drilled hole. The real-time image is a "positive" in contrast to an image obtained with radiographic film: thinner or less dense portions of the sample have relatively higher intensity in the real-time image. The vertical edges of the cylinder present a thinner cross-section to the X-ray beam, which caused the detector to saturate. Consequently, these edges were not imaged as clearly.

Figure 5.4 shows an image of the sample after being rotated -30° about the Y_S axis. The image of the longer (detector-side) marker moved to the right, while the shorter (source-side) marker moved to the left. The image of the hole translated to the right, indicating that it was located closer to the detector than to the source in the initial view.

Table 5.1: Measurement results for cylindrical sample

Test	Number of Views	Error		
		D1 (cm)	D2 (cm)	D3 (cm)
1	2 ($\theta = 0^\circ, +30^\circ$)	+0.00	+0.04	+0.02
2	2 ($\theta = 0^\circ, -30^\circ$)	+0.00	+0.03	+0.02
3	2 ($X = -0.1'', +0.5''$)	+0.38	−0.34	+0.06
4	3 ($X = 0.0'', -0.1'', +0.5''$)	+0.36	−0.25	+0.13
5	2 ($\theta = 0^\circ, +30^\circ$)	+0.02	+0.01	+0.02
6	2 ($\theta = 0^\circ, +30^\circ$)	+0.02	+0.00	+0.01
7	2 ($\theta = 0^\circ, +30^\circ$)	+0.01	+0.03	+0.03
8	2 ($\theta = 0^\circ, +30^\circ$)	−0.01	+0.04	+0.02
9	5 ($\theta = 0^\circ, -30^\circ, -60^\circ, -120^\circ, -150^\circ$)	+0.00	+0.03	+0.02

For the 3-D measurements, the images of the tips of the lead markers were used as Points 1 and 2, and Point 3 was selected as the center of the hole image on the same row as the lead marker tips. Table 5.1 summarizes the 3-D measurement results obtained for this sample. The error was computed by subtracting the reference distance (obtained from the optical image) from the RTR measured distance.

All tests except Tests 3 and 4 had similar errors. Tests 5–8 repeated the measurement of Test 1. The mean values of these five measurements were D_1=1.20 cm, D_2=1.86 cm, and D_3=2.55 cm. The means were biased by 0.01 to 0.02 cm compared to the optical reference. The standard deviations for D_1, D_2, and D_3 were 0.01 cm, 0.02 cm, and 0.01 cm, respectively. Test 9 was made using five views, and still had some positive bias. These error values are consistent with the simulator-predicted values of Chapter 3.

Tests 3 and 4 used a horizontal translation of 0.6". The error was a factor of

10 larger for the distances D_1 and D_2. The Z components of the measured 3-D coordinates of the lead markers were off by 0.6 cm compared to the other tests, and the Z component of the drilled hole axis was off by 0.2 cm. This problem was examined by looking at the condition number of the $\mathbf{X}$ matrix (the ratio of the largest to smallest singular value). The singular values for the rotation experiment of Test 1 were 43.75, 169.5, and 175.1, resulting in a condition number of 4.00. The singular values for the translation experiment of Test 3 were 3.26, 175.1, and 175.1, resulting in a condition number of 53.8. The sensitivity to measurement error of the least-squares result is proportional to the square of the condition number, and since the squared condition number of Test 3 is 180 times larger than that of Test 1, the small translation amount used in Test 3 and 4 yielded an ill-conditioned matrix with respect to least-squares solution. This large error was predicted earlier by the translation-only simulation for a 4× configuration.

A two-view rotation measurement was made to confirm the validity of the simulation results of Chapter 3. The first view was always made at 0°. The second view was obtained by rotating the sample in multiples of 2°. So, for example, the first measurement was obtained using views at 0° and 2°, the second at 0° and 4°, and so on up to 0° and 36°. The difference in measured depth (Z coordinate) from the final value for each of the three points is plotted using solid lines in Figure 5.5. This experiment was performed using the following laboratory conditions: $\mathbf{s} = [2.03\ 1.27\ 81.0]^T$ cm, $\mathbf{c} = [1.40\ 0.88\ 55.9]^T$ cm (magnification = 3.22), and the X-ray source was operated at 90 KV and 300 μA. Point 1 is the lead marker on the source side, Point 2 is the lead marker on the detector side, and Point 3 is the central axis of the drilled hole. The condition number of the least-squares solution for

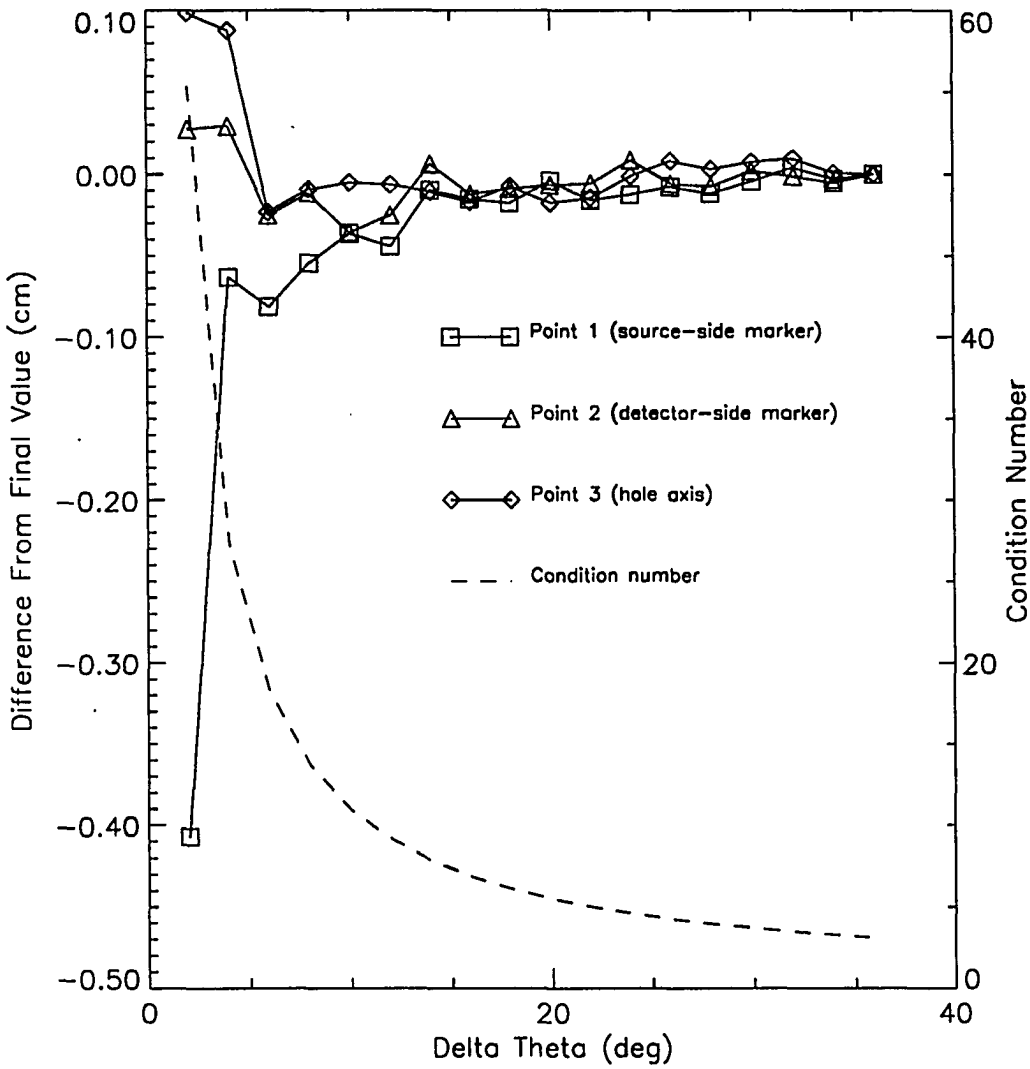

Figure 5.5: Measurement error as a function of rotation angle for 2-view experiment

Point 1 is plotted as the dashed line (the condition numbers for the remaining points were essentially the same). Note that the measurement stabilized once the change in rotation between the two views exceeded 15°. This point corresponded to a condition number approximately equal to 5. The standard deviation of the measurements in the range 15° to 30° was 0.005 cm, 0.007 cm, and 0.01 cm for Points 1, 2, and 3, respectively. Bias was investigated by recalculating these points using an error in the source location of +0.5 cm and −0.5 cm. The new points for a source position error of +0.5 cm had a bias of approximately +0.01 cm; a bias of about −0.01 cm was observed in the computed depth using a source position error of −0.5 cm. This supports the conclusion that measurement bias is due to the X-ray source/detector geometry and random variation is due to point selection on the display.

The previous two-view test was repeated using a magnification of 1.46 by moving the center of rotation to 25.4 cm (Figure 5.6). The errors are higher than the previous test; in the range 15–30°, the standard deviations of the depth measurements were 0.009 cm, 0.019 cm, and 0.018 cm, respectively, for Points 1, 2, and 3. This is to be expected since lower magnification effectively reduces the resolution of the detector. However, the depth measurements stabilized after a rotation of 20°, which indicates that good results can still be obtained at lower magnification values.

The variance of point selection from the display screen is the source of the random errors. The amount of variance was determined experimentally using the image of Figure 5.3. Four different features (labeled A–D) were selected within this image: Feature A is the top of the lead marker, Feature B is a small low-contrast blob, Feature C is some arbitrary point located along the center axis of the drilled hole, and Feature D is the top of the drilled hole. A 16×16 pixel cross-shaped cursor was

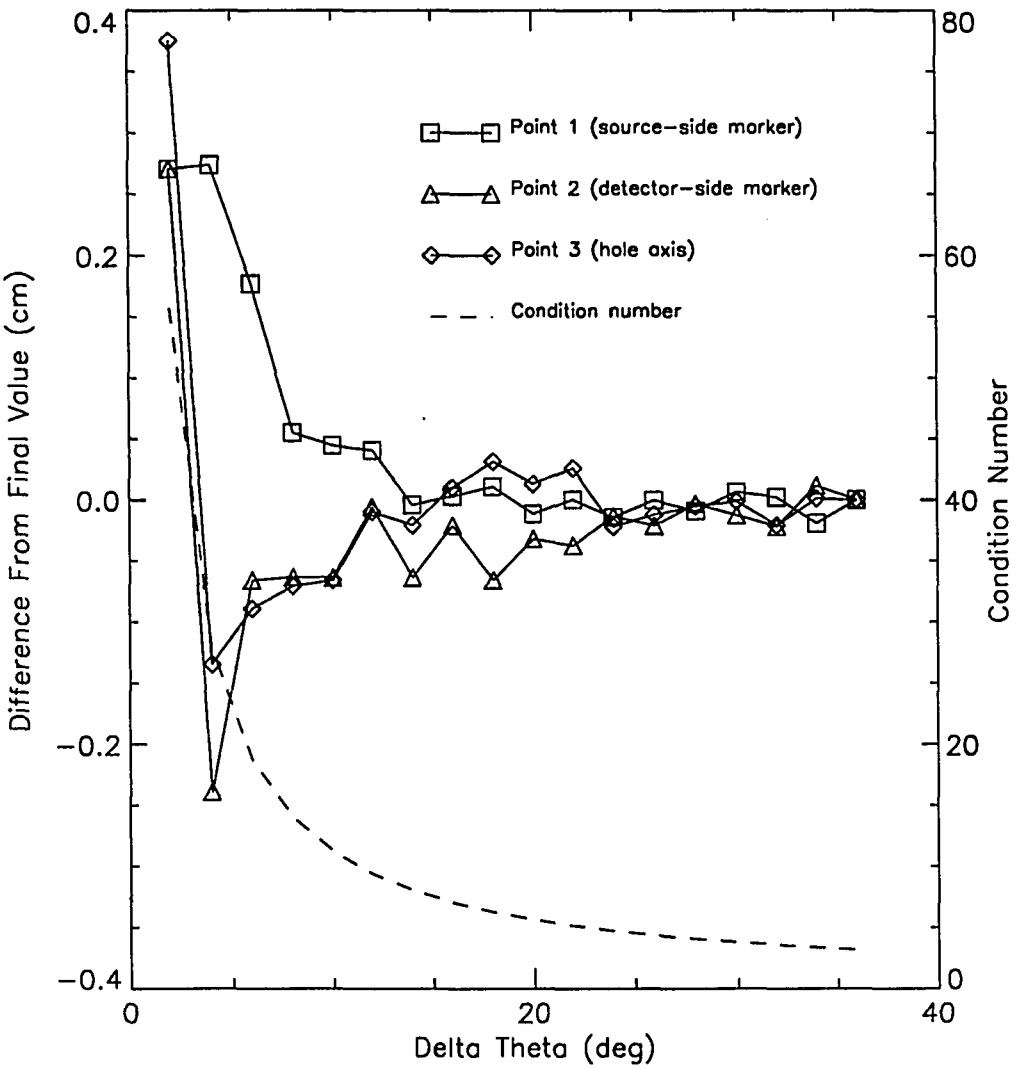

Figure 5.6: Measurement error as a function of rotation angle for 2-view experiment (1.46× magnification)

Table 5.2: Variance of operator-determined screen coordinates

Feature	Standard Deviation of Position	
	Horizontal (pixels)	Vertical (pixels)
A	0.47	0.23
B	0.56	0.50
C	0.69	2.54
D	0.82	0.52

used. The operator was prompted to select the same feature 20 times. The cursor position was reset to the center of the image between each measurement. Table 5.2 indicates the standard deviations for these four tests.

Feature A is a rectangular shape with a sharp horizontal edge of approximately the same width as the cursor. The variance in selecting the vertical position of this edge was quite low (0.23 pixels) since the edge is well-defined. There was a little more ambiguity in selecting the center of the edge since the operator had to judge where the center was located. This is reflected in a higher variance (0.47 pixels). Determining the center was still relatively easy since the cursor size matched the size of the feature.

Feature B is a low contrast circular blob the same size as the cursor. The standard deviation was about 0.5 pixels in both the horizontal and vertical directions. This makes sense since the operator's judgement of the center of the blob is similar for both directions.

In the third experiment, the operator was required to measure the central axis of the drilled hole by choosing an arbitrary location. The operator attempted to measure the same point each time (as opposed to picking any vertical location along

the hole). The standard deviation of the vertical position increased nearly five times to 2.54 pixels, while the standard deviation of the horizontal position increased only slightly to 0.69 pixels. The drilled hole feature was about 3 times wider than the cursor, so this caused more ambiguity in determining the center. It should be noted that selecting the edges of the hole and computing the average value would be a more accurate way of determining the central axis. As a result of these experiments, the mouse control was modified so the user could constrain the mouse motion to a single axis (horizontal or vertical), determine the edge locations, and type in the average value.

Feature D is similar to Feature A, except it is larger and less defined. This is reflected in the increased standard deviation of the results compared to Feature A. Overall, the typical variance of selecting a feature point from the screen was in the range 0.5–0.8 pixels.

This experiment showed how the position of a feature, in this case the central axis of a drilled hole, could be determined relative to external markers affixed to the sample. The distances between the hole and the markers were measured using an independent technique (CCD video camera image of the cylinder face), and the error between these two measurements ranged between −0.01 to +0.04 cm for a two-view rotation experiment of 30°. Five repetitions of the same rotation-based measurement indicated the length measurements were biased by 0.01–0.02 cm and had a standard deviation of 0.01–0.02 cm. These values are comparable to the resolution of a commercial CT image of 0.01 cm/pixel (Martz *et al.*, 1990). The axial symmetry of this sample permits a good CT scan (no problems with partial data reconstructions), so either technique could be used to make this type of measurement. The CT-based

measurement does not require external markers to identify the surface, but the cost of the RTR-based measurement is less by an order of magnitude.

It was determined that translation-only measurements had ten times as much error compared to the rotation-only measurements; this confirmed the validity of the simulation results presented in Chapter 3. This cylinder had axial symmetry, so rotating it closer to 90° would improve the reliability of the measurement.

Experiment 2: Aluminum Plate With Embedded Copper Wires

The object used for this experiment is an aluminum plate with copper wires embedded at different depths. Figure 5.7 shows an exploded view schematic of this plate. The plate is composed of four 5"×5" aluminum plates of thicknesses 13 mm, 1 mm, 2 mm, and 6 mm. Four 0.01" diameter copper wires of lengths 12 mm, 6 mm, 14 mm, and 4 mm were used to simulate crack defects. The vertices of the wires are used as the range points, and are numbered 1–10 in Figure 5.7. The objectives of the experiment are: (1) to measure the length of the wires, (2) to determine the 3-D orientation of the endpoints of the wires, and (3) to determine the ability to distinguish which layer contains a specific wire.

Before assembling the thin plates into a single plate, an optical image was made of each plate in the stack using a CCD camera. The XY coordinates of the wire endpoints were measured using the lower left corner of the plate as the origin. The depth (Z coordinate) of each level in the assembled plate was measured to 0.001" using calipers. Table 5.3 lists the three-dimensional coordinates of the wires. Using these coordinates, the lengths were computed; they are tabulated in Table 5.4. The total thickness of the plate was 2.23 cm.

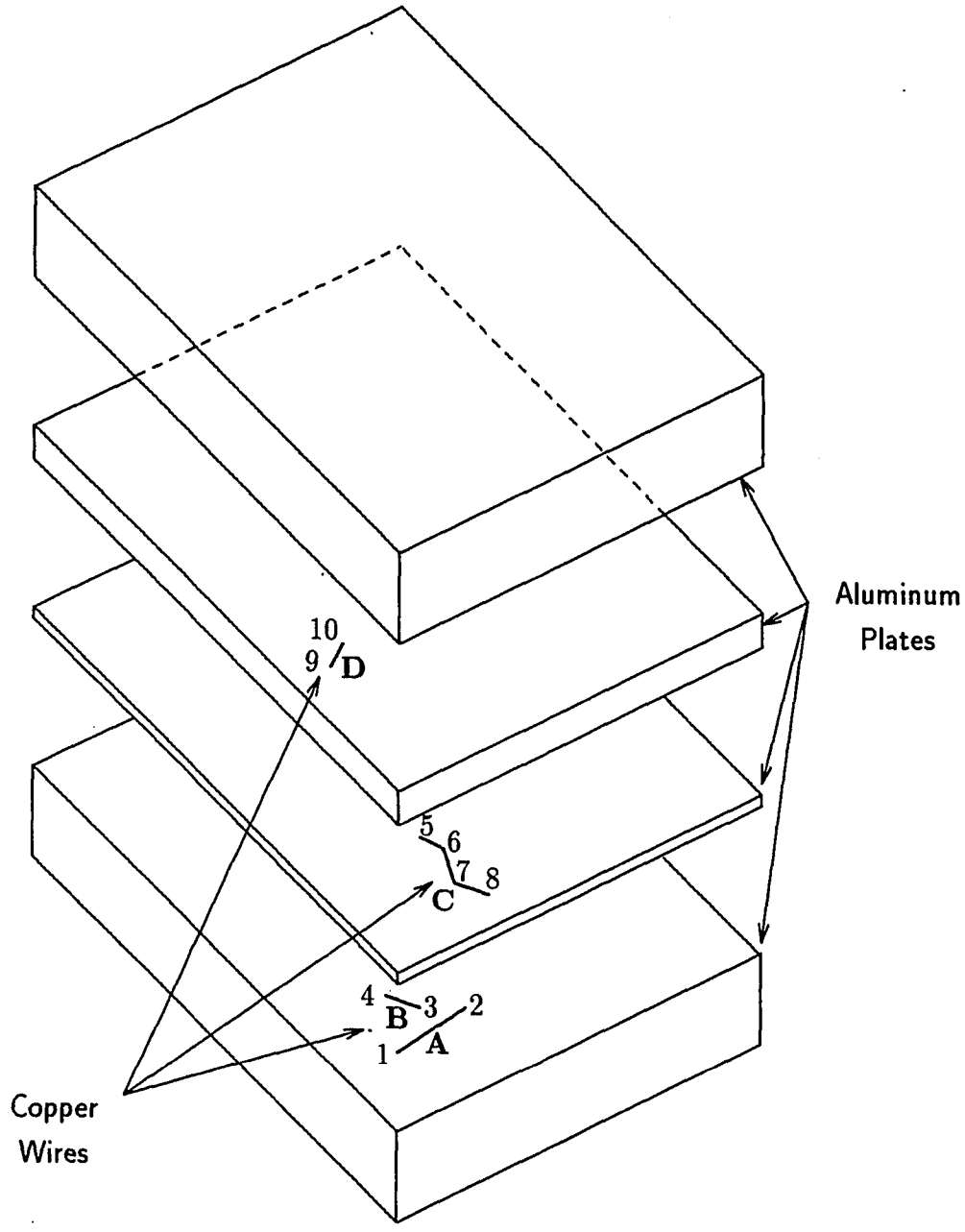

Figure 5.7: Schematic diagram of aluminum plate sample, with wires alphabetically labeled and vertices numerically labeled

Table 5.3: Optically measured coordinates of wire endpoints

Point	X (cm)	Y (cm)	Z (cm)
Wire A			
1	0.94	1.09	1.29
2	2.02	1.53	1.29
Wire B			
3	2.15	2.45	1.29
4	1.67	2.81	1.29
Wire C			
5	2.38	1.86	1.40
6	2.93	1.75	1.40
7	3.05	1.27	1.40
8	3.36	1.07	1.40
Wire D			
9	0.84	1.62	1.59
10	1.04	1.93	1.59

Table 5.4: Optically measured wire lengths using endpoint coordinates

Wire	Length (cm)
A	1.16
B	0.60
C	1.43
D	0.37

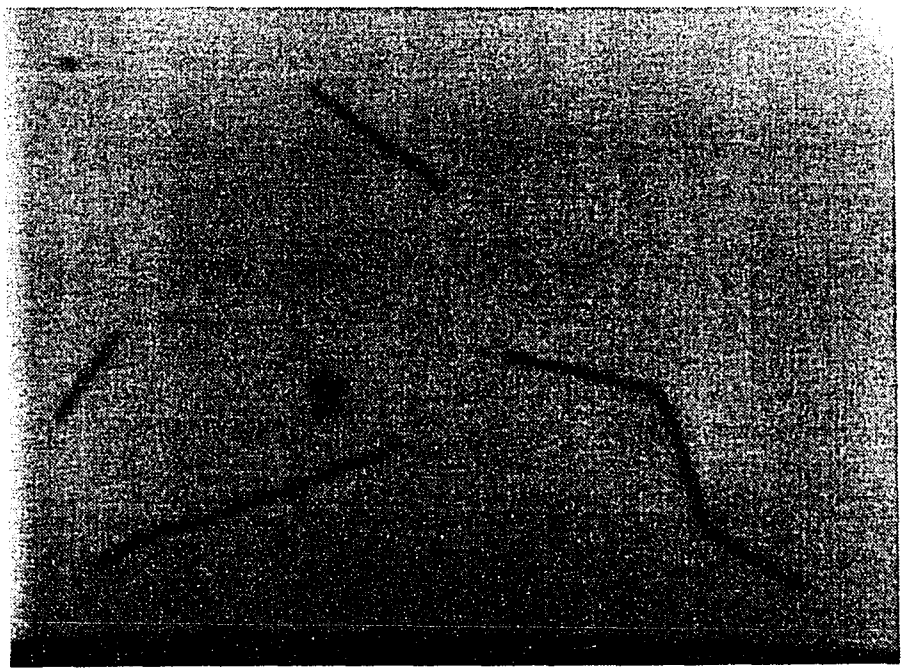

Figure 5.8: Real-time image of aluminum plate (0° rotation)

Figure 5.8 shows the real-time image of the plate oriented at 0°. The X-ray generator was operated at 90 KV and 800 μA. Two small lead markers were attached on either side of plate to indicate the plate boundaries. The marker on the detector side is denoted Point 11 and the marker on the source side is denoted Point 12. The angle of the plate was adjusted to make the images of the markers overlap, and the θ axis of the positioner control program was zeroed at that point. Real-time processing was used to divide a flat-field image from the live image. The ROI size was selected to process the entire image.

Figure 5.9 shows an image of the plate oriented at $+47^{\circ}$. The X-ray source was operated at the same voltage and current levels; the decrease in intensity is due to the

Figure 5.9: Real-time image of aluminum plate ($+47^{\circ}$ rotation)

increased effective thickness of the plate as a result of rotation. Rotation was limited to $\pm 40^{\circ}$ in order to detect all four wires in both views. A trend removal/contrast stretch was used for ROI processing to better see the wires in the rotated image. This processing was used to extend the wire visibility to $+60^{\circ}$; the wires became undetectable after 65–70° rotation without increasing the X-ray source current. Averaging at least 16 frames was necessary to maintain image quality in the rotated image since the reduced number of photons increased quantum mottle noise. Figure 5.10 shows the real-time image of the plate oriented at $+60^{\circ}$ with ROI-enhancement of Wire C. Note that quantum mottle noise obscured the wire endpoints. In addition, the fixed-pattern background noise of the CCD camera became more pronounced as a result of the contrast stretch operation. This noise appeared as a vertical pattern of lines.

Five data sets were acquired using a variety of angular changes. Figure 5.11 plots the first data set as three coordinate planes. Solid lines are drawn between related range points, and the dotted lines indicate the expected Z locations for the range points. Note that the wire depths are easily distinguished from each other.

The error in measured length is tabulated in Table 5.5. The last column of the table denoted "M" indicates the error in measuring the distance between the two lead markers on the plate surfaces. Seven views were acquired for Test 5 at angles 0°, $+10^{\circ}$, $+10^{\circ}$, $+20^{\circ}$, $+30^{\circ}$, $+40^{\circ}$, and -20°.

The length of Wire C was consistently under-measured compared to the other wires. This is likely due to the increased uncertainty in choosing the proper locations of the intermediate vertices compared to choosing the endpoints. Tests 3 and 4 used a smaller rotation angle, but still yielded good results. The measurement of the plate

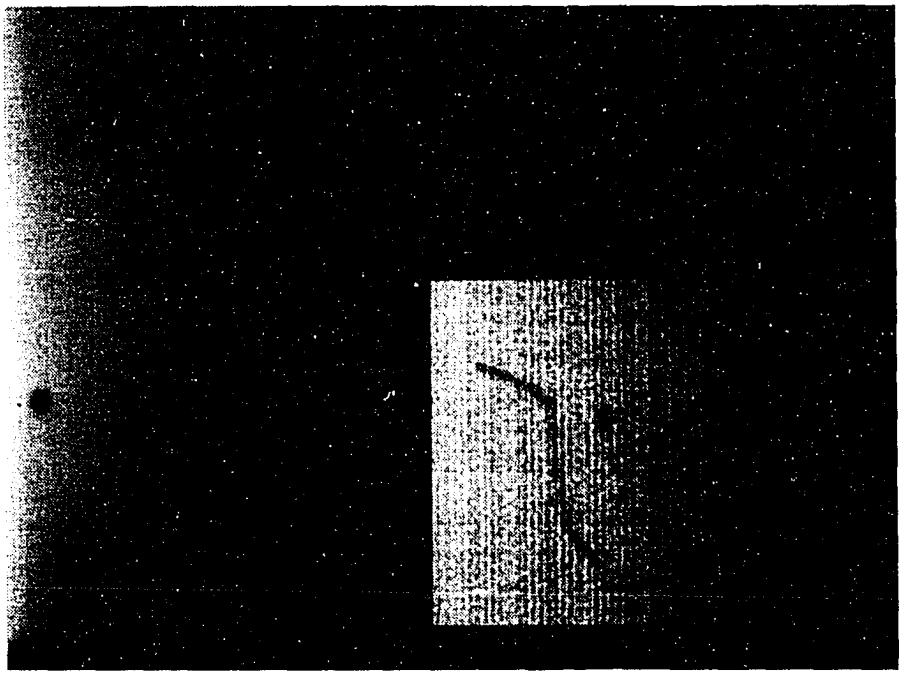

Figure 5.10: Real-time image of aluminum plate (+60° rotation) with contrast stretch in a region-of-interest

Table 5.5: Measurement results for aluminum plate

Test	Views	CN	Error				
			A (cm)	B (cm)	C (cm)	D (cm)	M (cm)
1	$\theta = 0°, +51°$	02.3	−0.02	−0.02	−0.05	−0.01	+0.01
2	$\theta = 0°, -47°$	02.5	−0.01	−0.01	−0.05	+0.00	+0.06
3	$\theta = 0°, +10°$	11.4	−0.02	−0.01	−0.05	+0.00	−0.06
4	$\theta = 0°, +10°$	11.4	−0.01	−0.01	−0.05	+0.00	−0.02
5	*	03.2	−0.01	−0.02	−0.04	−0.01	+0.02

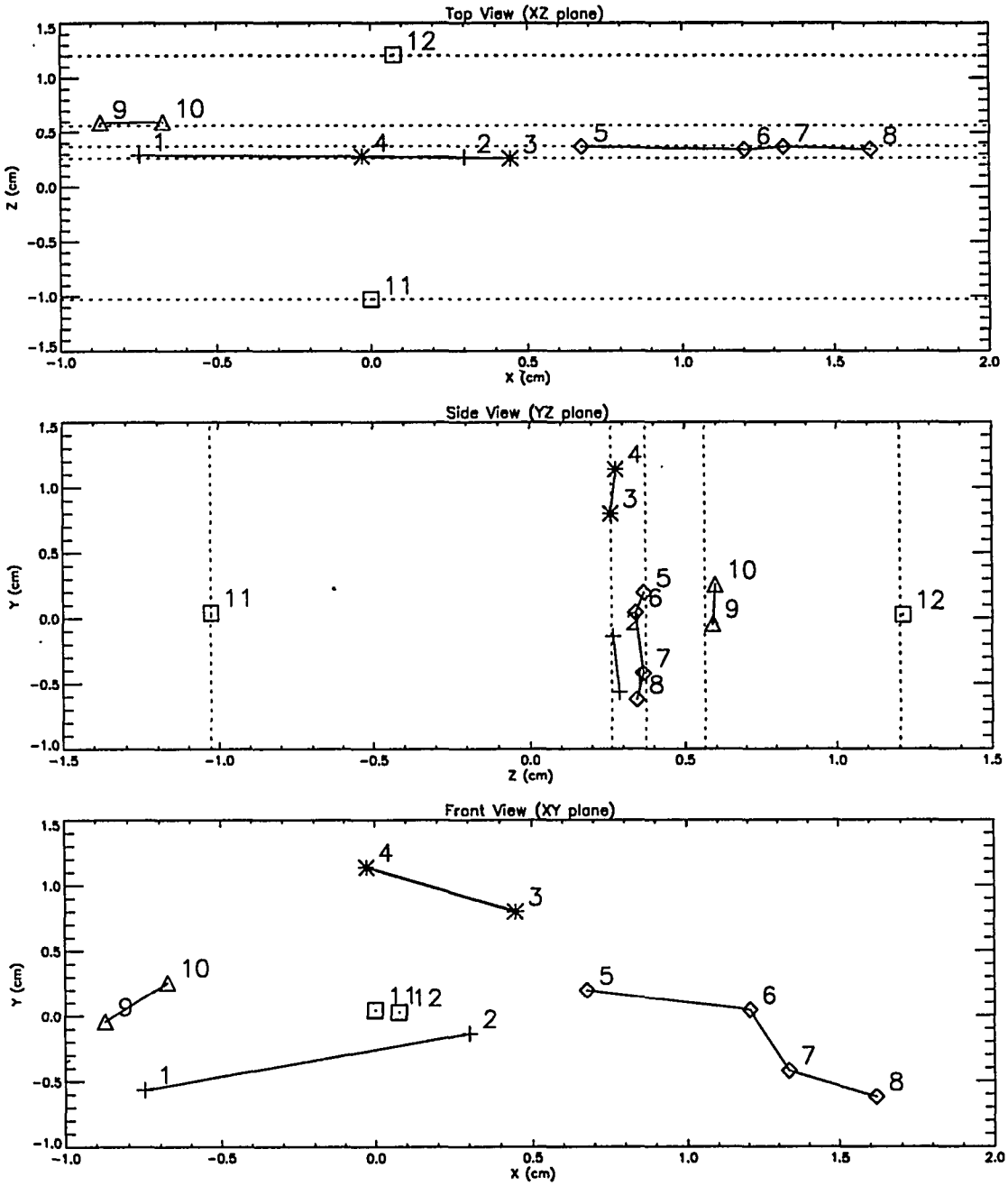

Figure 5.11: Range point measurements for aluminum plate

thickness had more variability (see the results of Tests 2 and 3 compared to the other tests); the reason for this is not known, although operator error in determining the feature points is the most likely cause.

As mentioned before, plate rotation presents an increased effective thickness to the X-ray beam, which decreases the image contrast and, hence, the detectability of the feature of interest. Detectability is characterized by percentage thickness of the feature relative to the host material. A spherical flaw of diameter t embedded in a plate of thickness T oriented normal to the X-ray path is $(t/T) \times 100\%$. The effective thickness T_e of the plate after rotation through an angle θ is $T_e = T/\cos\theta$. The overall percentage thickness of the spherical flaw is thus

$$\%thickness = \frac{t\cos\theta}{T} \times 100\%. \tag{5.3}$$

The real-time detector can detect the feature down to 2% thickness. In comparison, radiographic film can detect down to 1% thickness. Therefore, for a given flaw thickness, there is a maximum rotation angle $\theta_{max} < 90^\circ$ that can be used and still maintain flaw detectability. Maximum detectability occurs at $\theta = 0^\circ$. On the other hand, for a two-view rotation measurement the condition number CN is maximum at $\theta = 0^\circ$ and minimum at $\theta \simeq 90^\circ$. Consequently, the variance in depth measurement is highest when maximum feature detectability is highest. The optimum angle θ_{opt} is the point where CN is minimized and θ_{max} due to rotation is minimized.

The MEM image restoration was applied to determine its effectiveness for improving the resolution of the wire features. A Gaussian PSF of 2.9 pixels was selected to correspond to the 6" image intensifier used for the experiments in this chapter. A flat-field image was divided out as a pre-processing step. This eliminated the non-uniform background, and also reduced the fixed-pattern CCD camera noise. Twenty

Table 5.6: Variance of operator-determined screen coordinates using MEM

Feature	Standard Deviation of Position	
	Horizontal (pixels)	Vertical (pixels)
Input, 1	0.56	0.56
MEM, 1	0.50	0.64
Input, 2	0.69	0.51
MEM, 2	0.55	0.52

iterations of the MEM routine were used on 256×256 sub-regions about Wires A and D. The edge definition of the wires was improved a little. Two wire endpoints were used in a cursor variance test as in Experiment 1 to determine if MEM processing could reduce the variance associated with identifying feature points; the results are indicated in Table 5.6. The standard deviations varied at most by a tenth of a pixel, so the MEM processing did not significantly reduce the variance in selecting the feature points. The effect on the overall system accuracy of a tenth pixel reduction in the standard deviation of feature measurement noise was determined using a two-view 30° rotation simulation as in Chapter 3. Feature measurement noise of 0.7 pixels was applied in both the X and Y directions for a 4× configuration, and the depth standard deviation was 0.013 cm. Reducing the measurement noise to 0.6 pixels resulted in a 0.002 cm reduction in the standard deviation of the depth measurement. This change is an order of magnitude lower than the existing error, so the improvement was negligible. For this plate sample, MEM processing was found to be marginally effective in reducing the blur, but it did not make a substantial improvement in reducing operator error in determining feature points.

Using increased magnification would effectively increase the resolution of the

image. The plate could be manipulated to make a single wire fill the display screen. The coordinates of only a single wire could be determined, but this process could be repeated for each wire individually.

This sample demonstrated how plate-like geometries could be measured as easily as axially-symmetric geometries. While rotations of $\sim 90^{\circ}$ maximize the well-conditionedness of the least-squares inversion problem, rotations of only 10–30° were sufficient to achieve a satisfactory error level. The effective thickness of the rotated plate only increases by 16% at 30° rotation, so the feature detectability remains high. If more reliability is required, real-time contrast enhancement can extend the rotation amount to 60°, and increasing the X-ray source current and voltage would be able to extend the rotation angle another 10–20°. The effective thickness of the plate increases rapidly after the rotation angle exceeds 80°, so this places an upper limit on the amount of rotation that can be used.

This experiment showed that this 3-D RTR-based measurement technique can be successfully applied to samples that cannot easily be measured with a CT system. The specialized limited-view CT reconstruction algorithms require long computation times, and the resulting images must be thoroughly understood to ensure that artifacts are not corrupting the measurement. However, it must again be pointed out that the RTR-based measurement only yields the coordinates of a set of discrete points within the sample, where the CT image contains much more information. The utility of either of these two methods has to be determined based on the specific application.

Experiment 3: Turbine Blade

A turbine blade from a jet engine is used in this example. The blade is subjected to high temperatures in operation, so coolant tubes are embedded in the center of the blade. The blade has a spatially varying size and contour, and the coolant tubes must be properly located within the blade at all positions in the blade interior. An NDE procedure is required to verify that the tubes are properly oriented and do not pass too close to the surface of the part. The turbine blade sample is used to show how the real-time 3-D technique can be used for this type of dimensional analysis as well as for flaw sizing.

Figure 5.12 shows a diagram of the CAD model of this part. The grooved base of the turbine blade connects to the turbine axis. Nine coolant tubes enter at the base and exit at the top of the blade (the exit holes are visible on the top of the CAD drawing in the figure). The blade is made of a nickel alloy which highly attenuates X-radiation. A thinner section near the top of the blade was selected for 3-D measurements since it was easier to get good a signal in this region.

Using a CT image allows the hole diameters and hole positions relative to the external surfaces to be measured simultaneously. However, the geometry of the turbine blade presents a challenge to CT reconstruction since the effective material thickness changes radically over a 180° scan. Limited-view CT reconstruction methods have been developed to circumvent this problem, but they are still prone to introducing artifacts into the image.

The 3-D real-time method can find the locations of the hole axes. The hole diameters are estimated directly from the 2-D projection. Lead markers must be added to determine the 3-D contour of the external surfaces of the blade, which

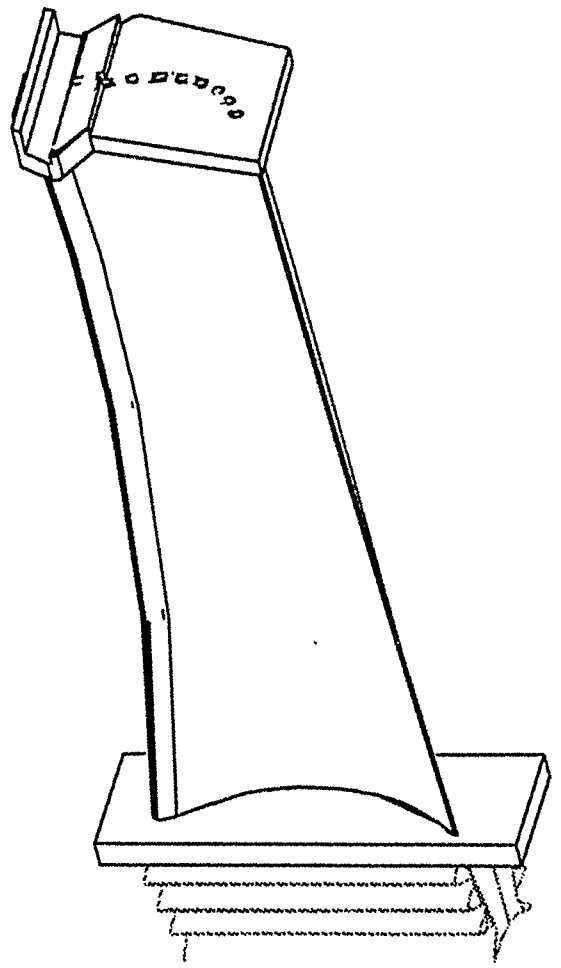

Figure 5.12: CAD model of turbine blade sample

highlights a disadvantage of this method. Adding too many markers clutters the image and makes it difficult to clearly identify correspondence points. Adding too few markers does not convey much information about the shape of the external surface. In practice, a jig could be used to hold the turbine blade in a well-known location on the sample positioner. The external surfaces would be inferred using a CAD model of the system. However, as indicated by the simulations of Chapter 3, this type of absolute measurement in the global coordinate system is highly sensitive to bias errors in determining the positioner center of rotation, so a relative measurement in the sample coordinate system is preferred. This could be done using a part handler with built-in lead markers. The handler would need to be made of a pliable material that would place the lead markers in close contact with the blade surface.

For this experiment, seven markers spaced approximately 3 mm apart were affixed to the inner (concave) surface, and 9 markers were attached to the outer (convex) surface. The inner surface markers were placed closer to the top of the blade to make them easily distinguishable.

Figure 5.13 shows the real-time image of the blade oriented at 0°. The concave surface was located facing the source. The nine higher intensity stripes are the image of the coolant tubes, and the lead markers are the short darker strips spaced at regular intervals. Note that all nine tubes are visible in this orientation, although the tube on the far left is more difficult to see since the blade was thicker on that side (the blade is shaped like a curved airplane wing, so one side is thick and rounded while the other side is thin and tapered).

The blade was rotated to $+30^{\circ}$ (Figure 5.14); this increased the effective thickness of the blade on the left side of the image and reduced it on the right side.

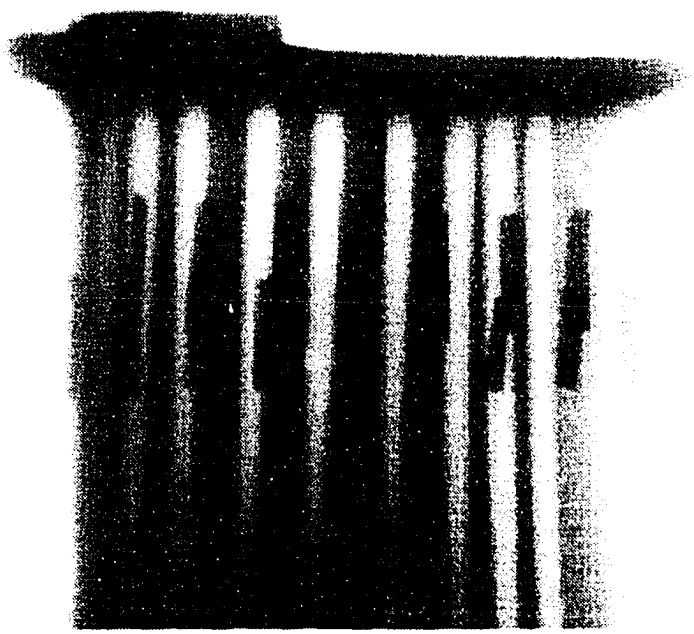

Figure 5.13: Real-time image of turbine blade oriented at 0°

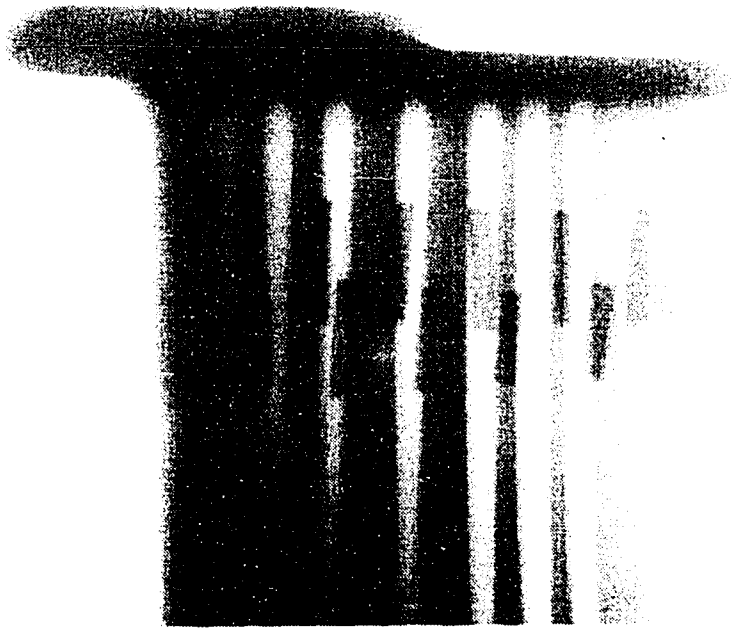

Figure 5.14: Real-time image of turbine blade oriented at $+30^{\circ}$

Consequently, the tube images became undetectable on the left side. Generally, increasing the X-ray power would solve this problem, but the blade curvature caused the tube images to overlap, so this was not a solution. When the blade was rotated the other direction to -30° (Figure 5.15), the left tubes became easily detectable, but the rightmost tubes disappeared from the image.

Due to its geometry, the blade could be rotated at most only 20° and still maintain visibility of all nine tubes in both views. To overcome this problem, the holes and marks on the left side of the image were measured using two views at 0° and -30°, and the features on the right side of the image were measured using views at 0° and $+30^{\circ}$. Three complete measurements were made, and all three results

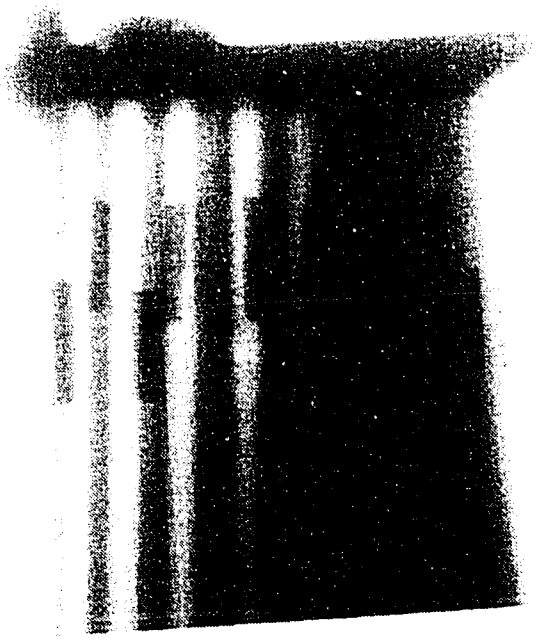

Figure 5.15: Real-time image of turbine blade oriented at -30°

are plotted as a top view (XZ plane) in Figure 5.16. The inner and outer surfaces defined by the lead markers are plotted with connecting lines, and the hole positions are plotted individually. Some points were more difficult to identify than others due to overlapping features, which increased the Z variance of some points compared to others. The same image row (250) was used for all features since no vertical features were available.

This sample was used to demonstrate how multiple sets of measurements could be made, with each set utilizing a greater rotation angle than that permitted by measuring all the features simultaneously in both views. This flexibility overcomes problems due to complex geometries in which some of the features occlude in certain sample orientations.

Experiment 4: Automotive Air Conditioner Part

This sample is an aluminum casting used as part of an automobile air conditioner. A drawing of a CAD model for this part is shown in Figure 5.17. The part has a wide variety of thickness variations, with the thickest sections on either end of the part, and the thinnest regions in the middle of the part. These thickness variations result in a large variation of X-ray absorption, and leads to simultaneous underexposure (not enough photons for good signal-to-noise ratio) and overexposure (detector saturation) in different parts of the image. The real-time system has an advantage in that the X-ray source power and image processing parameters can by dynamically altered to optimize different parts of the image, based on which region is of interest at the moment.

This sample contains cracks due to shrinkage porosity throughout its interior

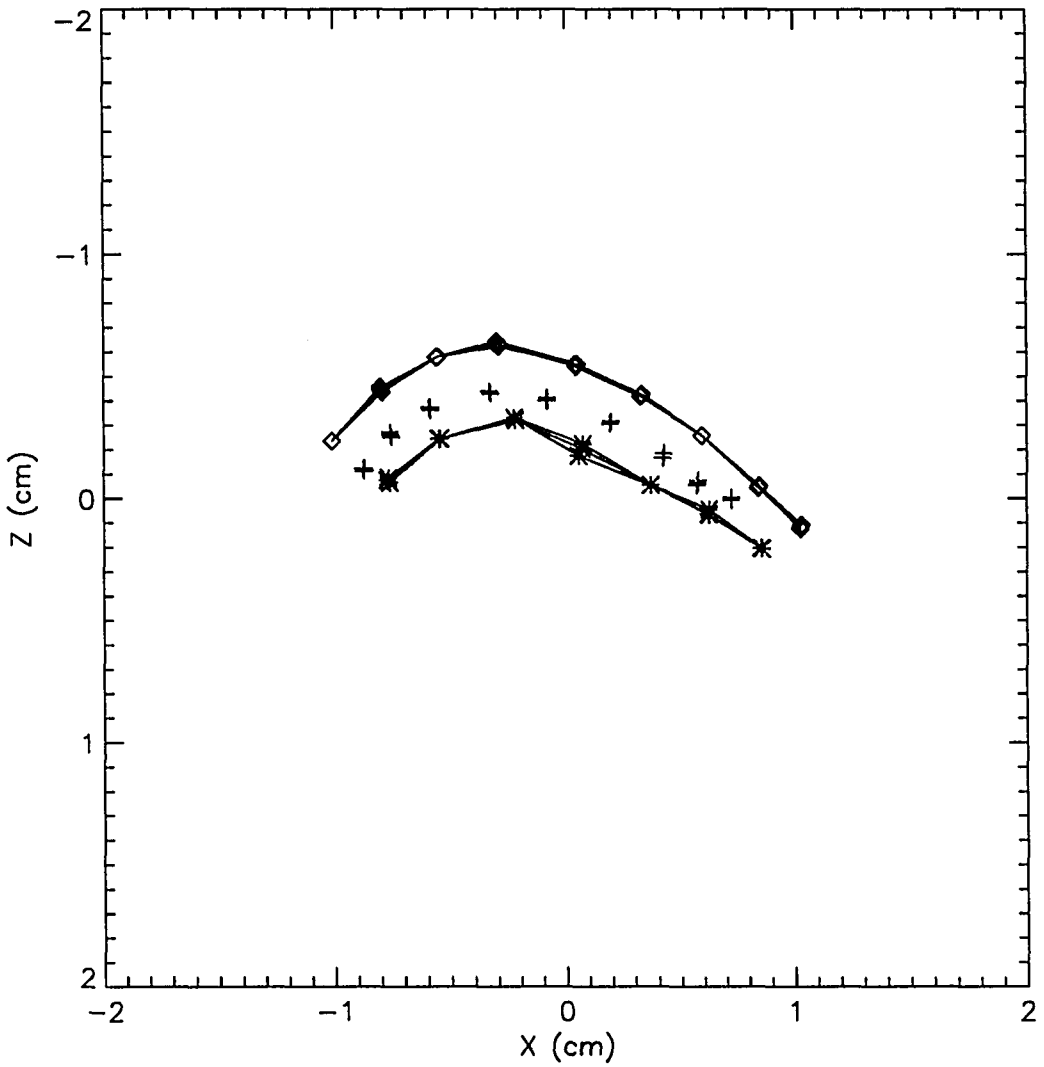

Figure 5.16: Top view (XZ plane) of turbine blade measurements

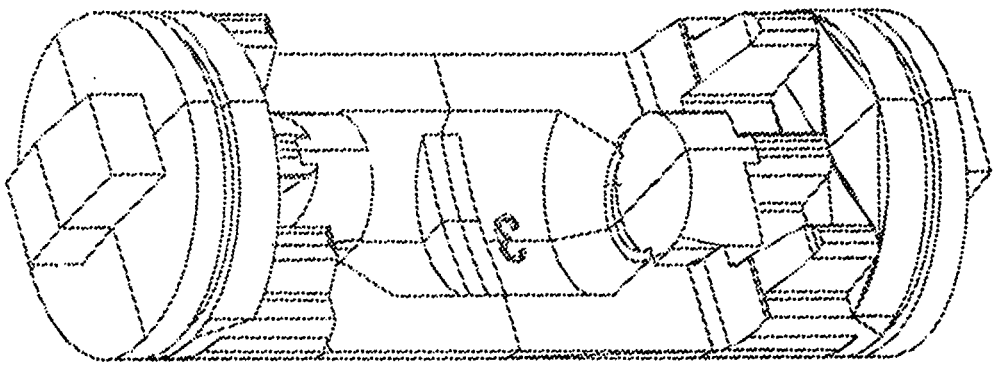

Figure 5.17: CAD model of automobile air conditioner part

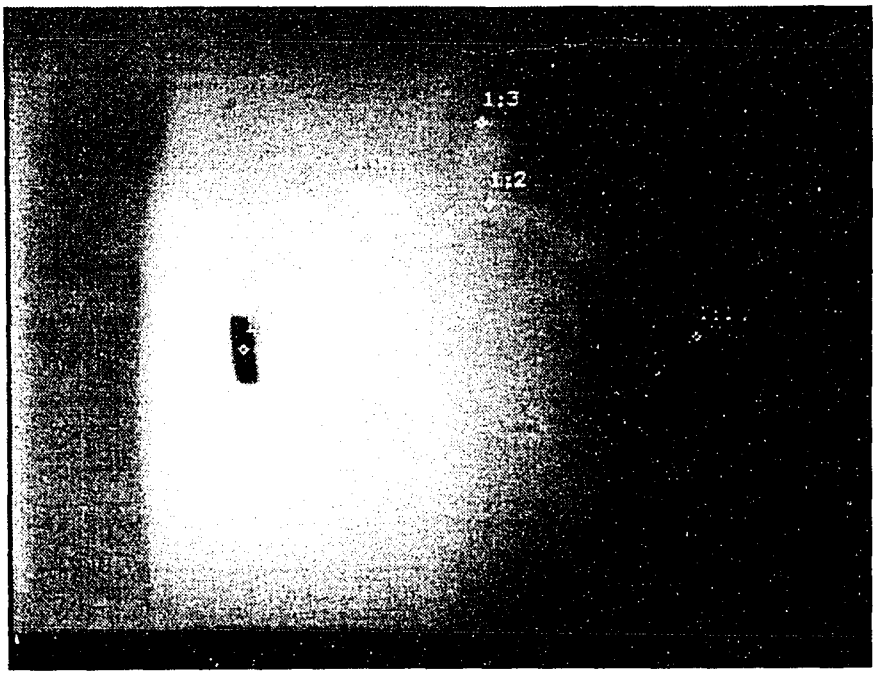

Figure 5.18: Real-time image of image of air conditioner part

due to improper manufacture. A particular fork-shaped crack located near the "3" was selected for measurement; the real-time image of this feature is indicated in Figure 5.18. The gray curved stripe on the left of the image is the projection of the center fillet of the casting to the left of the "3." The fillet appears curved since the casting was initially rotated about $+20^{\circ}$ to make the flaw more visible from the dark patch on the right side of the image. A lead marker was affixed to the back surface of the part which was placed closest to the detector. Five range points were selected to characterize the flaw, and two points were used to identify the inner and outer surface boundaries. These features are indicated as an overlay in Figure 5.18. The middle of the "3" was used as the inner surface feature, and the lead marker

was used as the outer surface feature. This demonstrates how including recognizable features in the design of the part can eliminate the need to attach external markers to identify the surface boundaries.

The results of three complete measurements are plotted in Figure 5.19. Since only two markers were used to locate the surface boundaries, the curved contours of the part were not measured. Dotted lines were drawn through the surface mark locations to give an idea of the flaw orientation relative to the surface. As mentioned previously, the part had an initial rotation of $+20^{\circ}$; this angle was used to plot the surface boundaries in the top view (XZ plane). Points 2 and 4 of the third data set had a depth deviation of 0.05 cm compared to the other two data sets, which accounts for the "messiness" of the plot in the side view (YZ plane). The flaw boundaries for these points were not as well-defined, so the feature point selection had higher variance. Furthermore, it was difficult to identify the corresponding points since the flaw significantly changed shape between views. This demonstrates how flaw morphology plays a significant role in determining screen measurement variance.

MEM processing was used to sharpen the flaw features located within two 256×256 subimages (Figure 5.20); the flaw boundaries were only marginally enhanced. Three complete measurements were made again using the MEM processed images, with the results plotted in Figure 5.21. The X and Y locations for all except Point 2 were determined with less variation, but the depth variation was not reduced compared to the previous measurement. The processing time for a 256×256 image was 4 minutes on the DEC5000. The improvement due to MEM processing was marginal as far as image quality is concerned, and was negligible in terms of reducing

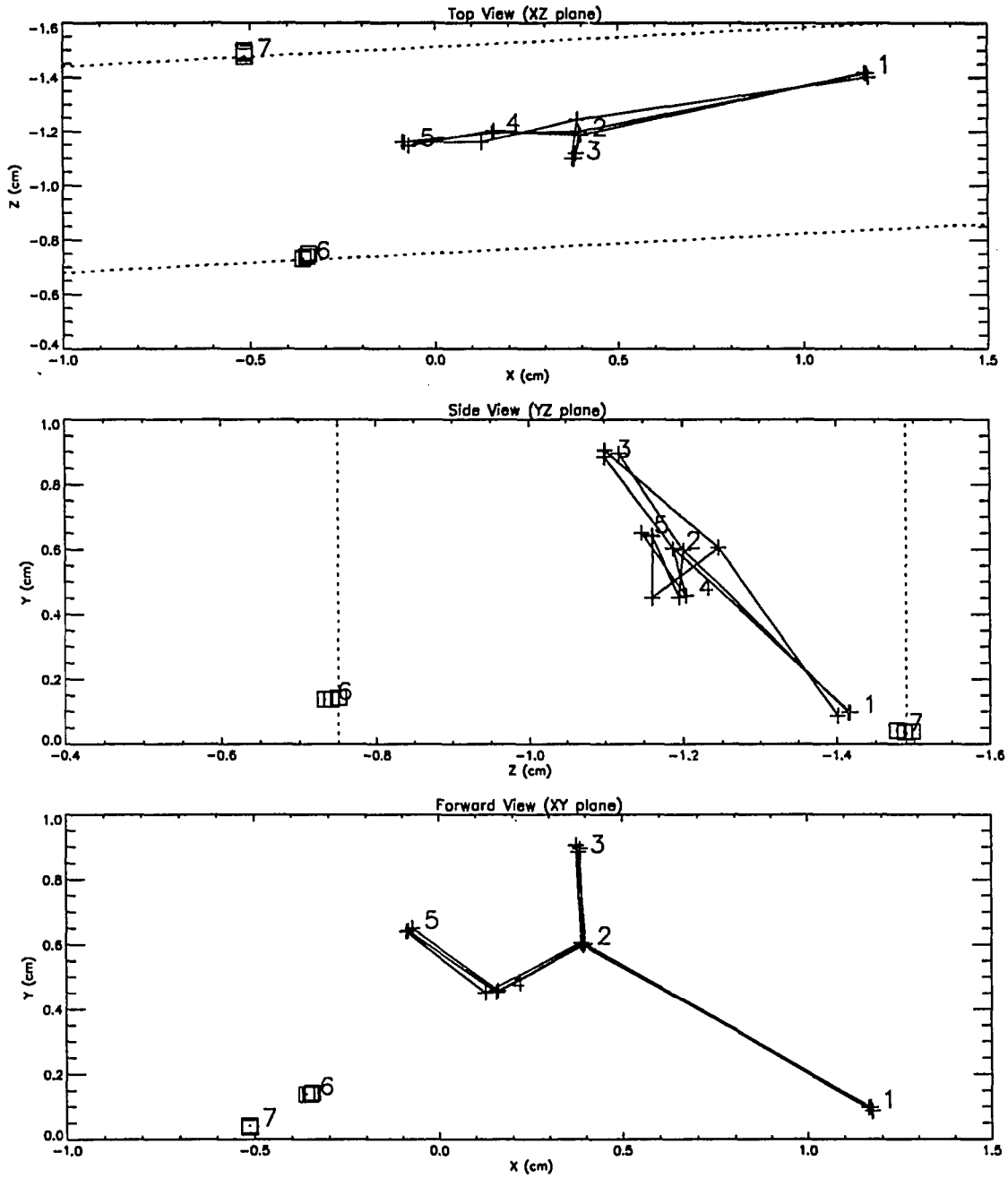

Figure 5.19: Range point measurements for air conditioner sample

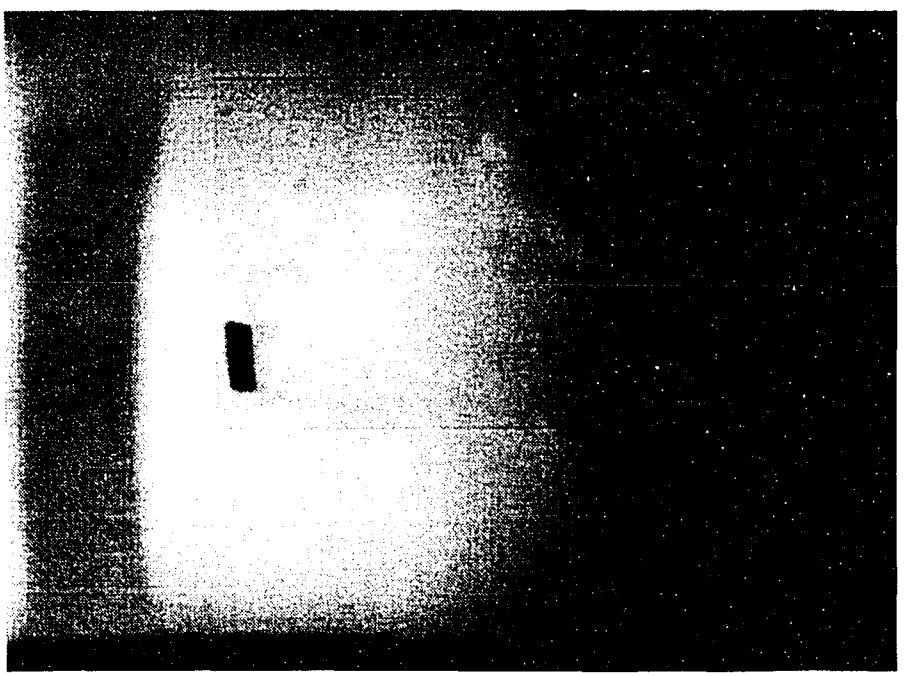

Figure 5.20: MEM processed image of air conditioner part

operator error in determining the feature points. Thus, the long computation time of MEM was not found to be justified.

This sample demonstrated the ability to make a 3-D crack orientation and size measurements. The features of interest had the poorest definition of the four samples used in this chapter, and the results showed an increased variance in depth as a result. Use of an edge detection scheme would eliminate the operator ambiguity problem, yet these features would also present a challenge to an automated edge detector as well. This showed that measurement error in determining the feature points is a significant component of the overall measurement error, so it would be valuable to incorporate as much automatic and robust edge detection as possible.

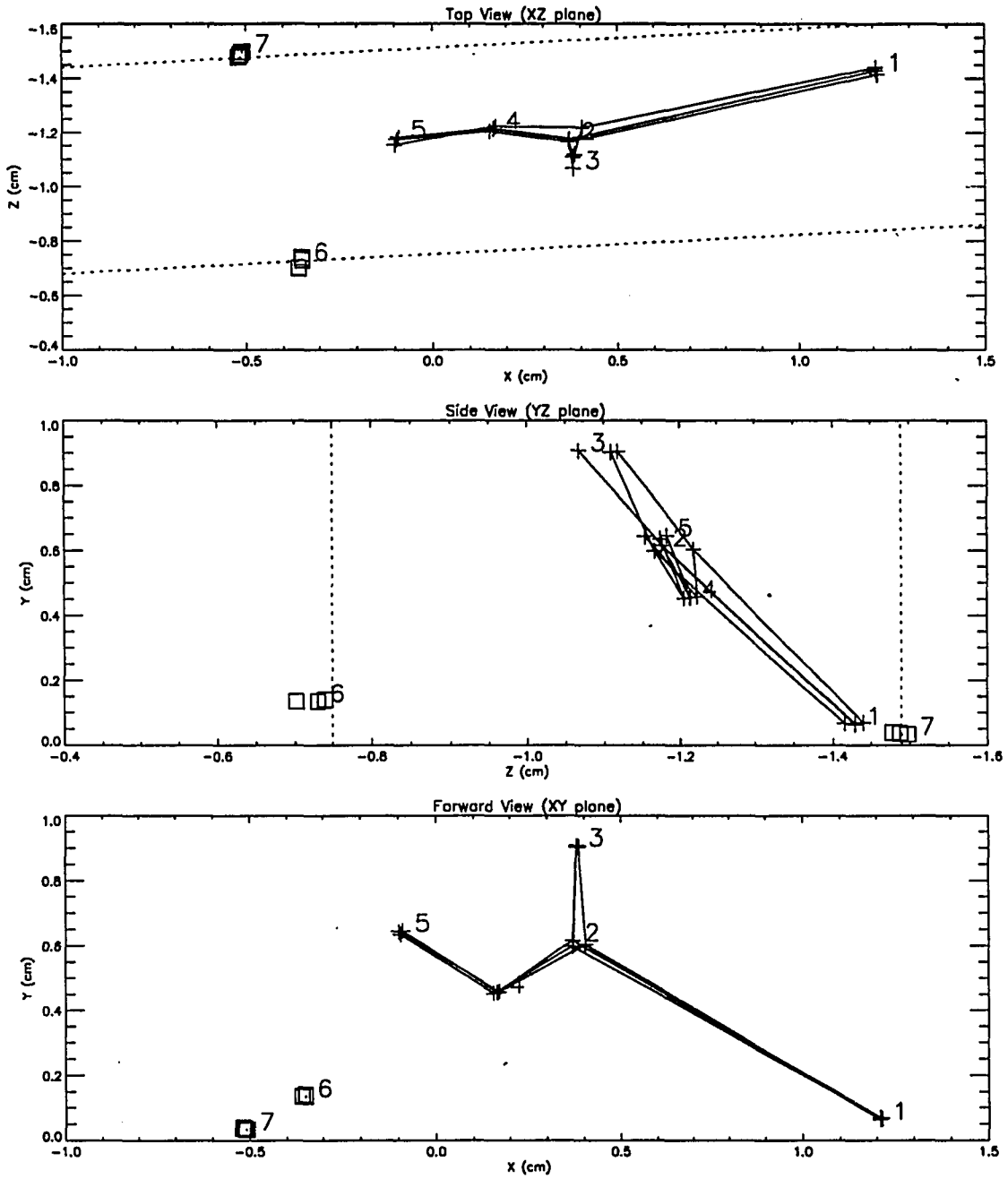

Figure 5.21: Range point measurements for air conditioner sample using MEM processed image

CHAPTER 6. SUMMARY AND CONCLUSIONS

A system has been developed to make accurate three-dimensional measurements of features of interest within a material sample using a real-time X-ray imaging system. This 3-D capability adds a useful tool to the RTR laboratory, and permits accurate determination of feature lengths and orientations within a sample at a fraction of the cost of a CT-based measurement. The mathematical foundation for this system was specifically developed to exploit the general-purpose motion control provided by the multi-axis sample positioner. This system can deliver good (± 0.02 cm) measurement results using only two views and small ($\sim 20^{\circ}$) rotations between views, so axially-symmetric as well as plate-like geometries can be measured with a minimum of data collection effort. In addition, each of the tools developed for this 3-D measurement system has broad applicability to other types of measurements. For example, the pincushion distortion correction and source/sample calibration techniques would be necessary to achieve accurate results for a CT measurement using the RTR laboratory. The software/hardware framework developed for real-time image processing makes it possible to implement any image processing algorithm, and the region-of-interest processing technique makes efficient use of the frame processor resources since it is usually not necessary to process the entire image for every frame. Furthermore, the use of a general DSP board makes it possible to implement

on-line data analysis as data is collected, e.g., a CT reconstruction could be carried out in parallel with data acquisition, rather than waiting for the entire data set to be obtained.

The overall accuracy of the system is governed by how well the X-ray source, sample, and detector positions are known, how accurately the X-ray detector can be calibrated, the accuracy of sample movement between views, and by the user's ability to accurately identify the correspondence points. A simple image-oriented technique was developed to calibrate the physical positions of the X-ray source and positioner center of rotation to within ± 1 mm. The sample positioning device used for this work was extremely precise; this level of precision is not required compared to other portions of the system. Furthermore, the generality of sample motion is not a requirement. A fixture which rotates only a fixed amount would be suitable for some applications. Software techniques were implemented to improve the resolution and spatial linearity of the X-ray detector. The spatial distortion of the X-ray detector was corrected to below the level of sampling uncertainty of ± 0.5 pixel.

The operator is a key aspect of the overall measurement quality of the system. The intelligence of the operator is relied on to accurately determine the initial features of interest and their corresponding points in subsequent views. The operator is responsible for making any changes in the real-time processing or X-ray generator setup needed to visually see the feature for all sample orientations. The interactive and continuous nature of the real-time X-ray image naturally lends itself to using a human operator as an integral part of the system. The continuous X-ray image eliminates the problems of occluded points and crossed disparities associated with film-based stereography. If two points appear to be occluding, the operator simply

moves the sample a little to eliminate the problem. Crossed disparities are not a problem since the operator can watch how two features are moving within the image and know that they have crossed.

Given that the operator has certain tasks to perform, the software was designed to make these tasks easy to perform. The sample control program was tied together with the correspondence point determination program, thus freeing the operator to concentrate on how to move the sample, rather than keeping track of exactly how the sample was moved. The correspondence points were labeled at each view to make it easier to see how much disparity each point had encountered. Real-time processing was seamlessly integrated in to the correspondence point determination program so contrast enhancement routines could be invoked on a region of interest around the feature. Additional frame grabber capabilities such as image magnification, profile display, and pseudocolor enhancement were also incorporated to make identification of correspondence points easier.

The smooth integration of real-time processing into the correspondence point determination program was found to be a significant aid to the operator. A combination of trend removal followed by a contrast stretch made it possible to rotate the plate sample through a greater angle, which reduced sensitivity to measurement error. The ability to dynamically alter the number of video frames averaged and processing parameters made it convenient to use a low SNR/fast updated image for sample movement or a high SNR/slow updated image for feature point selection.

Three laboratory calibration steps were required: one to identify the 3-D X-ray source position, one to identify the sample center of rotation, and one to calculate the X-ray detector spatial warp coefficients. These techniques were image-based

and required only two physical measurements to be made with a tape measure (the source/detector Z distance and the center of rotation Z distance) and one image to be collected of a uniform grid object. The source position was determined to ± 1 mm in all three coordinates, and the spatial distortion of the X/L convertor was corrected to below the sampling uncertainty of ± 0.5 pixel. The entire laboratory calibration process required one hour at most, so it was not a problem to recalibrate after the laboratory was used for another experiment.

Collinearity of the source, range point, and measurement point, and a linear transformation of the form $\mathbf{y} = \mathbf{A}\mathbf{x} + \mathbf{b}$ were the bases of a concise, nonparametric system of equations. This system was inverted to solve for the range point coordinates, and at least two measurement points were required to yield a unique solution. Additional measurements were easily accommodated to increase the overdeterminedness of the least-squares solution. The cross product operator $\mathbf{C}_\mathbf{x}$ made it possible to the express the collinearity constraint in matrix form, thus simplifying the development of the complete system.

The operating characteristics of the specific X/L convertor used for this work (an image intensifier tube) were thoroughly investigated. Since the detector was used for spatial measurements, reducing its spatial degradations was of prime importance. The X-ray detector pincushion distortion was the dominant systematic error in this system. A simple polynomial-based image warp was sufficient to correct the distortion, initially as high as 0.45 cm (28 pixels at 60 pixels/cm sampling frequency), to less than ± 0.5 pixels (0.008 cm). Blurring due to phosphor bloom, although significantly reducing resolution of the real-time image compared to film, did not significantly impair the user's ability to identify feature points in the image.

A high resolution edge scan was implemented to measure the point spread function of the image intensifier. A Gaussian curve satisfactorily modeled the PSF as evidenced by the reduced chi-squared goodness-of-fit criterion. The FWHM of the Gaussian was measured as 2.9 pixels (0.048 cm at 60 lp/cm sampling frequency) for the image intensifier tube. This PSF was used by the maximum entropy method to reduce image blurring. Analysis of a resolution gauge image indicated a +8 dB increase in spectral amplitude at 1.0 lp/mm frequency; the increase continued to the break-even point of 1.7 lp/mm. This increase was obtained without increasing the image noise. However, the increase in spectral amplitude only occurred in the lower 57 percent of the usable bandwidth between 0–3 lp/mm as defined by the folding frequency of the quantizer. This sharpened the image a bit, but not enough to make an improvement in the overall system accuracy. From a price/performance standpoint, the image warp was found to be a much better use of computational resources.

The measurement simulator successfully verified the system performance, and also provided insight into determining which aspects of the system were of key importance. The system was fairly insensitive to random errors when a two-view rotation of at least 20° was used. The system was most sensitive to bias errors in determining the sample center of rotation. This was more of a problem for making absolute depth measurements in the global coordinate system. The bias error was only 0.01–0.02 cm when making relative depth measurements within the sample's local coordinate system. Making multiple intermediate measurements was found to reduce the depth estimation error slightly (0.002 cm), but not enough to justify the extra expense of data collection. Translation was found to be very inefficient compared to rotation to achieve a given error level. At least 15 cm translation at 4× magnification was

required to reach the same result as a 20° rotation. Plate-like geometries are the only ones with potential problems for rotation, but a 20° rotation only increases the effective thickness of a plate by 6 percent. Consequently, small-angle two-view rotations are suitable for any sample geometry.

Feature selection from the display screen was the dominant source of random error in the system. Variance in selecting a single point is a function of edge blurriness, feature size and contrast, and detector quantization. Using a higher resolution quantizer such as a 1K×1K frame grabber would reduce variance when the feature is well-defined. Alternatively, placing the sample away from the detector in a magnification setup improves the system accuracy, since magnification effectively increases resolution of the detector at the cost of reduced field of view. The microfocus source allows higher magnification than a broad focus source, but the sample thickness and composition is then limited. The microfocus source is also considerably more expensive. Good results can be obtained with a broad focus source (1× magnification), but the sample must be rotated close to 90° to get measurement error down to ±0.01 cm.

Four samples were used to experimentally determine the system performance. Feature length measurements were tested using the aluminum cylinder and plate samples; standard deviations in length were 0.01–0.02 cm, and biases were ±0.00–0.05 cm. These values were confirmed by simulation. The aluminum cylinder was also used to show that a rotation of at least 15–20° was required to yield a well-conditioned $\mathbf{X}$ matrix, and hence, a stable solution of the system inversion. The plate sample measurements indicated that the system could successfully identify the depths of the four embedded copper wires, and was able to distinguish between two wires located 1 mm apart in depth.

A turbine blade sample was used to demonstrate how the system could be used for dimensional analysis, in this case, the determination of the central axis positions of nine coolant tubes relative to the blade surfaces. The same depth errors (0.01–0.02 cm) were encountered for this sample. This represented roughly 7% of the turbine blade's maximum thickness; the suitability of this value as the basis of a quality assurance test would have to be determined by the blade manufacturer or end-user. Again, increasing the system resolution through magnification or use of a higher resolution digitizer would improve the measurement result.

An automobile air conditioner part containing shrinkage porosity was used as an example of a real crack defect. The flaw boundaries were the least defined of all the samples investigated, and resulted in twice as much depth error (±0.04 cm). MEM processing sharpened the flaw boundaries a bit, but did not improve overall accuracy in determining the range point depths.

Previous investigators reported depth measurement errors ranging from ±0.6 cm (Wallingford, 1988) to ±0.004 cm (Veress, Lippert, and Takamoto, 1977). The latter work used radiographic film, a broad focus X-ray source (1× magnification), and photogrammetric measurement equipment to obtain the correspondence points. Upgrading the present RTR system to use a 1K×1K frame grabber or using higher magnification on the order of 20× would make this system comparable to the results reported by Veress *et al.*

The need to attach external markers to identify the surface of the sample highlights a disadvantage of this system compared to a CT-based measurement. As the sample geometry becomes more complex, more markers are required to adequately describe the surface contours. On the other hand, too many markers tends to obscure

the feature of interest within the sample. Using a fixture on the sample positioner would be one solution, but the measurement system is very sensitive to error in knowing where the fixture is located in the global coordinate system. Relative measurements made within the sample's local coordinate system are not subject to this problem. Placement of the lead markers would be simplified by building them into a part handler. Alternatively, marks could be designed into the part at key locations.

Ideas for Future Work

Integration with CAD model

The present system does not use any information about the sample geometry. Incorporating this information via a CAD model would make a more effective display of the 3-D locations of the features of interest measured by the RTR system. Reference points (like the lead markers) could be added to the CAD model. The sample coordinate system used for the RTR measurements could be referenced to some known feature on or within the CAD model. The results would be displayed either as orthographic or perspective displays. Distances from the measured points of interest to any feature on the sample could be easily computed this way.

Detector characterization

Techniques have been developed to determine the PSF directly from the image of interest rather than using a separate measurement step. (Andrews and Hunt, 1977; Chalmond, 1991). Some of these techniques rely on *a priori* knowledge of edge locations within the image. This is a less controlled method than that used in Chapter 4. Other techniques assume a given noise field as input to the system and

determine a Markov model which describes how the input noise field was blurred to yield the output noise field. The latter technique would be most useful in the RTR environment since images of only the X-ray source are readily made.

Improvements are possible with the high resolution edge scanning technique described in Chapter 4. The current implementation samples only a single pixel and saves it as 8-bit data. The frame grabber used for this work has a 16-bit buffer, so up to 255 frames could be saved into this buffer to improve gray level resolution. The 16-bit number would be saved rather than truncating it to 8 bits as is done now. In addition, a neighborhood of pixels about this measurement pixel could be sampled as well. Registration and ensemble averaging of this neighborhood would improve the SNR and reduce or eliminate the need to use a smoothing convolution filter. Registration is simple since the pixel pitch of the CCD array is accurately known. The small neighborhood is required since the image intensifier PSF is constant over small areas of the image.

Automatic calibration and measurement

The source position calibration procedures outlined in Chapter 5 are essentially manual. The X and Y coordinates of the X-ray source position require the Z coordinate to be known in advance. This was determined using a tape measure and was confirmed by checking the magnification of objects of known length. A more automated method can be designed around a calibration phantom of known length. Measuring the magnification at a series of Z locations forms a least-squares problem in which it is possible to determine both the sample positioner Z location and the source Z location.

The procedure to determine the X and Y coordinates of the X-ray source position could be automated by implementing a control algorithm to keep the sample point lined up with the detector point. The user would align these points at the initial Z location and indicate the ΔZ to the program. The program would increment the Z position of the sample point a small distance, and make adjustments in the X and Y sample position to bring the sample point back in line with the detector point. Using small Z increments results in small perturbations of the sample point relative to the detector point, so the level of image interpretation to distinguish the two points would be minimized. This procedure would continue until the sample Z position reached the user-selected ΔZ value. The accumulated corrections in the X and Y components of the sample position would be used as the ΔX and ΔY values required for the source position calculations.

An alternative technique would require the user to line up the sample and detector points as before, but translate the sample point the full ΔZ length. The user would identify the sample point and detector point for the computer. The computer would track the sample point while manipulating the X and Y positions of the sample. A homing algorithm would be used to make the image of the sample point match the image of the detector point. This procedure would yield the ΔX and ΔY values as before. Since there are only two features in the image and the sample point is well-defined, a simple tracking algorithm can be employed.

Many aspects of the measurement process could be automated as well. Identification of correspondence points is prone to operator error. A first step towards automation would require the operator to select an initial view and points of interest. An automatic point tracking process would be invoked at this point to free the

operator from having to follow all these points around the screen as the sample is manipulated. The computer could continuously compute the 3-D coordinates of the sample points and present this information graphically and numerically in real-time. The condition number and error statistics could also be reported to indicate how well the experiment is performing. Periodically the user would indicate to the system when to use the current view as a new set of data points. The user would stop the program when the error statistics had reached a satisfactory level. In this way, the user could concentrate more on how to manipulate the sample to achieve good measurements rather than tracking simultaneously moving features of interest.

The automatic tracking algorithm has to overcome the same set of problems previously encountered with film-based stereography (Wallingford, 1990). The availability of the continuous position of the feature eliminates some problems such as crossed disparities, but occluded and intersecting features require the tracking algorithm to use the previous history of the feature (position, velocity, acceleration) to make sense of a situation where two features have intersected and only one feature is visible. Well-defined features in the initial view could evolve into poorly-defined features in subsequent views. Plate-like geometries which have a thin and thick dimension cause the feature SNR to drop when the thicker portion of the sample is imaged. This problem could be solved by allowing the computer to boost the X-ray power when the flaw SNR decreases below a certain level. Local SNR measures have been developed to measure the signal strength (Doering, 1991a); these could be used to measure the SNR of each feature.

Operator intervention in the measurement process could be further reduced by implementing an algorithm to automatically determine how to manipulate the sam-

ple. In this case, the user would simply identify features of interest in the initial view, and the computer would adjust the sample position until a given level of confidence was achieved. This can be formulated as a minimization problem with constraints. Minimization of the matrix condition number would serve as a quantitative goal. The constraints include keeping the feature points in the field of view, and keeping the sample within a certain range between the source and the detector.

The above ideas for automation are geared towards making a general-purpose scanning system. In a manufacturing environment, it would be more practical to tailor the image processing routines to a given part. The initial view and subsequent part translations/rotations would be determined in advance. Image processing routines could be developed to identify the points of interest in the initial view and modified views. Thus, as the problem becomes specific to a certain part, the generality of the RTR lab used for this development could be reduced to only the elements that are needed.

BIBLIOGRAPHY

ASTM E 1000-88. 1988. Standard guide for radioscopic real-time imaging. Pages 389–407 in Annual Book of ASTM Standards, Vol 03.03. American Society for Nondestructive Testing, Inc., Columbus, OH.

ASTM E 1255-88. 1988. Standard practice for radioscopic real-time examination. Pages 575–579 in Annual Book of ASTM Standards, Vol 03.03. American Society for Nondestructive Testing, Inc., Columbus, OH.

Andrews, H. C., and B. R. Hunt. 1977. Digital image restoration. Prentice-Hall, Englewood Cliffs, NJ.

Bates, C. W., Jr. 1980. Concepts and implementations in X-ray intensification. Pages 45–65 in D. A. Garrett and D. A. Bracher, eds. Real-time radiologic imaging: medical and industrial applications. American Society for Testing and Materials, Philadelphia, PA.

Betz, R. A., and R. C. Barry. 1988. Description of a rapid, high-sensitivity real-time radiographic system. Materials Evaluation 46:1424–1428.

Bevington, P. R. 1969. Data reduction and error analysis for the physical sciences. McGraw Hill, New York, NY.

Bryant, L. E., and P. McIntire, eds. 1985. Nondestructive testing handbook, 2nd ed., vol. 3: Radiography and radiation testing. American Society for Nondestructive Testing, Columbus, OH.

Buechler, D. W. 1987. Real-time radiography for electronics reliability assessment. Materials Evaluation 45:1326–1329.

Burch, S. F., S. F. Gull, and J. Skilling. 1983. Image restoration by a powerful

maximum entropy method. Computer Vision, Graphics, and Image Processing 23:113-128.

Casperson, L. W., P. Spiegler, and J. H. Grollman, Jr. 1976. Characterization of aberrations in image-intensified fluoroscopy. Medical Physics 3(2):103–106.

Chakraborty, D. P. 1987. Image intensifier distortion correction. Medical Physics 14(2):249–252.

Chalmeton, V. 1980. Microchannel X-ray image intensifiers. Pages 66–89 in D. A. Garrett and D. A. Bracher, eds. Real-time radiologic imaging: medical and industrial applications. American Society for Testing and Materials, Philadelphia, PA.

Chalmond, B. 1991. PSF estimation for image deblurring. Computer Vision, Graphics, and Image Processing: Graphical Models and Image Processing 53(4):364–372.

Christensen, E. E., T. S. Curry, III, and J. Nunnally. 1972. An introduction to the physics of diagnostic radiology. Lea and Febiger, Philadelphia, PA.

Cornwell, T. J., and K. F. Evans. 1985. A simple maximum entropy deconvolution algorithm. Astronomy and Astrophysics 143:77–83.

Corso, R. 1992. Private communication. Precise Optics Photo Medic Equipment, Inc., Bay Shore, NY.

Cortes, A. B., C.L. Lin, and J.D. Miller. 1991. An improved X-ray CT reconstruction algorithm suitable for quantitative analysis in industrial applications. Pages 459–467 in D. O. Thompson and D. E. Chimenti, eds. Review of Progress in Quantitative NDE Vol. 10A, Plenum Press, New York.

Csorba, I. P. 1985. Image tubes. Howard W. Sams and Co., Indianapolis, IN.

Cunningham, I. A., and A. Fenster. 1987. A method for modulation transfer function determination from edge profiles with correction for finite-element differentiation. Medical Physics 14(4):533–537.

Doering, E. R., and J. P. Basart. 1991a. Need for image goodness measures for X-ray imaging. Pages 789–795 in D. O. Thompson and D. E. Chimenti, eds. Review of Progress in Quantitative NDE Vol. 10A, Plenum Press, New York.

Doering, E. R., and J. P. Basart. 1991b. Improving the spatial resolution of real-time radiography images using the maximum entropy method. Pages 1072–1076 in R. R. Chen, ed. Conference Record for the Twenty-fifth Asilomar Conference on Signals, Systems, and Computers. IEEE Computer Society Press, Los Alamitos, CA.

Doering, E. R., J. N. Gray, and J. P. Basart. 1992. Point spread function estimation of image intensifier tubes. Pages 323–329 in D. O. Thompson and D. E. Chimenti, eds. Review of Progress in Quantitative NDE Vol. 11A, Plenum Press, New York.

Dyson, N. A. 1973. X-rays in atomic and nuclear physics. Longman Group Limited, London, England.

Eberhard, J. W., and K. H. Hedengren. 1988. Use of a priori information in incomplete data X-ray CT imaging. Pages 723–730 in D. O. Thompson and D. E. Chimenti, eds. Review of Progress in Quantitative NDE Vol. 7A, Plenum Press, New York.

Feldkamp, L. A., G. Jesion, and D. J. Kubinski. 1989. Fundamental aspects of micro-CT in cone-beam geometry. Pages 381–388 in D. O. Thompson and D. E. Chimenti, eds. Review of Progress in Quantitative NDE Vol. 8A, Plenum Press, New York.

Fougère, P. F. 1990. Maximum entropy and Bayesian methods. Kluwer Academic Publishers, Boston, MA.

Freiden, B. R., and D. C. Wells. 1978. Restoring with maximum entropy. Journal of the Optical Society of America 68(1):93–103.

Friedman, W. D., P. Engler, M. W. Santana, R. W. Ohnsorg, and D. A. White. 1991. The use of CT for dimensional measurements of green and sintered ceramic components. Pages 419–426 in D. O. Thompson and D. E. Chimenti, eds. Review of Progress in Quantitative NDE Vol. 10A, Plenum Press, New York.

Frobin, W., and E. Hierholzer. 1991. Video rasterstereography: a method for on-line measurement of body surfaces. Photogrammetric Engineering and Remote Sensing 57(10):1341-1345.

Glasser, J., J. Vaillant and F. Chazallet. 1988. An accurate method for measuring

the spatial resolution of integrated image sensors. Image Processing II, SPIE 1027:40–47.

Golub, G. H., and C. F. Van Loan. 1989. Matrix computations. 2nd ed. Johns Hopkins University Press, Baltimore, MD.

Gonsalves, R. A., J. P. Kennealy, R. M. Korte, and S. D. Price. 1990. FIER: A filtered entropy approach to maximum entropy image reconstruction. Pages 369–382 in P. F. Fougère, ed. Maximum Entropy and Bayesian Methods. Kluwer Academic Publishers, Boston, MA.

Gonzalez, R. C., and P. Wintz. 1977. Digital image processing. Addison-Wesley, Reading, MA.

Gupta, N. K., and B. R. Krohn. 1987. Discrete detectors for near-real-time radiography. Materials Evaluation 45:1320–1325.

Haaker, P., E. Klotz, R. Koppe, and R. Linde. 1988. Real-time distortion correction of digital X-ray II/TV systems: an application example. Image Processing II, SPIE 1027:261–266.

Halmshaw, R. 1987. An analysis of the performance of X-ray television-fluoroscopic equipment in weld inspection. Materials Evaluation 45:1298–1302.

Halmshaw, R. 1990. Review of digital radiological methods. British Journal of Nondestructive Testing 32(1):17–26.

Herman, G. T., ed. 1979. Image reconstruction from projections : implementation and applications. Springer-Verlag, New York, NY.

Hillen, W., U. Schiebel, and T. Zaengel. 1987. Imaging performance of a digital storage phosphor system. Medical Physics 14(5):744–751.

Jacquemod, G., C. Odet, and R. Goutte. 1990. X-ray real-time evaluation of a new line detector for inspection of stripped steel. Nondestructive Testing and Evaluation 5:239–248.

Link, R., W. Nuding, H. Wiacker, H. P. Busse, and J. J. Munro, III. 1989. Weld inspection using real-time radiography. International Advances in Nondestructive Testing 14:143–173.

Martz, H. E., S. G. Azevedo, G. P. Robertson, D. J. Schneberk, and M. F. Skeate.

1990. Computerized tomography. UCRL-53868-89. Lawrence Livermore National Laboratory, Livermore, CA.

McNeil, G. T. 1966. X-ray stereo photogrammetry. Photogrammetric Engineering 32(6):993–1004.

Meinel, E. S. 1986. Origins of linear and nonlinear recursive restoration algorithms. Journal of the Opical Society of America, Part A 3(6):787–799.

Mengers, P. 1980. Real-time digital image processing for radiological imaging. Pages 267–276 in D. A. Garrett and D. A. Bracher, eds. Real-time radiologic imaging: medical and industrial applications. American Society for Testing and Materials, Philadelphia, PA.

Munro, J.J., R. E. McNulty, W. Nuding, H. P. Busse, H. Wiacker, R. Link, K. Sauerwein, and R. Grimm. 1987. Weld inspection by real-time radioscopy. Materials Evaluation 45:1303–1325.

Olsen, R. 1988. More than just a pretty picture: Real-time X-ray image enhancement in the electronics industry. Materials Evaluation 46:1403–1408.

Photometrics. 1991. Charge-couple devices for quantitative electronic imaging. Photometrics, Ltd., Tucson, AZ.

Precise Optics. 1990. Data sheet. Comparison of new HP and HX intensifiers with previous F generation. Precise Optics Photo Medic Equipment, Inc., Bay Shore, NY.

Press, W. H., B. P. Flannery, S. A. Teukolsky, and W. T. Vetterling. 1988. Numerical recipes in C: the art of scientific computing. Cambridge University Press, New York, NY.

Quinn, R. A., and C. C. Sigl. 1980. Radiography in modern industry. Eastman Kodak, Rochester, NY.

Reichenbach, S. E., S. K. Park, and R. Narayanswamy. 1991. Characterizing digital image acquisition devices. Optical Engineering 30(2):170–176.

Roberts, R. A. 1991. Limited data tomography using a minimal support constraint. Pages 435–442 in D. O. Thompson and D. E. Chimenti, eds. Review of Progress in Quantitative NDE Vol. 10A, Plenum Press, New York.

Samuelson, E. G., and B. Jaggi. 1989. Design and implementation of a solid state imaging system for visible light and X-ray imaging. Pages 393–394 in Proceedings of the 11th Annual International Conference of the IEEE Engineering in Medicine and Biology Society, Part 2. Alliance for Engineering in Medicine and Biology, Washington, DC.

Segal, Y., and B. Cohen. 1990. Computerized laminagraphy. NDT International 23(3):137–146.

Seibert, J. A., O. Nalcioglu, and W. W. Roeck. 1984. Characterization of the veiling glare PSF in X-ray image intensified fluoroscopy. Medical Physics 11(2):172–179.

Stupin, D. M. 1987. Filmless radiographic detection of microscopic wires and very small areal density variations. Materials Evaluation 45:1315–1319.

Tekalp, A. M., H. Kaufman, and J. W. Woods. 1986. Identification of image an blur parameters for the restoration of noncausal blurs. IEEE Transactions on Acoustics, Speech, and Signal Processing ASSP-34(4):963–972.

Terry, C. 1990. C compilers for real-time software. EDN 35(7):96–100.

Veress, S. A., F. G. Lippert, and T. Takamoto. 1977. An analytical approach to X-ray photogrammetry. Photogrammetric Engineering and Remote Sensing 43(12):1503–1510.

Veress, S. A. 1989. X-ray photogrammetry, systems, and applications. Pages 167–186 in H. M. Karara, ed. Non-Topographic Photogrammetry. 2nd ed. American Society for Photogrammetry and Remote Sensing, Falls Church, VA.

Wallingford, R. M., and J. P. Basart. 1988. 3-D crack reconstruction in radiographic images using projections obtained from a linear sample shift. Pages 68–72 in R. R. Chen, ed. Conference Record for the Twenty-second Asilomar Conference on Signals, Systems, and Computers. Maple Press, San Jose, CA.

Wallingford, R. M. 1990. Flaw reconstruction in NDE using a limited number of X-ray radiographic projections. PhD dissertation. Iowa State University, Ames, IA.

Weinhaus, F., and M. Walterman. 1990. A flexible approach to image warping. Image Processing Algorithms and Techniques, SPIE 1244:108–122.

Williams, C. S. 1989. Introduction to the optical transfer function. Wiley, New York.

Wilson, D. 1992. Is RISC or DSP best for your application? Computer Design 31(4):65–72.

Zheng, Y., and J. P. Basart. 1988. Deblurring NDE X-ray images and infrared images by a maximum entropy deconvolution method. Pages 72–76 in R. R. Chen, ed. Conference Proceedings of the Twenty-first Asilomar Conference on Signals, Systems and Computers. Maple Press, San Jose, CA.

Zhu, Y. M., D. Babot, and G. Peix. 1990. A quantitative comparison between linear X-ray sensitive array and image-intensifier systems. NDT International 23(4):214–220.